Transport through a resonator-coupled double quantum dot

Zenelaj, Drilon

2025

Transport through a resonator-coupled double quantum dot

DRILON ZENELAJ
DEPARTMENT OF PHYSICS | FACULTY OF SCIENCE | LUND UNIVERSITY

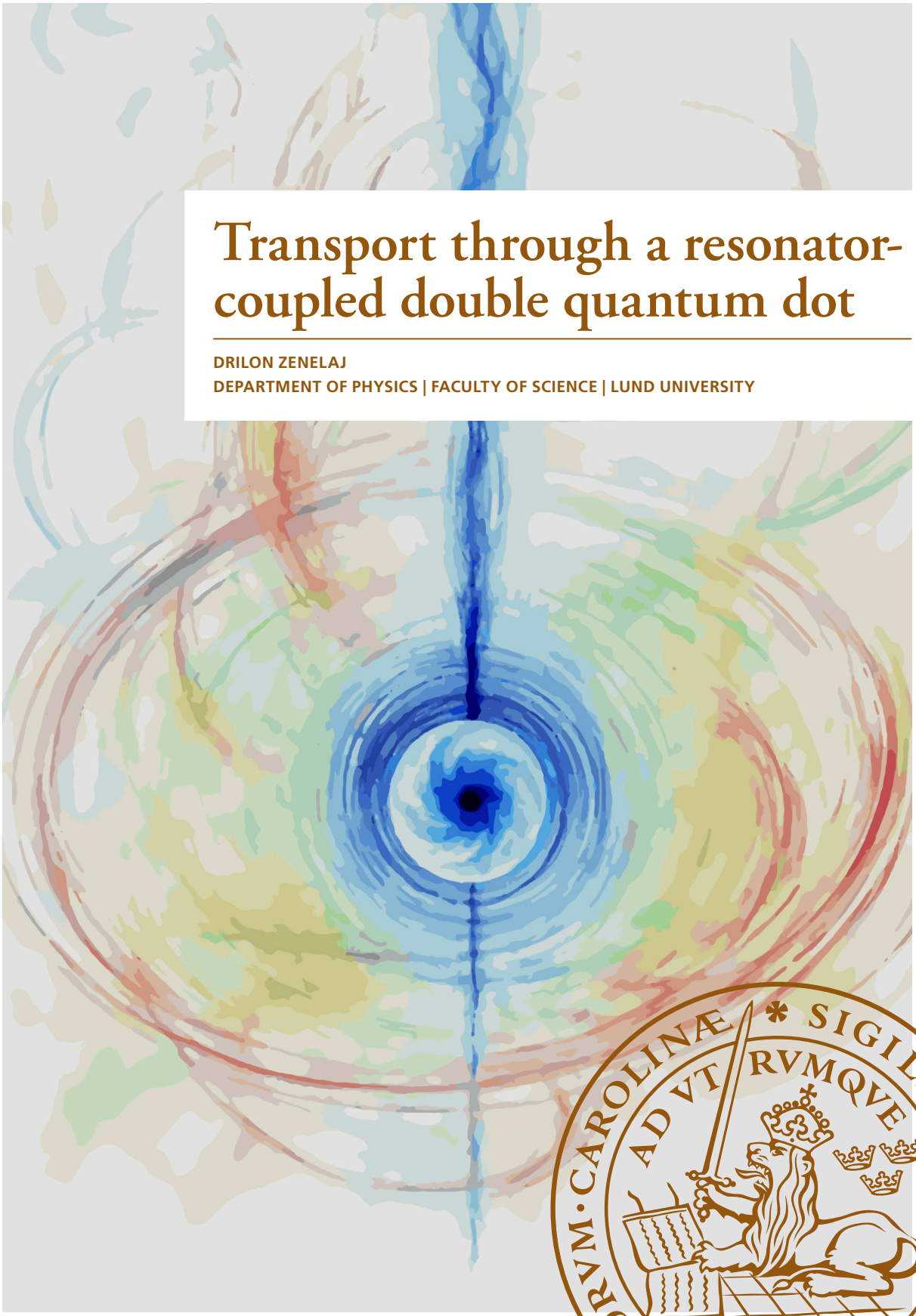

Printed by Media-Tryck, Lund 2025 NORDIC SWAN ECOLABEL 3041 0903

Faculty of Science
Department of Physics

ISBN 978-91-8104-296-2

Transport through a resonator-coupled double quantum dot

Transport through a resonator-coupled double quantum dot

by Drilon Zenelaj

LUND
UNIVERSITY

Thesis for the degree of Doctor of Philosophy
Thesis advisors: Prof. Peter Samuelsson, Prof. Patrick P. Potts
Faculty opponent: Prof. Guido Burkard

To be presented, with the permission of the Faculty of Science of Lund University, for public criticism in the Lundmark lecture hall (Lundmarksalen) at the Division of Astrophysics, Department of Physics on Friday, the 4th of April 2025 at 09:15.

Organization	Document name
LUND UNIVERSITY Department of Physics Box 118 SE–221 00 LUND Sweden	**DOCTORAL DISSERTATION** Date of disputation 2025-04-04 Sponsoring organization
Author(s) Drilon Zenelaj	

Title and subtitle

Transport through a resonator-coupled double quantum dot

Abstract

Nanoscale systems coupled to superconducting circuits offer a platform to study a variety of research questions ranging from more fundamental investigations on the quantum nature of light interacting with matter to more application-oriented ones such as quantum computing and communication. These hybrid systems have thus gained a great deal of attention in the community in the recent years and have led to a whole new research field called circuit quantum electrodynamics (cQED).

In this thesis, the cQED system of interest is a semiconductor double quantum dot (DQD) coupled to a superconducting microwave resonator (MR). The main focus lies on the study of photo-assisted electron transport and the potential applicability of the DQD-MR hybrid system as a detector for single microwave photons.

In Paper I, we study the zero-frequency full counting statistics (FCS) and the finite-frequency noise (FFN) of the photo-assisted electric current through the DQD-MR system in the case when the system is driven by a monochromatic, coherent source of microwave radiation. We find analytical solutions to the FCS and the FFN in the limits of low and large drive strengths.

In Paper II, we study the photo-assisted electron transport in the case when the system is driven by a single, coherent microwave pulse. In the limit of low drive, we develop a Wigner-function formalism for the drive and the detector, giving a visually compelling tool to study the interaction between the drive and the system. We use this formalism to compute the photo-assisted current and analyze the performance of the detector in different parameter regimes.

In Paper III, we demonstrate the conversion of microwave to electrical power in the DQD-MR system by running the photo-assisted current against an applied bias between the source and drain of the DQD. The device reaches a maximum power-harvesting efficiency of 2% for an incoming microwave power of 2 fW.

In Paper IV, we investigate the role of charge transport on the coherence of light-matter coupling in a DQD strongly coupled to a high-impedance microwave resonator by applying a finite voltage bias across the DQD. An inherent asymmetry in the tunnel couplings to the electronic leads shows how different charge occupations effect the decoherence in this system. We also find an electron-hole symmetry between different bias polarities.

Key words

quantum transport, open quantum systems, double quantum dots, microwave resonators, circuit QED, full counting statistics, single photon detectors

Classification system and/or index terms (if any)

Supplementary bibliographical information		Language English
ISSN and key title		ISBN 978-91-8104-296-2 (print) 978-91-8104-297-9 (pdf)
Recipient's notes	Number of pages 177	Price
	Security classification	

Transport through a resonator-coupled double quantum dot

by Drilon Zenelaj

LUND
UNIVERSITY

A doctoral thesis at a university in Sweden takes either the form of a single, cohesive research study (monograph) or a summary of research papers (compilation thesis), which the doctoral student has written alone or together with one or several other author(s).

In the latter case the thesis consists of two parts. An introductory text puts the research work into context and summarizes the main points of the papers. Then, the research publications themselves are reproduced, together with a description of the individual contributions of the authors. The research papers may either have been already published or are manuscripts at various stages (in press, submitted, or in draft).

Cover illustration front: Artistic interpretation of the thesis work by my dear friend VASR.

Funding information: The thesis work was financially supported by the Knut and Alice Wallenberg Foundation through the Wallenberg Center for Quantum Technology (WACQT).

Faculty of Science, Department of Physics

ISBN: 978-91-8104-296-2 (print)
ISBN: 978-91-8104-297-9 (pdf)

Printed in Sweden by Media-Tryck, Lund University, Lund 2025

Media-Tryck is a Nordic Swan Ecolabel certified provider of printed material. Read more about our environmental work at www.mediatryck.lu.se

MADE IN SWEDEN

Dedicated to my parents
Përkushtuar prindërve të mi

Contents

List of publications

This thesis is based on the following publications, referred to by their Roman numerals:

I **Full counting statistics of the photocurrent through a double quantum dot embedded in a driven microwave resonator**
Drilon Zenelaj, Patrick P. Potts, and Peter Samuelsson
Phys. Rev. B 106, 205135 (2022)

II **Wigner-function formalism for the detection of single microwave pulses in a resonator-coupled double quantum dot**
Drilon Zenelaj, Peter Samuelsson, and Patrick P. Potts
(submitted to Phys. Rev. Res.)

III **Microwave power harvesting using resonator-coupled double quantum dot photodiode**
Subhomoy Haldar, **Drilon Zenelaj**, Patrick P. Potts, Harald Havir, Sebastian Lehmann, Kimberly A. Dick, Peter Samuelsson, and Ville F. Maisi
Phys. Rev. B 109, L081403 (2024)

IV **Symmetries and decoherence in a double quantum dot coupled to a high-impedance microwave resonator**
Drilon Zenelaj, Antti Ranni, Patrick P. Potts, Sebastian Lehmann, Kimberly A. Dick, Peter Samuelsson, and Ville F. Maisi
(manuscript in preparation)

Publications not included in this thesis:

High-efficiency microwave photodetection by cavity coupled double dots with single cavity-photon sensitivity
Subhomoy Haldar, Harald Havir, Waqar Khan, **Drilon Zenelaj**, Patrick P. Potts, Sebastian Lehmann, Kimberly A. Dick, Ville F. Maisi, and Peter Samuelsson
(submitted to Phys. Rev. Applied)

Acknowledgments

I would like to start by expressing my deepest gratitude to my main supervisor, Peter. Thank you for offering me the opportunity to do my PhD in your group and for your continuous guidance and help during those years. Your open and cheerful nature created a very welcoming atmosphere within the group and took away a lot of the stress that typically comes with the PhD. I've always felt like I can come to you with any odd question, no matter how big or small. I have also very much appreciated the encouragement and freedom you gave me and all the other group members, which really helped with keeping up the motivation in times where it was hard to do so. I've learned a lot from you and I wish you all the best.

I would also like to thank my second supervisor, Patrick. Your input and support has been very valuable and necessary to keep things going. I have also always appreciated your creativity in coming up with new ideas and methods to solve a specific problem we were having. Mostly, I appreciate that you continued with the supervision even after you moved to Basel to start your own group. I have also always felt very welcome when I visited you in Basel and have enjoyed every stay. I've also learned a lot from you and wish you the best as well.

I'm also grateful to all the members of the group whom I had the pleasure of meeting and working together with: Björn, Morten, Pharnam, Saulo, Kalle and Daniel. The atmosphere within the group has always been very open, friendly and supportive. Our discussions in the group meetings were always very interesting and I appreciated the humor all of you brought in.
Thanks also to all the other members of the MatFys division during those years. The working environment has always been pleasant and I enjoyed the table-tennis sessions and all the activities we did outside of work very much.
A special thanks goes to Katarina. You were always very helpful with everything not related to science that comes with working at a university and I knew that I could reach out to you whenever I needed help and that your door was always open.

Thanks also to Ville for giving me the opportunity the collaborate with his group and get a deep insight into how the experiments work that are related to my research. I have learned a lot from these collaborations and have felt a lot of support also from you and your group members.

My gratefulness also extends to all the friends I have made outside of work and the great times we have spent together. Thanks to the wonderful room mates I met at the guest house: Silvia, Gareth and Mike. Thank you Mike for staying with me as a great room mate and friend. Thanks to my (E)Spanish crew: Juan-Carlos, Claudia and Albert. All the WACQT trips would have been much less enjoyable without you.

Finally, I would like to show my deepest regards for my friends and family back home in Switzerland: My mother and father, my brother Dardan and his wife Afrorë together with their beautiful kids Kian and Joen, my friends Stefan, Cagla, Valentina, Vladislav, Gionatan, Mario, Eliane, Valentino, Jil, Noa, Melanie and Andreea. You have helped me and supported me and are continuing to do so in all ways imaginable. I don't know where I would be without you and will never be able to thank you enough for your love and guidance.

Mostly, I thank my parents for their love and support. You have always been there for me and have provided for me such that I can live the life I want and continue to follow my dreams. I am very grateful for that, and hope that I will have you by my side for many more years to come. *Ju dua shumë*.

Popular science summary

Quantum mechanics, the branch of physics governing the smallest scales of nature, reveals a world where particles can exist in multiple states simultaneously and interact in ways that defy classical intuition. These principles are the foundation of cutting-edge technologies such as quantum computing and quantum communication. This doctoral research delves into this fascinating domain, investigating a hybrid system of double quantum dots coupled to superconducting microwave resonators — an innovative platform for exploring quantum phenomena and advancing practical applications.

A quantum dot (QD) is a nanoscale structure that confines electrons in all three spatial dimensions, effectively creating an "artificial atom." The confinement leads to discrete energy levels, much like those in real atoms, and enables the precise manipulation of electrons using external fields. When two such quantum dots are coupled, they form a double quantum dot (DQD), or an "artificial molecule," where electrons can tunnel between the dots. This tunneling behavior, a quintessential quantum phenomenon, depends on the relative energy levels of the two dots and the strength of their coupling.

DQDs are remarkable because they allow researchers to create and study a tunable two-level system, a key element in quantum information processing. By adjusting external parameters like electric or magnetic fields, the energy difference between the two dots can be precisely controlled. This tunability makes DQDs ideal for applications in quantum computing, where they can function as qubits, and in quantum sensing, where their sensitivity to electromagnetic fields can be leveraged.

To further probe and utilize the quantum properties of DQDs, they are coupled to superconducting microwave resonators (MRs). These resonators, made of superconducting materials, can confine electromagnetic waves in the microwave frequency range. This confinement creates standing waves, analogous to sound vibrations in a musical instrument, but at much smaller scales and higher frequencies. MRs are central to circuit quantum electrodynamics (cQED), a field that studies the interaction between light (photons) and matter (like QDs or superconducting qubits).

MRs are particularly advantageous because they operate in the quantum regime, where photons can be individually counted and manipulated. They also integrate seamlessly into electronic circuits, making them suitable for scalable quantum technologies. The coupling of a DQD to a MR enables the controlled exchange of energy between the electrons in the DQD and the photons in the resonator, opening new avenues for investigating quantum interactions.

The research presented in this thesis explores the rich interplay between electrons in DQDs and photons in MRs, shedding light on how this hybrid system can be harnessed for novel

applications.

The coupling of DQDs with MRs exemplifies the power of hybrid quantum systems in bridging the gap between fundamental physics and practical applications. By investigating photo-assisted transport and energy-conversion mechanisms, this research contributes to our understanding of quantum transport, light-matter interaction, and open quantum systems. These findings have implications for quantum computing, where precise control of qubits is essential, and for quantum communication, where detecting and manipulating individual photons is critical.

Moreover, the work on microwave power harvesting highlights the potential for sustainable and efficient energy technologies based on quantum principles. As the quantum revolution continues to unfold, hybrid systems like the DQD-MR platform stand at the forefront of innovation, combining theoretical expertise with technological advancement.

In essence, this research demonstrates how the strange and beautiful rules of the quantum world can be harnessed to build the technologies of tomorrow, paving the way for a future where quantum mechanics transforms communication, computation, and energy.

Chapter 1

Introduction

The ability to fabricate systems at a scale of several hundreds to tens of nanometers has in recent decades lead to a greater understanding of how the constituents of matter behave when confined to a size comparable to or even smaller than their de Broglie wavelength. Under this strong spatial confinement, the physics of the systems cannot accurately be described by classical means, and one has to rely on quantum mechanics. Quantum effects such as the quantization of energy levels and quantum tunneling are used in many areas of research from both an application-oriented point of view but also to gain a greater understanding on the fundamentals of quantum physics.
A field that relies on such effects is quantum transport [1]. This field is concerned with the study of transport of single or multiple particles across nanostructures. One of the most well-studied transport scenarios is electrons moving through semiconductor quantum dots (QDs) [2]. By controlling the quantized energy levels within the QD, the flow of electrons can either be enhanced or prohibited, creating what is known as a single electron transistor (SET) [3]. Coupling several QDs in series allows for an even greater control of the electronic transport, including the ability to manipulate the directivity of the flow or to select the spin of the transported electron[4].
Through said control of the energy levels, an electron can also be trapped within a QD and manipulated through the application of electromagnetic fields [5]. The QD offers thus a great platform for several qubit architectures, such as charge [6] or spin qubits [7], and also to study the interaction between electrons and the applied fields [8]. This type of interaction lies at the heart of quantum electrodynamics (QED) [9].
QED describes the interaction between light and matter at the quantum level. This typically involves scenarios where electrically charged particles interact via the exchange of a photon. QED was the first theory that saw an agreement between quantum mechanics and special relativity. It was able to very accurately predict many physical phenomena, such as the Lamb shift in hydrogen. The exchange of photons with the charged particle

typically involves transitions of the particle between different energy levels. In order to address and manipulate specific transitions, one has to hit the particle with a photon of a frequency close to the energy splitting of the levels. An efficient method for generating and confining photons at a specific frequency is to utilize an optical cavity composed of two highly reflective mirrors. The cavity is a type of resonator whose resonant frequency can be tuned by changing the distance between the mirrors. The study of light-matter interactions in optical cavities is called cavity QED [10]. In cavity QED systems, coherent interactions between photons and electronic systems allow for widely used applications like single-photon sources [11] or quantum sensors [12].
The circuit analogue of cavity QED, called circuit QED (cQED) [13], uses resonators made out of superconducting circuits, which trap photons in the microwave regime. The advantage of this is that the cQED system can be directly integrated into a circuit. Some of the state-of-the-art qubit architectures rely on these circuits, like IBM's quantum computer [14]. Important features for quantum technology applications such as strong light-matter coupling [15] and long coherence times [16] have been achieved in cQED experiments, both for superconducting qubits [17] as well as QDs [18, 19] that are coupled to the photons in the resonator.
It has also been theoretically predicted that a double quantum dot (DQD) coupled to a microwave resonator (MR) could act as a platform for efficient and continuous detection of single microwave photons [20]. The detection of microwave photons is an important but elusive task. It is important because it finds applications in many areas ranging from quantum information [21, 22] to astronomy [23], but it is elusive because of the low energy of microwave photons. In the optical regime, single photon detectors typically rely on the excitation of an electron across the bandgap of a semiconductor [24]. In the microwave regime this approach does not work because there are no semiconductors with such small bandgaps. A different approach is thus needed, and this is where the DQD-MR system comes in. Within a DQD, the energy splitting of the two energy levels can be tuned such that it matches the frequency of the photons in the MR. The detection scheme relies on the photon-assisted transport of an electron across the DQD. Experiments so far have shown that this approach is indeed promising. High photon-detection efficiencies [25] and single-photon sensitivities have been reported [26].

In this thesis, we investigate several questions regarding the photo-assisted transport of electrons through a DQD that is coupled to a MR. The thesis is a compilation of four research papers, all of them dealing with a different aspect of said transport scenario. Paper I deals with the full counting statistics (FCS) of the photo-assisted current, or photocurrent, through the DQD when the system is driven by a monochromatic, coherent drive. Paper II investigates a drive that consists of a single microwave pulse and presents a Wigner-function formalism for the detection of the pulse. Paper III presents a realization of a microwave-power to electrical-power converter, which is achieved by applying a finite bias across the DQD. Paper IV studies the role of charge transport on the coherence of light-matter coup-

ling.
The main text in the first part of the thesis contains several chapters which give an introduction to DQDs, MRs, cQED systems, quantum transport and dynamics, FCS, Wigner functions and power harvesting. Within those chapters we also summarize the main findings of the research papers. In the second part the four research papers are attached. We also give an introduction to input-output theory in the appendix.

Chapter 2

Double Quantum Dots

A quantum dot (QD), sometimes referred to as "artificial atom", is a man-made nanostructure that exhibits unique electronic and optical properties due to its small size. QDs are typically created out of semiconducting materials, and one distinguishes mainly between three different types: colloidal [27], self-assembled [28] and electrostatic (or gated) QDs [29]. The strong spatial confinement in all three dimensions leads to the quantization of energy levels in the QD. This confinement is typically highly tunable in the lab, which leads to a strong control over the aforementioned properties of the QD.
QDs have thus found applications in a variety of research areas. A QD can be used as a qubit inside a quantum computer [6, 7, 30], or as an LED inside your television [31]. QDs even find applications in medical imaging and diagnostics [32, 33].
A natural continuation to the field of QD research is to couple two QDs, which then forms a double quantum dot (DQD), also labeled "artificial molecule". The two QDs comprising the DQD are usually spaced close to each other, such that quantum tunneling of electrons between the two QDs can occur. This tunnel coupling lends the DQD several additional and interesting properties [34]. In a strong-coupling regime, the particle picture for an electron in the DQD does not suffice to accurately describe its physical behavior. Rather, the electron exhibits properties of a coherent wave, which is delocalized over the two QDs. Coherence in the DQD is a purely quantum-mechanical phenomenon, which can function as a resource for several quantum technology applications [35, 36]. This is because it enables the maintenance of superposition and entanglement, a key prerequisite for quantum error correction and communication protocols [37].
A different important property of the DQD is the ability to control two separate discrete energy levels within the same system, creating a so-called two-level system (TLS) with a tunable energy gap. This TLS can serve as a qubit architecture [38, 39], the creation of single photonic states [40, 41] or, as we will discuss in detail later, the detection of single photons [20].

We see that the DQD offers a platform to investigate many interesting directions of research, and it is for this reason that the DQD is one of the main building blocks for the scientific results presented in this thesis.

In this chapter, we present a theoretical description of the DQD. In Sec. 2.1, we derive a Hamiltonian description for a single QD and introduce the notion of second quantization. In Sec. 2.2, we derive the Hamiltonian for a DQD.

Note that, for the results presented below, we set $\hbar = 1$ throughout.

2.1 QD Hamiltonian

As mentioned above, the QD is also called an artificial atom. And similarly to an atom, where the electrons are confined by the attractive potential of the nucleus, the electrons in the QD are typically bound by a quantum-well type potential, usually created through a combination of semiconducting materials with different bandgaps, see Fig. 2.1, or the use of electrostatic gates. It should be noted that seminconductor QDs usually consist of a large

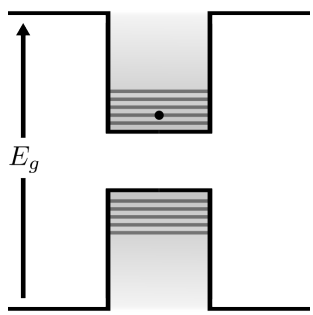

Figure 2.1: Energy level diagram of a QD made out of a semiconductor heterostructure, which is produced by layering two materials with different band gaps E_g. The bandgap offset creates a strong confinement in the center semiconductor, which leads to a discretization of energy levels within the valence and conduction bands of the material. We will in this thesis only be interested in studying electrons, and thus we will focus solely on the conduction band.

$(10^3 - 10^9)$ number of atoms. Most of the atoms' electrons are bound to the nuclei, such that there are only a small $(0 - 10^3)$ number of free electrons. The Schrödinger equation for these free electrons is given by

$$\hat{H}\psi = E\psi, \tag{2.1}$$

where $\psi = \psi(\mathbf{r}_1, ..., \mathbf{r}_{N_e})$ is the wave function of N_e electrons at positions $\mathbf{r}_i$, $\hat{H}$ is the total Hamilton operator or Hamiltonian and E is the total energy eigenvalue.

The total Hamiltonian is given by

$$\hat{H} = \sum_{i=1}^{N_e} \hat{H}_0(\mathbf{r}_i) + \frac{1}{2} \sum_{i \neq j} \frac{e^2}{|\mathbf{r}_i - \mathbf{r}_j|}, \tag{2.2}$$

where e denotes the electron charge. The total Hamiltonian is thus a sum of the single-particle Hamiltonian $\hat{H}_0(\mathbf{r}_i)$ and a Coulomb interaction term. The single-particle Hamiltonian is given by

$$\hat{H}_0(\mathbf{r}_i) = \frac{\hat{\mathbf{p}}_i^2}{2m^*} + V(\mathbf{r}_i), \tag{2.3}$$

where m^* denotes the effective electron mass, $\hat{\mathbf{p}}_i$ gives the canonical momentum operator and $V(\mathbf{r}_i)$ is the single-particle confinement potential, which can typically be well described by an infinite square well potential

$$V(\mathbf{r}_i) = \begin{cases} 0, & -L/2 < |\mathbf{r}_i| < L/2 \\ \infty, & \text{else} \end{cases}, \tag{2.4}$$

where L denotes the total length of the well.
We will from now on only be interested in the simplified case where only a single free electron resides on the QD. The reason for that will become clear later. In this case, the total Hamiltonian is given by

$$\hat{H} = \frac{\hat{\mathbf{p}}^2}{2m^*}. \tag{2.5}$$

2.1.1 Second quantization

A focal theme in this thesis is the transport of electrons through a DQD. Such transport scenarios are best described using the formalism of second quantization, also known as occupation number representation [42]. As the name suggests, the formalism offers a convenient way to describe the occupation of a given quantum state and introduces the notion of creation and annihilation operators to move between states which are occupied by different number of particles.
For fermions, the creation operator $\hat{c}^\dagger$ and annihilation operator $\hat{c}$ obey the following anti-commutation relations

$$\{\hat{c}, \hat{c}^\dagger\} = 1, \qquad \{\hat{c}, \hat{c}\} = \{\hat{c}^\dagger, \hat{c}^\dagger\} = 0. \tag{2.6}$$

Due to the latter relation, we find that $(\hat{c}^\dagger)^2 = (\hat{c})^2 = 0$, implying that only a single fermion can occupy a given state, which is the famous Pauli exclusion principle. We further have the following relations

$$\hat{c}\,|0\rangle = 0, \qquad \hat{c}^\dagger\,|1\rangle = 0, \qquad \hat{c}^\dagger\hat{c}\,|n\rangle = \hat{n}\,|n\rangle = n\,|n\rangle\,, \tag{2.7}$$

where $n = 0, 1$. The operator $\hat{n}$ is called number operator and it gives the occupation of a given state $|n\rangle$.
We can now describe the basis state in Eq. (2.1) $|\psi\rangle$ in second quantized form

$$\Psi^\dagger(\mathbf{r}) \equiv \langle \mathbf{r}|\psi\rangle^* \, \hat{c}^\dagger = \psi^*(\mathbf{r})\hat{c}^\dagger, \qquad \Psi(\mathbf{r}) \equiv \langle \mathbf{r}|\psi\rangle \, \hat{c} = \psi(\mathbf{r})\hat{c}. \tag{2.8}$$

From Eq. (2.6) we can deduce that

$$\{\Psi(\mathbf{r}_1), \Psi^\dagger(\mathbf{r}_2)\} = \delta(\mathbf{r}_1 - \mathbf{r}_2). \tag{2.9}$$

The single-particle Hamiltonian in second quantization is then given by

$$\hat{H}_{\mathrm{QD}} = \int d\mathbf{r}\, \Psi^\dagger(\mathbf{r})\hat{H}(\mathbf{r})\Psi(\mathbf{r}) = \epsilon_0 \hat{n}, \tag{2.10}$$

where

$$\epsilon_0 = \int d\mathbf{r}\, \psi^*(\mathbf{r})\hat{H}(\mathbf{r})\psi(\mathbf{r}), \tag{2.11}$$

denotes the single-particle energy.

2.2 DQD Hamiltonian

We now have all the tools we need to present the Hamiltonian of a DQD in second quantized form. The single-particle Hamiltonians for the separate QDs will be equivalent to the one in Eq. (2.10). To distinguish both QDs, we are going to attach a subscript L (R) to the quantities describing the left (right) QD

$$\hat{H}_{\mathrm{L}} = \epsilon_{\mathrm{L}} \hat{n}_{\mathrm{L}}, \qquad \hat{H}_{\mathrm{R}} = \epsilon_{\mathrm{R}} \hat{n}_{\mathrm{R}}. \tag{2.12}$$

Writing the creation operator for the left (right) QD as $\hat{c}^\dagger_{\mathrm{L(R)}} = |L\rangle\langle 0|$ ($|R\rangle\langle 0|$), where $|L\rangle$ ($|R\rangle$) denotes the state of the left (right) QD, we get

$$\hat{H}_{\mathrm{L}} = \epsilon_{\mathrm{L}} \, |L\rangle\langle L| \, , \qquad \hat{H}_{\mathrm{R}} = \epsilon_{\mathrm{R}} \, |R\rangle\langle R| \, . \tag{2.13}$$

Setting $\epsilon_{\mathrm{L}} = -\epsilon_{\mathrm{R}}$ and defining $\epsilon = \epsilon_{\mathrm{L}} - \epsilon_{\mathrm{R}}$, we write the the sum of the two terms in Eq. (2.13) as

$$\hat{H}_{\mathrm{L}} + \hat{H}_{\mathrm{R}} = \frac{\epsilon}{2}(|L\rangle\langle L| - |R\rangle\langle R|). \tag{2.14}$$

As mentioned above, an electron inside a DQD can tunnel coherently between the two QDs. This process also needs to be accounted for in the total Hamiltonian of the DQD. We denote with t_c the real tunneling amplitude between $|L\rangle \leftrightarrow |R\rangle$ and introduce the tunneling Hamiltonian as

$$\hat{H}_{\mathrm{T}} = t_c(|L\rangle\langle R| + |R\rangle\langle L|). \tag{2.15}$$

The total DQD Hamiltonian is then given by $\hat{H}_{\mathrm{DQD}} = \hat{H}_{\mathrm{L}} + \hat{H}_{\mathrm{R}} + \hat{H}_{\mathrm{T}}$.
It is more convenient for further analysis to work in the eigenstate basis of the DQD, which is found by diagonalizing $\hat{H}_{\mathrm{DQD}}$. The eigenstate basis is spanned by the ground state $|g\rangle$ and excited state $|e\rangle$, which are defined by

$$\begin{pmatrix} |g\rangle \\ |e\rangle \end{pmatrix} = \begin{pmatrix} \cos\theta/2 & -\sin\theta/2 \\ \sin\theta/2 & \cos\theta/2 \end{pmatrix} \begin{pmatrix} |L\rangle \\ |R\rangle \end{pmatrix}, \tag{2.16}$$

where $\cos\theta = -\epsilon/\Omega$, with $\Omega = \sqrt{4t_c^2 + \epsilon^2}$ being the DQD energy level splitting. We now write the Hamiltonian of the DQD in this basis as

$$\hat{H}_{\mathrm{DQD}} = \frac{\Omega}{2}\hat{\sigma}_z, \tag{2.17}$$

where $\hat{\sigma}_z = |e\rangle\langle e| - |g\rangle\langle g|$.
From Eq. (2.16) it is clear that the ground and excited states are coherent superpositions of the left and right charge states of the DQD. For a finite tunnel coupling, the two QDs thus hybridize and the wave function of the left (right) QD has a finite spread over the right (left) QD, see Fig. 2.2.

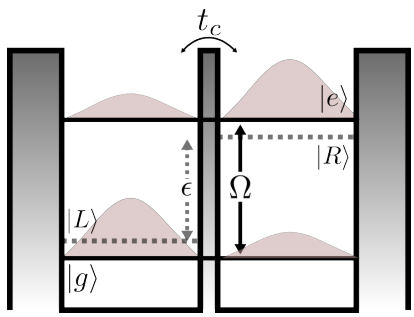

Figure 2.2: Energy level diagram of a DQD. Due to the finite tunnel coupling t_c between the QDs, the state of the left QD $|L\rangle$ and that of the right QD $|R\rangle$ hybridize to form the DQD ground $|g\rangle$ and excited state $|e\rangle$. The wave functions of the QDs thus leak into the neighbouring QD. The level splitting between $|L\rangle$ and $|R\rangle$ is given by ϵ and the splitting between $|g\rangle$ and $|e\rangle$ is given by Ω.

Chapter 3

Microwave Resonators

The term resonator typically describes a system that oscillates more strongly at certain frequencies compared to others. These frequencies are called resonant frequencies. A special type of resonator is the cavity resonator [43], which is able to confine waves which oscillate at the resonant frequencies of the cavity. A microwave resonator cavity, or short microwave resonator (MR) [44], is therefore a system that traps standing electromagnetic waves at frequencies in the microwave regime. There exist different kinds of MRs, but the one relevant for this thesis is the superconducting transmission line resonator (STLR) [45]. This type of resonators are typically produced by choosing a transmission line, such as a coaxial cable, which is then short-circuited at two ends, such that an electromagnetic standing wave may be trapped between both ends, see Fig. 3.1. The frequency of the wave is then dependent on the geometry of the system. The reason for choosing superconducting materials will become clear in the following section.
STLRs are widely used in various areas of research, ranging from more fundamental studies of light interacting with matter at the quantum level [46, 47], to more application-oriented investigations on how one can use the light inside the STLR to manipulate and couple qubits [48]. One of the main advantages of STLRs are their high quality factor [49] which, together with the fact that they are operated at ultra-low temperatures, leads to large coherence times of the trapped light. They can also be integrated into existing circuit architectures, something we will explore in depth in the following chapter.
We can see that STLRs offer a plethora of interesting avenues of research, which is why they are the second main building block of this thesis.

In this chapter, we present a theoretical description of the STLR. In Sec. 3.1, we introduce a theoretical model for the LC-circuit and explain why the STLR is equivalent to a series of LC-circuits. In Sec. 3.2, we quantize the LC-circuit and show that this quantized version is similar to a very well-known system in quantum mechanics. To that end, we also intro-

duce the second quantization formalism for bosons. In Sec. 3.3, we derive the quantum Hamiltonian for the STLR.

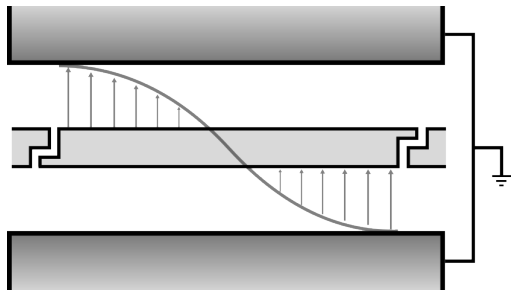

Figure 3.1: Schematic of a transmission line resonator. The resonator sketched is a $\lambda/2$ type resonator, meaning that it traps half the wavelength of an electromagnetic wave, which is also depicted. The top and bottom parts are called ground planes, and the middle part is called center conductor.

3.1 The LC-circuit

A transmission line can be described as a series of distributed inductance (L), capacitance (C) and resistance (R) elements [50]. Shortening the ends of the series of RLC elements restricts the propagation of electromagnetic waves and thus gives a transmission line resonator. If we want to have a lossless transmission line resonator, we need to somehow get rid of the resistance elements. And this is where the superconductor is needed. The electrical resistance of a superconductor drops to zero below its critical temperature. Thus, the STLR can be modeled as a shortened series of LC-circuits, see Fig. 3.2 for the circuit diagram. Our

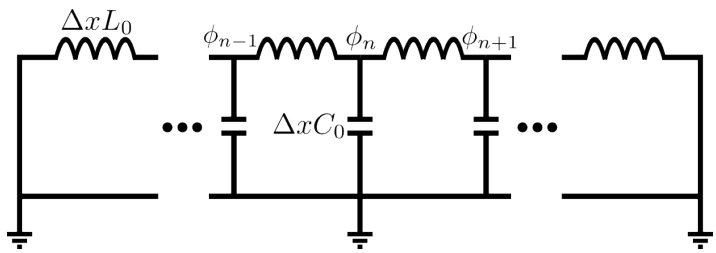

Figure 3.2: Circuit diagram for the STLR, consisting of a shortened series of LC-circuits, which is composed of parallel grounded capacitors with a capacitance of C_0 per unit length Δx, and a series of inductors with an inductance of L_0 per unit length Δx. The symbol ϕ_n denotes the flux threading the inductor at node n and is defined in the main text.

goal later will be to quantize the series of LC-circuits [51]. To that end, we start classically and introduce the Lagrangian $\mathcal{L}$ for a single LC-circuit

$$\mathcal{L}(\phi, \dot{\phi}) = \frac{1}{2} C \dot{\phi}^2 - \frac{1}{2L} \phi^2, \tag{3.1}$$

where ϕ describes the generalized coordinate of the system, C is the capacitance and L is the inductance. The generalized coordinate for an electrical circuit is given by the flux threading the inductor

$$\phi = \int_{-\infty}^{t} dt\, V(t), \tag{3.2}$$

where $V(t)$ is the voltage. We now proceed by deriving the classical Hamiltonian of the circuit, which is a function of the flux and its conjugate momentum

$$q = \frac{\partial \mathcal{L}}{\partial \dot{\phi}} = C\dot{\phi}, \tag{3.3}$$

which generally corresponds to the charge on the capacitor

$$q = \int_{-\infty}^{t} dt\, I(t), \tag{3.4}$$

where $I(t)$ gives the current.
The Hamiltonian is then found through a Legendre transformation of the Lagrangian and gives

$$\mathcal{H}(\phi, q) = \frac{q^2}{2C} + \frac{\phi^2}{2L}. \tag{3.5}$$

It will be useful for the quantization below to to introduce the resonant frequency of an LC-circuit

$$\frac{\phi^2}{2L} \to \frac{1}{2} C\omega_{\mathrm{r}}^2 \phi^2, \qquad \omega_{\mathrm{r}} = \frac{1}{\sqrt{LC}}. \tag{3.6}$$

3.2 Quantization of an LC-circuit

The quantization of the Hamiltonian in Eq. (3.5) follows the standard procedure. The variables describing the charge and the flux are changed to operators obeying the commutation relation (note again that $\hbar = 1$)

$$[\hat{\phi}, \hat{q}] = i. \tag{3.7}$$

Using this operator notation, the quantum Hamiltonian is given by

$$\hat{H}_{\mathrm{LC}} = \frac{\hat{q}^2}{2C} + \frac{1}{2} C\omega_{\mathrm{r}}^2 \hat{\phi}^2. \tag{3.8}$$

We see that this Hamiltonian resembles that of a quantum harmonic oscillator with frequency ω_{r} and "mass" C. Analogous to the harmonic oscillator, we define ladder operators

to simplify the equations. For bosons, the creation operator $\hat{a}^\dagger$ and annihilation operator $\hat{a}$ obey the following commutation relations

$$[\hat{a}, \hat{a}^\dagger] = 1, \qquad [\hat{a}, \hat{a}] = [\hat{a}^\dagger, \hat{a}^\dagger] = 0. \tag{3.9}$$

We further have the following relations

$$\hat{a}\,|0\rangle = 0, \qquad |n\rangle = \frac{(\hat{a}^\dagger)^n}{\sqrt{n!}}\,|0\rangle\,, \tag{3.10}$$

where $|0\rangle$ denotes the state with no bosons, also called vacuum state, and $|n\rangle$ denotes the state with n bosons and is usually called Fock state. Using these definitions, we find

$$\hat{a}\,|n\rangle = \sqrt{n}\,|n-1\rangle\,, \qquad \hat{a}^\dagger\,|n\rangle = \sqrt{n+1}\,|n+1\rangle\,, \qquad \hat{a}^\dagger\hat{a}\,|n\rangle = n\,|n\rangle\,. \tag{3.11}$$

Applying the ladder-operator notation, we rewrite the charge and flux operators as

$$\hat{\phi} = \sqrt{\frac{Z}{2}}(\hat{a}^\dagger + \hat{a}) \qquad \hat{q} = i\sqrt{\frac{1}{2Z}}(\hat{a}^\dagger - \hat{a}), \tag{3.12}$$

where $Z = \sqrt{L/C}$ is the characteristic impedance of the circuit. Using these relations, we rewrite the Hamiltonian in Eq. (3.8) as

$$\hat{H}_{\mathrm{LC}} = \omega_{\mathrm{r}}\left(\hat{a}^\dagger\hat{a} + \frac{1}{2}\right). \tag{3.13}$$

For the remainder of the thesis, we adhere to the convention of omitting the $1/2$ factor related to zero-point energy.

3.3 STLR Hamiltonian

We model a transmission line by coupling many LC-circuits in series. The Lagrangian for this system is given by

$$\mathcal{L}_{\mathrm{TL}} = \sum_n \left[\frac{1}{2}\Delta x C_0 \dot{\phi}_n^2 - \frac{(\phi_n - \phi_{n-1})^2}{2\Delta x L_0}\right], \tag{3.14}$$

where C_0 (L_0) denotes the capacitance (inductance) per unit length Δx. In the continuum limit $\Delta x \to 0$, the Lagrangian becomes

$$\mathcal{L}_{\mathrm{TL}} = \int dx\, \left[\frac{C_0}{2}\left(\frac{\partial\phi(x,t)}{\partial t}\right)^2 + \frac{1}{2L_0}\left(\frac{\partial\phi(x,t)}{\partial x}\right)^2\right]. \tag{3.15}$$

The classical Hamiltonian for the transmission line is then given by

$$\mathcal{H}_{\mathrm{TL}} = \int dx \left[\frac{1}{2C_0} q^2(x,t) + \frac{1}{2L_0} \left(\frac{\partial \phi(x,t)}{\partial x} \right)^2 \right], \tag{3.16}$$

where $q(x,t)$ is the charge density field and $\phi(x,t)$ is the flux field. Now we quantize the Hamiltonian (3.16). We again start by promoting the charge density and flux fields to operators, which now obey the following commutation relations

$$\begin{aligned} &[\hat{\phi}(x,t), \hat{\phi}(x',t)] = [\hat{q}(x,t), \hat{q}(x',t)] = 0, \\ &[\hat{\phi}(x,t), \hat{q}(x',t)] = i\delta(x-x'). \end{aligned} \tag{3.17}$$

Moving to momentum space, we define by $\hat{a}_k^\dagger$ ($\hat{a}_k$) the operator that creates (annihilates) a boson in the mode with wave vector k. These operators obey the following commutation relations

$$[\hat{a}_k, \hat{a}_{k'}] = [\hat{a}_k^\dagger, \hat{a}_{k'}^\dagger] = 0, \qquad [\hat{a}_k, \hat{a}_{k'}^\dagger] = \delta(k-k'). \tag{3.18}$$

The flux and charge density field operators are then given by, respectively

$$\begin{aligned} \hat{\phi}(x,t) &= \sqrt{\frac{1}{4\pi C_0}} \int dk \, \frac{1}{\sqrt{\omega_k}} [\hat{a}_{-k}^\dagger(t) + \hat{a}_k(t)] e^{ikx}, \\ \hat{q}(x,t) &= \sqrt{\frac{C_0}{4\pi}} \int dk \, i\sqrt{\omega_k} [\hat{a}_{-k}^\dagger(t) - \hat{a}_k(t)] e^{ikx}, \end{aligned} \tag{3.19}$$

where $\omega_k = ck$, with $c = 1/\sqrt{L_0 C_0}$ denoting the velocity of the field in the transmission line. The quantum Hamiltonian of the transmission line can now be written as

$$\hat{H}_{\mathrm{TL}} = \int dk \, \omega_k \left(\hat{a}_k^\dagger \hat{a}_k + \frac{1}{2} [\hat{a}_k, \hat{a}_k^\dagger] \right), \tag{3.20}$$

where the commutator $\frac{1}{2}[\hat{a}_k, \hat{a}_k^\dagger] = \frac{1}{2}\delta(0)$ gives the zero-point energies $\hbar\omega_k/2$ of all the modes.

If we now consider a transmission line resonator [c.f. Fig. 3.2], the length of the system is finite. In this case, the field at the ends of the system is zero and thus, only modes that fulfill $\omega_n = n\pi c/d$ are allowed, where d denotes the length of the system and $n \in \mathbb{Z}$. This restriction on the modes gives the following Hamiltonian for the resonator

$$\hat{H}_{\mathrm{R}} = \sum_n \omega_n \hat{a}^\dagger(\omega_n) \hat{a}(\omega_n). \tag{3.21}$$

Typically, only a single mode is of interest, such that the Hamiltonian simplifies to

$$\hat{H}_{\mathrm{R}} = \omega_{\mathrm{r}} \hat{a}^\dagger \hat{a}. \tag{3.22}$$

Chapter 4

Connecting the Dots (to the Resonator)

The first theory where a full agreement between quantum physics and special relativity was derived is called quantum electrodynamics (QED) [9], which describes interactions between light and matter on the quantum level. One of the simplest such interactions between light and matter is a TLS interacting with a single photon, like an electron surrounding the nucleus of an atom transitioning between two energy levels. The electron in that case can either emit or absorb a photon while it undergoes the transitions.
In the field of cavity QED, the TLS, usually an atom, is placed inside an optical cavity resonator [52], where the TLS and the photonic mode inside the cavity may coherently swap excitations. These coherent interaction lead to a variety of interesting physical phenomena. Starting from an excited TLS, excitations can be swapped between the TLS and the vacuum state of the cavity, leading to so-called vacuum Rabi oscillations [53], which are a purely quantum-mechanical effect. In the same configuration, the hybrid TLS-cavity system can also be used as a source of single photons [11]. One may also entangle the states of the two subsystems [54], which can then act as a platform for quantum computation and quantum communication [55]. Research on cavity QED systems have also led to the advent of the laser [56].
The mesoscopic analogue of cavity QED is called circuit QED (cQED) [13], where resonators made out of superconducting circuits (STLRs) are employed and are coupled to solid-state systems such as QDs [18, 19] or Josephson junctions [57, 58]. In cQED systems, the regime of strong light-matter coupling has been reached [59, 60] and has paved the way for astonishing progress in the field, from research on quantum state transfer between qubits [61] or multiqubit entanglement [62] to more quantum optics related experiments demonstrating single photon generation [63, 64].

We have introduced the two subsystems relevant for the scope of this thesis and have seen that coupling the two opens up a whole new field where one may explore a great diversity of interesting directions of research.

In this chapter, we present a theoretical description of the coupling between the DQD and the MR. In Sec. 4.1, we present a general framework for light-matter interactions in cavity and cQED systems. In Sec. 4.2, we derive the Jaynes-Cummings Hamiltonian, which is one of the most widely used models to describe the kind of light-matter hybrid systems introduced above.

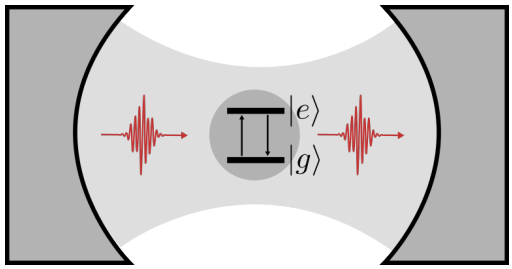

Figure 4.1: Schematic of a cavity QED system. The cavity consist of two highly-reflective, concave mirrors that trap a standing wave of the electromagnetic field. The field interacts with a TLS with ground state $|g\rangle$ and excited state $|e\rangle$. The TLS swaps excitations with the cavity by absorbing and emitting photons.

4.1 Light-matter interactions in cQED systems

Quite generally, the interaction between quantized modes of the electromagnetic field and an electric TLS can be described by the dipole interaction Hamiltonian [65]

$$\hat{H}_{\text{int}} = -\hat{\mathbf{d}} \cdot \hat{\mathbf{E}}(\mathbf{r}), \tag{4.1}$$

where $\hat{\mathbf{d}} = -e\hat{\mathbf{r}}$ gives the dipole moment operator and $\hat{\mathbf{E}}(\mathbf{r})$ gives the electric field operator, where $\mathbf{r}$ denotes the position of the TLS. Working in the subspace spanned by the ground and excited states of the TLS $\{|g\rangle, |e\rangle\}$, we know due to parity that [66]

$$\langle g|\hat{\mathbf{d}}|g\rangle = \langle e|\hat{\mathbf{d}}|e\rangle = 0, \tag{4.2}$$

and thus, we can write the dipole moment operator as

$$\hat{\mathbf{d}} = \mathbf{d}\,|g\rangle\langle e| + \mathbf{d}^*\,|e\rangle\langle g| = \mathbf{d}(\hat{\sigma}_+ + \hat{\sigma}_-), \tag{4.3}$$

where we have assumed that the matrix element $\mathbf{d} = \langle g|\hat{\mathbf{d}}|e\rangle \in \mathbb{R}$ and have introduced the ladder operators $\hat{\sigma}_+ = |e\rangle\langle g|$ and $\hat{\sigma}_- = |g\rangle\langle e|$, which describe the excitation and

de-excitation of the TLS, respectively. The electric field operator is given by [67]

$$\hat{\mathbf{E}}(\mathbf{r}) = \sum_{\mathbf{k}} \boldsymbol{\epsilon}_{\mathbf{k}} \sqrt{\frac{\omega_{\mathbf{k}}}{2\varepsilon_0 V}} \left(\hat{a}^\dagger e^{i\mathbf{kr}} + \hat{a} e^{-i\mathbf{kr}} \right), \tag{4.4}$$

where $\boldsymbol{\epsilon}_{\mathbf{k}}$ denotes the polarization vector, ε_0 gives the permittivity of vacuum, $\omega_{\mathbf{k}}$ is the frequency of the mode and V denotes the volume in which the electromagnetic field is trapped.
We plug Eqs. (4.3) and (4.4) into Eq. (4.1) and get

$$\hat{H}_{\text{int}} = \sum_{\mathbf{k}} g_{\mathbf{k}} \left(\hat{a}^\dagger e^{i\mathbf{kr}} + \hat{a} e^{-i\mathbf{kr}} \right) (\hat{\sigma}_+ + \hat{\sigma}_-), \tag{4.5}$$

where

$$g_{\mathbf{k}} = \sqrt{\frac{\omega_{\mathbf{k}}}{2\varepsilon_0 V}} \boldsymbol{\epsilon}_{\mathbf{k}} \cdot \mathbf{d}, \tag{4.6}$$

denotes the light-matter coupling constant.

4.2 The Jaynes-Cummings model

The first step in deriving the Jaynes-Cummings (JC) Hamiltonian [68] consists of restricting our analysis to only a single mode of the electromagnetic field, meaning that we can drop the sum in Eq. (4.5). Then, we move to the interaction picture defined by

$$\hat{H}_{\text{int}}(t) = e^{i\hat{H}_0 t} \hat{H}_{\text{int}} e^{-i\hat{H}_0 t}, \tag{4.7}$$

where $\hat{H}_0$ denotes the Hamiltonian of the uncoupled TLS and electromagnetic field mode

$$\hat{H}_0 = \frac{\Omega}{2} \hat{\sigma}_z + \omega_{\text{r}} \hat{a}^\dagger \hat{a}. \tag{4.8}$$

The interaction Hamiltonian in the interaction picture is given by

$$\hat{H}_{\text{int}}(t) = g \left(\hat{a}^\dagger \hat{\sigma}_+ e^{i(\Omega+\omega_{\text{r}})t} + \hat{a}\hat{\sigma}_- e^{-i(\Omega+\omega_{\text{r}})t} + \hat{a}^\dagger \hat{\sigma}_- e^{-i(\Omega-\omega_{\text{r}})t} + \hat{a}\hat{\sigma}_+ e^{i(\Omega-\omega_{\text{r}})t} \right). \tag{4.9}$$

We now assume that the frequency of the field mode is close to resonance with the transition frequency of the TLS, i.e. $\Omega \approx \omega_{\text{r}}$. In that case, the terms oscillating at a frequency of $2\omega_{\text{r}}$ in Eq. (4.9) average out to zero over the relevant time scales of the system. We can thus drop those fast-oscillating terms, which is known as the rotating-wave approximation (RWA).
After performing the RWA, we arrive at the JC interaction Hamiltonian [68]

$$\hat{H}_{\text{JC}} = g(\hat{a}^\dagger \hat{\sigma}_- + \hat{a}\hat{\sigma}_+). \tag{4.10}$$

The JC Hamiltonian in Eq. (4.10) commutes with the free Hamiltonian in Eq. (4.8), which means that we can write the eigenstates if the full Hamiltonian $\hat{H}_0 + \hat{H}_{\mathrm{JC}}$ in the lab frame as a linear combination of the degenerate eigenstates of $\hat{H}_0$. These degenerate eigenstates consist of a tensor product between the Fock states of the quantized electromagnetic field $|n\rangle$ and the eigenstates of the TLS $|g\rangle$ and $|e\rangle$. We denote by $|n, e\rangle$ the state where n photons are in the resonator and the TLS is in its excited state and by $|n+1, g\rangle$ the state where $n+1$ photons are in the resonator and the TLS is in its ground state. In the subspace spanned by $\{|n, e\rangle, |n+1, g\rangle\}$, the full Hamiltonian can be written as a 2×2 matrix of the form

$$\hat{H} = \begin{pmatrix} \omega_{\mathrm{r}}(n+1/2) & \sqrt{n+1}g \\ \sqrt{n+1}g & \omega_{\mathrm{r}}(n+1/2) \end{pmatrix}. \tag{4.11}$$

Diagonalizing the matrix in Eq. (4.11) gives the following eigenspectrum

$$\begin{aligned} E_{\pm}(n) &= \omega_{\mathrm{r}} \left(n + \frac{1}{2} \right) \pm \frac{1}{2} \Omega_n^r, \\ |n, \pm\rangle &\equiv \frac{1}{\sqrt{2}} (|n, e\rangle \pm |n+1, g\rangle), \end{aligned} \tag{4.12}$$

where we have introduced the Rabi frequency [67] $\Omega_n^r = 2g\sqrt{n+1}$, which gives the frequency at which the TLS oscillates between its eigenstates by emitting and absorbing a photon. The eigenstates in Eq. (4.12) are called dressed states [67]. We can see that the interaction of the TLS with the field mode lifts the degeneracy between the $|n, e\rangle$ and $|n+1, g\rangle$ states by an amount of Ω_n^r, which is sometimes referred to as an a.c. Stark shift. This particular and non-linear energy scaling between the quantized energy levels is known as the JC ladder [67], see Fig. 4.2.

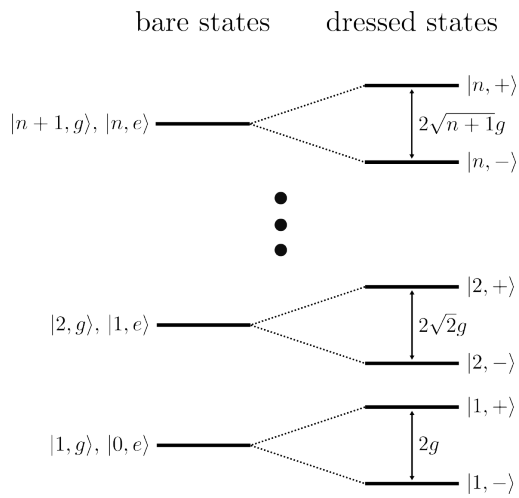

Figure 4.2: Sketch of the JC ladder. The bare, uncoupled states of the cavity and TLS are degenrate. The coupling lifts the degeneracy by an amount of Ω_n^r (see main text) and hybridizes the eigenstates of the two constituent systems. These hybridized states are also called dressed states. The splitting $2g$ for the $n = 0$ state is called vacuum Rabi splitting, as it arises from coupling of the TLS to vacuum fluctuations of the electromagnetic field inside the cavity.

Chapter 5

Transport and Dynamics

So far, we have presented the Hamiltonian descriptions for the DQD, the MR and the coupling between the two. Such Hamiltonian descriptions are able to describe systems that are completely isolated from the outside world. We call such systems also closed. The dynamics of closed systems are then captured by the Schrödinger equation.
In reality, quantum systems are not closed, but usually coupled to some form of environment. These systems are known as open quantum systems [69, 70]. The coupling to the environment is typically not favoured, as it leads to the loss of coherence in the system. Typical examples of such unwanted decoherence are the coupling of solid-state qubits to the electromagnetic environment inside the architecture in which they are embedded [71], or a photon losing the information encoded in its phase while it travels from source to recipient [72].
The coupling to the environment can, however, also be specifically employed for certain tasks. Opening an isolated QD to an environment consisting of fermionic reservoirs allows for the exchange of electrons between the reservoirs and the QD, which can be used to build a single-electron transistor (SET) [3], which we will describe below. Similarly, opening an isolated cavity to the outside world allows photons to leak in, which could then be detected by interacting with a TLS inside the cavity [20], something we will also discuss in detail in this chapter.
As mentioned above, the dynamics of closed systems are described by the Schrödinger equation, where the quantum states are represented by wavefunctions. For open systems, one has to rely on different means to capture the dynamics. A standard tool for this task is the master equation [69, 70, 73], which gives the time evolution of the probability of a system to occupy one of its discrete states and the switching probability between the different states is usually described by a rate matrix. Transport scenarios such as those within the above-mentioned SET can be nicely captured by such master equations. For quantum systems, where coherences are present, one typically has to describe the system using a density

matrix formalism and one has to rely on quantum master equations to correctly analyze the dynamics.
Having developed a formalism for the closed DQD-MR system, we will now open the system to the environment and investigate the photon-assisted transport of electrons through the DQD.

In this chapter, we present a quantum master equation formalism for the DQD-MR system. We also explain how, by opening the system to the environment, it can be used as a detector for microwave photons. In Sec. 5.1, we introduce the classical master equation and use it to study the transport of electrons trough a single QD. In Sec. 5.2, we introduce the quantum master equation and the density matrix formalism. We also derive the general Lindblad master equation, one of the most common tools in the field of open quantum systems, and use it to study the transport of electrons through the DQD-MR system. We then give an explanation of how the DQD-MR system can be used as a single-photon detecor. In Sec. 5.3, we present the equations of motion for the transport through the DQD-MR system.

5.1 Classical master equation

As mentioned above, the classical master equation describes the evolution of a system's occupation probabilities in time. It is thus a set of differential equations of the form [73]

$$\frac{d\mathbf{p}(t)}{dt} = \mathbf{M}(t)\mathbf{p}(t), \tag{5.1}$$

where, for a system consisting of N states, $\mathbf{p}(t)$ is a N-dimensional vector and $\mathbf{M}(t)$ is a $N \times N$ matrix containing the transition rates between the different states. We will focus on the specific case where the rates are time-independent, such that $\mathbf{M}(t) \to \mathbf{M}$.
As the probabilities in $\mathbf{p}(t)$ add up to one, we can derive the following property for the columns of $\mathbf{M}$

$$\frac{d}{dt}\sum_k p_k(t) = 0 = \sum_{l,k} M_{lk}p_k(t) \Rightarrow \sum_l M_{lk} = 0, \tag{5.2}$$

meaning that the entries of each column in $\mathbf{M}$ have to add up to zero.
When studying these transport processes involving transitions between different states, it often occurs that after a given time, the system reaches the so-called steady state, in which the occupation probabilities do not change with time. This steady state corresponds to setting the left-hand side of Eq. (5.1) to zero.

We will now employ the master equation to study one of the most simple transport systems, the SET.

5.1.1 Master equation for a SET

A SET consists of a QD coupled to two fermionic reservoirs [70], see Fig. 5.1. The fermi-

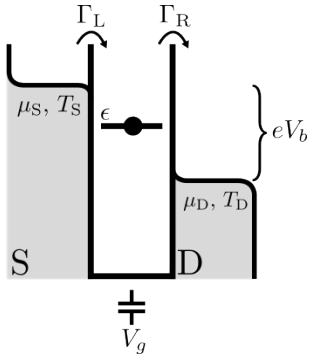

Figure 5.1: The single-electron transistor (SET). A QD with energy level ϵ is coupled to two femrionic leads called source (S) and drain (D), both having a respective chemical potential $\mu_{\mathrm{S,D}}$ and temperature $T_{\mathrm{S,D}}$. The electronic level is tuned by a gate voltage V_g and there is also an applied bias eV_b across S and D. If ϵ lies within the bias window, electrons from S can tunnel into the QD with rate Γ_{L} and out of the QD to D with rate Γ_{R}, leading to an electrical current through the SET.

onic reservoirs are typically called source and drain and are described by the Fermi-Dirac distributions

$$f_{\mathrm{S}}(\epsilon) = \frac{1}{e^{(\epsilon-\mu_{\mathrm{S}})/(k_B T_{\mathrm{S}})}+1}, \qquad f_{\mathrm{D}}(\epsilon) = \frac{1}{e^{(\epsilon-\mu_{\mathrm{D}}-eV_b)/(k_B T_{\mathrm{D}})}+1}, \tag{5.3}$$

respectively, where ϵ denotes the energy of the electron state, $\mu_{\mathrm{S,D}}$ is the chemical potential of the reservoirs and $T_{\mathrm{S,D}}$ gives their temperature, and k_B is the Boltzmann constant. We further apply a voltage bias between source and drain, which is given by eV_b. A voltage V_g can be applied to the QD, such that the energy level can be tuned. If the level is within the bias window, an electron from the source can tunnel into the QD with a rate Γ_{L}. It can then leave the QD with a rate Γ_{R}. This leads to an electrical current through the SET. Depending on the amount of bias and gate voltage applied, there are regions where electrons flow and regions where the flow is energetically forbidden due to Coulomb blockade. These regions without any current form so-called Coulomb diamonds in V_g-V_b space.
We now want to set up the master equation for the transport of electrons through the SET. We work in the limit of large applied bias $eV_b \gg k_B T_{\mathrm{S,D}}, \Gamma_{\mathrm{L,R}}$ and zero temperature $T_{\mathrm{S,D}} \to 0$. The QD can be either empty or full. We denote the probabilities to be in these two states by $p_0(t)$ for the empty state and $p_1(t)$ for the full state. The state of the system undergoes the following transitions with the respective rates $0 \xrightarrow{\Gamma_{\mathrm{L}}} 1 \xrightarrow{\Gamma_{\mathrm{R}}} 0$. Since the columns of the rate matrix have to add up to zero, we find

$$\frac{d}{dt}\begin{pmatrix} p_0(t) \\ p_1(t) \end{pmatrix} = \begin{pmatrix} -\Gamma_{\mathrm{L}} & \Gamma_{\mathrm{R}} \\ \Gamma_{\mathrm{L}} & -\Gamma_{\mathrm{R}} \end{pmatrix}\begin{pmatrix} p_0(t) \\ p_1(t) \end{pmatrix}. \tag{5.4}$$

The particle current through the dot can be found by taking into account all electrons tunneling out from the QD to the drain. It can thus be defined as

$$I(t)/e = \Gamma_{\mathrm{R}} p_1(t). \tag{5.5}$$

We can find the steady-state current by setting the left-hand side of Eq. (5.4) to zero and solving for $p_1(t)$. We find

$$I/e = \frac{\Gamma_{\mathrm{L}}\Gamma_{\mathrm{R}}}{\Gamma_{\mathrm{L}} + \Gamma_{\mathrm{R}}}. \tag{5.6}$$

5.2 Quantum master equation

In quantum systems, we have to take into account statistical mixtures that may arise between the different possible eigenstates when describing the time evolution of the system's occupation probabilities. These statistical mixtures are not captured by the wavefunction formalism of quantum mechanics, which is why we have to employ the density matrix formalism [74].

5.2.1 Density matrix formalism

The density matrix of a pure state is defined as the outer product of the system's wavefunction, typically represented by a state vector $|\psi(t)\rangle$, with its conjugate

$$\hat{\rho}(t) = |\psi(t)\rangle\langle\psi(t)| \,. \tag{5.7}$$

Expanding the state vector in terms of the system's eigenstates $|n\rangle$

$$|\psi(t)\rangle = \sum_n c_n(t) \, |n\rangle \,, \tag{5.8}$$

we can write the density matrix as

$$\hat{\rho}(t) = \sum_{n,m} c_n(t) c_m^*(t) \, |n\rangle\langle m| = \sum_{n,m} \rho_{nm}(t) \, |n\rangle\langle m| \,. \tag{5.9}$$

The diagonal density matrix elements $\rho_{nn}(t) = c_n c_n^* = p_n$ describe the probabilities to occupy a given state $|n\rangle$ and the off-diagonal elements $\rho_{nm} = c_n c_m^* e^{-i\omega_{nm}t}$ describe coherent superpositions in the system and are therefore also termed coherences.
If the coherences are zero, we can describe the system with the regular wavefunction. For non-zero coherences, we need the density matrix description. In such a system there is inherent uncertainty or incomplete knowledge regarding the exact state of the system. This

uncertainty is prevalent in the case when the quantum system is coupled to an external environment, which we will focus on in more detail below.
Before continuing, it is important to note that the density matrix can be used to compute the expectation value of an observable $\hat{x}$ through the following relations

$$\langle \hat{x} \rangle = \sum_n p_n \langle n|\hat{x}|n\rangle = \sum_n p_n \mathrm{Tr}\{|n\rangle\langle n|\,\hat{x}\} = \mathrm{Tr}\{\hat{\rho}\hat{x}\}. \tag{5.10}$$

5.2.2 The Lindblad master equation

In a classical scenario like the SET described above, where we deal with a system with no quantum coherences, we saw that the classical master equation was sufficient to describe the dynamics of the occupation probabilities. In a more complicated quantum system, said coherences may be present, and we thus need to employ a quantum master equation. The quantum analogue to the probability vector $\mathbf{p}(t)$ in Eq. (5.1) is the density matrix $\hat{\rho}(t)$. A quantum master equation thus gives the time evolution of the density matrix.
For a closed system, the time evolution of the density matrix is captured by the von Neumann equation [69], which is the density matrix analogue to the Schrödinger equation

$$\partial_t \hat{\rho}(t) = -i[\hat{H}, \hat{\rho}(t)]. \tag{5.11}$$

Our goal now is to derive the famous Lindblad quantum master equation [75] for an open quantum system.
In Fig. 5.2, a sketch of a general open quantum system scenario is depicted. As seen in

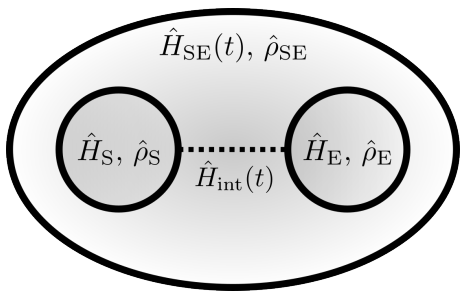

Figure 5.2: Schematic of an open quantum system. A quantum system, described by its Hamiltonian $\hat{H}_{\mathrm{S}}$ and density matrix $\hat{\rho}_{\mathrm{S}}$, is coupled to an environment, which is described by $\hat{H}_{\mathrm{E}}$ and $\hat{\rho}_{\mathrm{E}}$. The system interacts with the environment through an interaction Hamiltonian $\hat{H}_{\mathrm{int}}(t)$. The combined state of the system and environment is described by $\hat{H}_{\mathrm{SE}}$ and $\hat{\rho}_{\mathrm{SE}}$.

the figure, the quantum system is described by the Hamiltonian $\hat{H}_{\mathrm{S}}$ and the environment is described by $\hat{H}_{\mathrm{E}}$. The system and the environment interact through the interaction Hamiltonian $\hat{H}_{\mathrm{int}}(t)$. The total system and environment Hamiltonian is a sum of those three individual Hamiltonians and is denoted by $\hat{H}_{\mathrm{SE}}(t)$. The von Neumann equation

(5.11) for the total density matrix $\hat{\rho}_{\mathrm{SE}}$ is given by (note that we are working in the interaction picture)

$$\partial_t \hat{\rho}_{\mathrm{SE}}(t) = -i[\hat{H}_{\mathrm{int}}(t), \hat{\rho}_{\mathrm{SE}}(t)]. \tag{5.12}$$

Integrating Eq. (5.12), we get

$$\hat{\rho}_{\mathrm{SE}}(t) = \hat{\rho}_{\mathrm{SE}}(0) - \int_0^t ds\, [\hat{H}_{\mathrm{int}}(s), \hat{\rho}_{\mathrm{SE}}(s)]. \tag{5.13}$$

Plugging Eq. (5.13) into (5.12), we get

$$\partial_t \hat{\rho}_{\mathrm{SE}}(t) = -i[\hat{H}_{\mathrm{int}}(t), \hat{\rho}_{\mathrm{SE}}(0)] - \int_0^t ds\, [\hat{H}_{\mathrm{int}}(t), [\hat{H}_{\mathrm{int}}(s), \hat{\rho}_{\mathrm{SE}}(s)]]. \tag{5.14}$$

We assume that the system and the environment have not interacted with each other at time $t = 0$, which means that there are no correlations between the two subsystems, and thus, we can write the total density matrix at that time as a product state $\hat{\rho}_{\mathrm{SE}}(0) = \hat{\rho}_{\mathrm{S}}(0) \otimes \hat{\rho}_{\mathrm{E}}(0)$. Also, since we are mostly interested in the dynamics of the system $\hat{\rho}_{\mathrm{S}}(t)$, we can perform a partial trace on the total density matrix, tracing out the degrees of freedom of the environment $\hat{\rho}_{\mathrm{E}}(t)$. A partial trace is defined by

$$\mathrm{Tr}_{\mathrm{E}}\{\hat{\rho}_{\mathrm{SE}}\} = \sum_n (\hat{\mathbb{1}}_{\mathrm{S}} \otimes \langle n|_{\mathrm{E}}) \hat{\rho}_{\mathrm{SE}} (\hat{\mathbb{1}}_{\mathrm{S}} \otimes |n\rangle_{\mathrm{E}}) = \hat{\rho}_{\mathrm{S}}, \tag{5.15}$$

where $\{|n\rangle_{\mathrm{E}}\}$ is any orthonormal basis for the environment. We arrive at

$$\begin{aligned} \partial_t \hat{\rho}_{\mathrm{S}}(t) &= \mathrm{Tr}_{\mathrm{E}}\{\partial_t \hat{\rho}_{\mathrm{SE}}(t)\} \\ &= \mathrm{Tr}_{\mathrm{E}}\{[\hat{H}_{\mathrm{int}}(t), \hat{\rho}_{\mathrm{S}}(0) \otimes \hat{\rho}_{\mathrm{E}}(0)]\} - \int_0^t ds\, \mathrm{Tr}_{\mathrm{E}}\{[\hat{H}_{\mathrm{int}}(t), [\hat{H}_{\mathrm{int}}(s), \hat{\rho}_{\mathrm{SE}}(s)]]\}. \end{aligned} \tag{5.16}$$

The interaction Hamiltonian is, without loss of generality, assumed to be of the form

$$\hat{H}_{\mathrm{int}}(t) = \sum_i \hat{S}_i(t) \otimes \hat{E}_i(t), \tag{5.17}$$

where $\hat{S}_i(t)$ ($\hat{E}_i(t)$) is an operator that acts solely on the system's (environment's) degrees of freedom. Using this form of the interaction Hamiltonian, we can write the first term on the right-hand side of Eq. (5.16) as

$$\begin{aligned} \mathrm{Tr}_{\mathrm{E}}\{[\hat{H}_{\mathrm{int}}(t), \hat{\rho}_{\mathrm{S}}(0) \otimes \hat{\rho}_{\mathrm{E}}(0)]\} = &\sum_i \hat{S}_i(t) \hat{\rho}_{\mathrm{S}}(0) \mathrm{Tr}_{\mathrm{E}}\{\hat{E}_i(t) \hat{\rho}_{\mathrm{E}}(0)\} \\ &- \sum_i \hat{\rho}_{\mathrm{S}}(0) \hat{S}_i(t) \mathrm{Tr}_{\mathrm{E}}\{\hat{\rho}_{\mathrm{E}}(0) \hat{E}_i(t)\}. \end{aligned} \tag{5.18}$$

Without loss of generality, we can assume that this term is zero. If it is not zero, we can always rewrite the Hamiltonian as

$$\hat{H}_{\mathrm{SE}} = \hat{H}_{\mathrm{S}} + \hat{H}' + \hat{H}_{\mathrm{E}} + \hat{H}_{\mathrm{int}} - \hat{H}', \quad \hat{H}' = \sum_i \hat{S}_i \langle \hat{E}_i \rangle, \tag{5.19}$$

where $\langle \hat{E}_i \rangle = \mathrm{Tr}\{\hat{E}_i \hat{\rho}_{\mathrm{E}}\}$ and note also that we have dropped the time variable for ease of notation. We see that the system Hamiltonian is changed by a shift in energy which does not change the dynamics.
We are left with the second term on the right-hand side of Eq. (5.16)

$$\partial_t \hat{\rho}_{\mathrm{S}}(t) = -\int_0^t ds\, \mathrm{Tr}_{\mathrm{E}}\{[\hat{H}_{\mathrm{int}}(t), [\hat{H}_{\mathrm{int}}(s), \hat{\rho}_{\mathrm{SE}}(s)]]\}. \tag{5.20}$$

This equation still includes the state of the full system $\hat{\rho}_{\mathrm{SE}}(t)$. To simplify the equation, we assume that the environment is large and only weakly coupled to the system, such that the time scales of the environment and of the correlations between system and environment are much shorter than the typical times scales over which the system varies significantly. We can thus decouple both subsystems at all times and write the total density matrix as $\hat{\rho}_{\mathrm{SE}}(t) = \hat{\rho}_{\mathrm{S}}(t) \otimes \hat{\rho}_{\mathrm{E}}(0)$. This is known as the Born approximation [69]. Eq. (5.20) thus becomes

$$\partial_t \hat{\rho}_{\mathrm{S}}(t) = -\int_0^t ds\, \mathrm{Tr}_{\mathrm{E}}\{[\hat{H}_{\mathrm{int}}(t), [\hat{H}_{\mathrm{int}}(s), \hat{\rho}_{\mathrm{S}}(s) \otimes \hat{\rho}_{\mathrm{E}}(0)]]\}. \tag{5.21}$$

This equation is difficult to solve since the dynamics at time t depends on the state of the system at all previous times. A further approximation we take is the Markov approximation. To that end, we bring Eq. (5.21) to a form that is local in time by replacing $\hat{\rho}_{\mathrm{S}}(s)$ with $\hat{\rho}_{\mathrm{S}}(t)$. We also substitute the time variable in the integral s by $t - s$ and extend the upper bound of the integral to infinity and obtain a Markovian master equation [69]

$$\partial_t \hat{\rho}_{\mathrm{S}}(t) = -\int_0^\infty ds\, \mathrm{Tr}_{\mathrm{E}}\{[\hat{H}_{\mathrm{int}}(t), [\hat{H}_{\mathrm{int}}(t-s), \hat{\rho}_{\mathrm{S}}(t) \otimes \hat{\rho}_{\mathrm{E}}(0)]]\}. \tag{5.22}$$

Eq. (5.22) is known as the Redfield master equation [76] and it does not guarantee complete positivity of the density matrix. To guarantee complete positivity, we need to take one final approximation, the secular approximation [69]. We start by assuming that we know the eigenvalues λ of the system Hamiltonian $\hat{H}_{\mathrm{S}}$ and its projectors onto the eigenstates $\hat{\Pi}(\lambda)$. We can then project the system operators $\hat{S}$ (note that we start by working in the Schrödinger picture here) on subspaces with fixed energy difference ω

$$\hat{S}(\omega) = \sum_{\lambda' - \lambda = \omega} \hat{\Pi}(\lambda) \hat{S} \hat{\Pi}(\lambda'). \tag{5.23}$$

In the interaction picture, the system operators in Eq. (5.23) are changed to $\hat{S}(\omega) \rightarrow e^{-i\omega t}\hat{S}(\omega)$ and $\hat{S}^\dagger(\omega) \rightarrow e^{i\omega t}\hat{S}^\dagger(\omega)$. Plugging this into the interaction Hamiltonian, we get

$$\hat{H}'_{\text{int}}(t) = \sum_{j,\omega} e^{-i\omega t}\hat{S}_j(\omega) \otimes \hat{E}_j(t) = \sum_{j,\omega} e^{i\omega t}\hat{S}_j^\dagger(\omega) \otimes \hat{E}_j^\dagger(t). \tag{5.24}$$

Inserting Eq. (5.24) into the Redfield equation (5.22) gives

$$\begin{aligned}\partial_t\hat{\rho}_{\text{S}}(t) = &\sum_{\omega,\omega',j,k} e^{i(\omega'-\omega)t}\Lambda_{kj}(\omega)[\hat{S}_j(\omega)\hat{\rho}_{\text{S}}(t), \hat{S}_k^\dagger(\omega')] \\ &+ \sum_{\omega,\omega',j,k} e^{i(\omega-\omega')t}\Lambda_{jk}^*(\omega')[\hat{S}_j(\omega), \hat{\rho}_{\text{S}}(t)\hat{S}_k^\dagger(\omega')],\end{aligned} \tag{5.25}$$

where we have introduced the one-sided Fourier transform of the environment correlation functions

$$\begin{aligned}\Lambda_{kj}(\omega) &= \int_0^\infty ds\, e^{i\omega s}\text{Tr}_{\text{E}}\{\hat{E}_j^\dagger(t)\hat{E}_k(t-s)\hat{\rho}_{\text{E}}(0)\} \\ &= \int_0^\infty ds\, e^{i\omega s}\text{Tr}_{\text{E}}\{\hat{E}_j^\dagger(s)\hat{E}_k(0)\hat{\rho}_{\text{E}}(0)\},\end{aligned} \tag{5.26}$$

where we have assumed that the environment correlation functions are homogeneous in time. The secular approximation constitutes dropping all terms where $\omega \neq \omega'$. We thus assume that all those terms oscillate at a frequency that is much faster than the timescale of the system. We obtain

$$\partial_t\hat{\rho}_{\text{S}}(t) = \sum_{\omega,j,k}\left(\Lambda_{kj}(\omega)[\hat{S}_j(\omega)\hat{\rho}_{\text{S}}(t), \hat{S}_k^\dagger(\omega)] + \Lambda_{jk}^*(\omega)[\hat{S}_j(\omega), \hat{\rho}_{\text{S}}(t)\hat{S}_k^\dagger(\omega)]\right). \tag{5.27}$$

To cast the master equation (5.27) into Lindblad form, we split the the coefficients $\Gamma_{kj}(\omega)$ in Eq. (5.26) into their real and imaginary parts

$$\Lambda_{kj}(\omega) = \frac{1}{2}\alpha_{kj}(\omega) + \beta_{kj}(\omega), \tag{5.28}$$

where

$$\begin{aligned}\alpha_{kj}(\omega) &= \Lambda_{kj}(\omega) + \Lambda_{kj}^*(\omega) = \int ds\, e^{i\omega s}\text{Tr}_{\text{E}}\{\hat{E}_k^\dagger(s)\hat{E}_j(0)\hat{\rho}_{\text{E}}(0)\}, \\ \beta_{kj}(\omega) &= \frac{-i}{2}(\Lambda_{kj}(\omega) - \Lambda_{kj}^*(\omega)).\end{aligned} \tag{5.29}$$

The master equation (5.27) can now be divided into Hermitian and non-Hermitian parts

$$\begin{aligned}\partial_t\hat{\rho}_{\text{S}}(t) = &-i[\hat{H}_{\text{LS}}, \hat{\rho}_{\text{S}}(t)] \\ &+ \sum_{\omega,k,j}\alpha_{kj}(\omega)\left(\hat{S}_j(\omega)\hat{\rho}_{\text{S}}(t)\hat{S}_k^\dagger(\omega) - \frac{1}{2}\{\hat{S}_k^\dagger(\omega)\hat{S}_j(\omega), \hat{\rho}_{\text{S}}(t)\}\right),\end{aligned} \tag{5.30}$$

where we have introduced the so-called Lamb shift Hamiltonian
$\hat{H}_{\mathrm{LS}} = \sum_{\omega,k,j} \beta_{kj}(\omega)\hat{S}_k^\dagger(\omega)\hat{S}_j(\omega)$, which leads to a renormalization of the system's energy levels due to the interaction with the environment and is typically dropped. We can easily verify that the matrix formed by $\alpha_{kj}(\omega)$ is positive and it can thus be diagonalized. After diagonalizing Eq. (5.30) and moving back to the Schrödinger picture, we arrive at the Lindblad [75] (or Lindblad-Gorini-Kossakowski-Sudarshan [77]) master equation

$$\partial_t \hat{\rho}_{\mathrm{S}}(t) = -i[\hat{H}_{\mathrm{S}}, \hat{\rho}_{\mathrm{S}}(t)] + \sum_j \left(\hat{L}_j \hat{\rho}_{\mathrm{S}}(t) \hat{L}_j^\dagger - \frac{1}{2} \left\{ \hat{L}_j^\dagger \hat{L}_j, \hat{\rho}_{\mathrm{S}}(t) \right\} \right) = \mathcal{L}\hat{\rho}_{\mathrm{S}}(t), \quad (5.31)$$

where the operators $\hat{L}_j$ are usually called jump operators and $\mathcal{L}$ is referred to as Liouvillian.

5.2.3 Lindblad master equation for the DQD-MR system

Having derived the general form of the Lindblad master equation (5.31), we want to apply it to the DQD-MR system. The system Hamiltonians for the DQD and the MR are given in Secs. 2 and 3, respectively.
We start by giving the coupling between the field inside the MR and the dipole between the two charge states of the DQD [78]

$$\hat{H}_{\mathrm{MD}} = g_0(\hat{a}^\dagger + \hat{a})\hat{\tau}_z, \quad (5.32)$$

where g_0 denotes the bare coupling between the field and the dipole and $\hat{\tau}_z = |L\rangle\langle L| - |R\rangle\langle R|$. Moving to the eigenstate basis of the DQD defined in Eq. (2.16), we find

$$\hat{H}_{\mathrm{MD}} = g_0(\hat{a}^\dagger + \hat{a})(\hat{\sigma}_x \sin(\theta) - \hat{\sigma}_z \cos(\theta)). \quad (5.33)$$

Performing the RWA, we remove the term proportional to σ_z and also the terms rotating at higher frequencies and obtain the JC Hamiltonian

$$\hat{H}_{\mathrm{JC}} = g(\hat{a}^\dagger \hat{\sigma}_- + \hat{a}\hat{\sigma}_+), \quad (5.34)$$

where $g = g_0 \sin(\theta)$.
There is one more component to the system Hamiltonian we have not yet touched upon. In order for photons to be present in the MR, we need a microwave drive that feeds them into the MR. We model this drive as a coherent, monochromatic source of microwave radiation with the Hamiltonian [79]

$$\hat{H}_{\mathrm{DR}} = \sqrt{\kappa_{\mathrm{in}} \dot{N}}(\hat{a}^\dagger e^{i\omega_{\mathrm{d}} t} + \hat{a}e^{-i\omega_{\mathrm{d}} t}), \quad (5.35)$$

where κ_{in} denotes the coupling between the drive and the MR, $\dot{N}$ gives the rate of photons impinging on the MR and ω_{d} is the frequency of the drive. We derive the drive Hamiltonian in Eq. (5.35) using input-output theory, see App. A.

The total system Hamiltonian is given by $\hat{H}_{\mathrm{S}} = \hat{H}_{\mathrm{DQD}} + \hat{H}_{\mathrm{MR}} + \hat{H}_{\mathrm{JC}} + \hat{H}_{\mathrm{DR}}$. Further calculations are simplified by moving to the frame rotating at the frequency ω_{d} of the drive. This is done by a unitary operator $\hat{\mathcal{U}} = \exp\big(i\omega_{\mathrm{d}} t(\hat{a}^\dagger \hat{a} + \hat{\sigma}_z/2)\big)$

$$\begin{aligned}\hat{\mathcal{H}}_{\mathrm{S}} &= \hat{\mathcal{U}}^\dagger \hat{H}_{\mathrm{S}} \hat{\mathcal{U}} + i\partial_t \hat{\mathcal{U}} \hat{\mathcal{U}}^\dagger \\ &= \frac{\Delta_{\mathrm{d}}}{2}\hat{\sigma}_z + \Delta_{\mathrm{r}} \hat{a}^\dagger \hat{a} + g(\hat{a}^\dagger \hat{\sigma}_- + \hat{a}\hat{\sigma}_+) + \sqrt{\kappa_{\mathrm{in}} \dot{N}}(\hat{a}^\dagger + \hat{a}),\end{aligned} \tag{5.36}$$

where $\Delta_{\mathrm{d}} = \Omega - \omega_{\mathrm{d}}$ ($\Delta_{\mathrm{r}} = \omega_{\mathrm{r}} - \omega_{\mathrm{d}}$) gives the detuning between the DQD (MR) and the drive.
We will now shift our focus on the environment Hamiltonian $\hat{H}_{\mathrm{E}}$. Similarly to the SET, we couple the DQD to a source and a drain. The Hamiltonian for those fermionic reservoirs is given by [80]

$$\hat{H}_{\mathrm{F}} = \sum_{k,\alpha} \epsilon_{k,\alpha} \hat{c}^\dagger_{k,\alpha} \hat{c}_{k,\alpha}, \tag{5.37}$$

where $\epsilon_{k,\alpha}$ denotes the energy of an electron in the k-th mode of lead α, where $\alpha \in \{\mathrm{L},\mathrm{R}\}$, and $\hat{c}^\dagger_{k,\alpha}$ ($\hat{c}_{k,\alpha}$) is the fermionic operator creating (destroying) an electronic excitation in the k-th mode of lead α. Note that we have used the notation for left (L) and right (R), as the source only couples to the left QD and the drain only couples to the right QD. This will simplify the overall notation later on. Furthermore, the coupling of the DQD to the environment introduces the state $|0\rangle$, where no electron is present on the DQD, to the total electronic Hilbert space. Without loss of generality, we set the energy of the empty state to zero. For the MR, the environment is modeled as a bosonic bath and the Hamiltonian is given by [81]

$$\hat{H}_{\mathrm{B}} = \sum_q \omega_q \hat{b}^\dagger_q \hat{b}_q, \tag{5.38}$$

where ω_q denotes the frequency of the q-th mode and $\hat{b}^\dagger_q$ ($\hat{b}_q$) creates (destroys) a photon in the q-th mode. The total environment Hamiltonian is given by $\hat{H}_{\mathrm{E}} = \hat{H}_{\mathrm{F}} + \hat{H}_{\mathrm{B}}$.
The next component we need is the interaction Hamiltonian $\hat{H}'_{\mathrm{int}}$, which we will introduce in the Schrödinger picture. The coupling between the fermionic leads and the DQD is described by [80]

$$\hat{H}_{\mathrm{FD}} = \sum_{k,\alpha} (\mu_{k,\alpha} \hat{s}^\dagger_\alpha \hat{c}_{k,\alpha} + \mathrm{h.c.}), \tag{5.39}$$

where $\mu_{k,\alpha}$ denotes the coupling between the leads and the QDs. The operator $\hat{s}^\dagger_\alpha = |\alpha\rangle\langle 0|$ creates and electronic excitation in $|\alpha\rangle$. The coupling between the bosonic bath and the MR is described by [81]

$$\hat{H}_{\mathrm{BR}} = \sum_q (\nu_q \hat{a}^\dagger \hat{b}_q + \mathrm{h.c.}), \tag{5.40}$$

where ν_q denotes the coupling between the photons in the MR and the photons in the q-th mode in the bath. The total interaction Hamiltonian is given by $\hat{H}_{\mathrm{int}} = \hat{H}_{\mathrm{FD}} + \hat{H}_{\mathrm{BR}}$.

Moving to the interaction picture, the system and environment operators become

$$\begin{aligned}
\hat{s}_{\mathrm{L}}(t) &= \cos(\theta/2)\hat{s}_g e^{-iE_g t} + \sin(\theta/2)\hat{s}_e e^{-iE_e t}, \\
\hat{s}_{\mathrm{R}}(t) &= -\sin(\theta/2)\hat{s}_g e^{-iE_g t} + \cos(\theta/2)\hat{s}_e e^{-iE_e t}, \\
\hat{a}(t) &= e^{-i\omega_{\mathrm{r}} t}\hat{a}, \\
\hat{c}_{k,\alpha}(t) &= e^{-i\epsilon_{k,\alpha} t}\hat{c}_{k,\alpha}, \\
\hat{b}_q(t) &= e^{-i\omega_q t}\hat{b}_q,
\end{aligned} \tag{5.41}$$

where we have defined $\hat{s}_g = |0\rangle\langle g|$ ($\hat{s}_e = |0\rangle\langle e|$) as the operator creating (destroying) and excitation in the DQD ground (excited) state and $E_g = -\Omega/2$ ($E_e = \Omega/2$) is the energy of the ground (excited) state. We further employ the following relations [69]

$$\begin{aligned}
&\mathrm{Tr}_{\mathrm{E}}\{\hat{c}^\dagger_{k,\alpha}\hat{c}_{k,\alpha}\hat{\rho}_{\mathrm{E}}(0)\} = f_\alpha(\epsilon_{k,\alpha}), \\
&\mathrm{Tr}_{\mathrm{E}}\{\hat{c}_{k,\alpha}\hat{c}^\dagger_{k,\alpha}\hat{\rho}_{\mathrm{E}}(0)\} = 1 - f_\alpha(\epsilon_{k,\alpha}), \\
&\mathrm{Tr}_{\mathrm{E}}\{(\hat{b}^\dagger_q\hat{b}_q\hat{\rho}_{\mathrm{E}}(0)\} = n_B(\omega_q), \\
&\mathrm{Tr}_{\mathrm{E}}\{\hat{b}_q\hat{b}^\dagger_q\hat{\rho}_{\mathrm{E}}(0)\} = 1 + n_B(\omega_q), \\
&\Gamma_\alpha(\omega) = 2\pi\sum_{k,\alpha}|\mu_{k,\alpha}|^2\delta(\omega - \epsilon_{k,\alpha}), \\
&\kappa(\omega) = 2\pi\sum_{q}|\nu_q|^2\delta(\omega - \omega_q),
\end{aligned} \tag{5.42}$$

where $n_B(\omega_q) = 1/(e^{\omega_q/k_B T} - 1)$ is the Bose-Einstein distribution and $f_\alpha(\epsilon_{k,\alpha})$ is the Fermi-Dirac distribution, c.f. Eq. (5.3). We will also make use of the following integral relation

$$\lim_{t\to\infty}\int_0^t dt' e^{ixt'} = \pi\delta(x) + iP\left(\frac{1}{x}\right), \tag{5.43}$$

where P denotes Cauchy's principle value of integration. Plugging Eqs. (5.41), (5.42) and (5.43) into Eq. (5.30), we obtain

$$\begin{aligned}
\partial_t \hat{\rho}_{\mathrm{S}}(t) = &- i[\hat{H}_{\mathrm{LS}}, \hat{\rho}_{\mathrm{S}}(t)] \\
&+ (\Gamma_{g\mathrm{L}}(E_g) + \Gamma_{g\mathrm{R}}(E_g)) \left(\hat{s}_g^\dagger \hat{\rho}_{\mathrm{S}}(t) \hat{s}_g - \frac{1}{2}\{\hat{s}_g \hat{s}_g^\dagger, \hat{\rho}_{\mathrm{S}}(t)\} \right) \\
&+ (\Gamma_{\mathrm{L}g}(E_g) + \Gamma_{\mathrm{R}g}(E_g)) \left(\hat{s}_g \hat{\rho}_{\mathrm{S}}(t) \hat{s}_g^\dagger - \frac{1}{2}\{\hat{s}_g^\dagger \hat{s}_g, \hat{\rho}_{\mathrm{S}}(t)\} \right) \\
&+ (\Gamma_{\mathrm{L}e}(E_e) + \Gamma_{\mathrm{R}e}(E_e)) \left(\hat{s}_e \hat{\rho}_{\mathrm{S}}(t) \hat{s}_e^\dagger - \frac{1}{2}\{\hat{s}_e^\dagger \hat{s}_e, \hat{\rho}_{\mathrm{S}}(t)\} \right) \\
&+ (\Gamma_{e\mathrm{L}}(E_e) + \Gamma_{e\mathrm{R}}(E_e)) \left(\hat{s}_e^\dagger \hat{\rho}_{\mathrm{S}}(t) \hat{s}_e - \frac{1}{2}\{\hat{s}_e \hat{s}_e^\dagger, \hat{\rho}_{\mathrm{S}}(t)\} \right) \\
&+ \kappa(\omega_{\mathrm{r}})(1 + n_B(\omega_{\mathrm{r}})) \left(\hat{a} \hat{\rho}_{\mathrm{S}}(t) \hat{a}^\dagger - \frac{1}{2}\{\hat{a}^\dagger \hat{a}, \hat{\rho}_{\mathrm{S}}(t)\} \right), \\
&+ \kappa(\omega_{\mathrm{r}}) n_B(\omega_{\mathrm{r}}) \left(\hat{a}^\dagger \hat{\rho}_{\mathrm{S}}(t) \hat{a} - \frac{1}{2}\{\hat{a} \hat{a}^\dagger, \hat{\rho}_{\mathrm{S}}(t)\} \right)
\end{aligned} \tag{5.44}$$

where we have defined the effective rates

$$\begin{aligned}
\Gamma_{g\mathrm{L}}(E_g) &= \Gamma_{\mathrm{L}}(E_g) f_{\mathrm{L}}(E_g) \cos^2(\theta/2), \\
\Gamma_{g\mathrm{R}}(E_g) &= \Gamma_{\mathrm{R}}(E_g) f_{\mathrm{R}}(E_g) \sin^2(\theta/2), \\
\Gamma_{\mathrm{L}g}(E_g) &= \Gamma_{\mathrm{L}}(E_g)(1 - f_{\mathrm{L}}(E_g)) \cos^2(\theta/2), \\
\Gamma_{\mathrm{R}g}(E_g) &= \Gamma_{\mathrm{R}}(E_g)(1 - f_{\mathrm{R}}(E_g)) \sin^2(\theta/2), \\
\Gamma_{e\mathrm{L}}(E_e) &= \Gamma_{\mathrm{L}}(E_e) f_{\mathrm{L}}(E_e) \sin^2(\theta/2), \\
\Gamma_{e\mathrm{R}}(E_e) &= \Gamma_{\mathrm{R}}(E_e) f_{\mathrm{R}}(E_e) \cos^2(\theta/2), \\
\Gamma_{\mathrm{L}e}(E_e) &= \Gamma_{\mathrm{L}}(E_e)(1 - f_{\mathrm{L}}(E_e)) \sin^2(\theta/2), \\
\Gamma_{\mathrm{R}e}(E_e) &= \Gamma_{\mathrm{R}}(E_e)(1 - f_{\mathrm{R}}(E_e)) \cos^2(\theta/2).
\end{aligned} \tag{5.45}$$

The rates in Eq. (5.45) are the tunneling rates of electrons into and out of the DQD ground and excited state, respectively. The subscript has to be read from right to left. For example, $\Gamma_{g\mathrm{L}}(E_g)$ denotes the rate of an electron tunneling from the source to the ground state. The rate $\kappa(\omega_{\mathrm{r}})$ is the rate of photons leaving the MR. Under the Born-Markov approximation, the bare rates $\Gamma_\alpha(E_{g,e})$ are supposed to be small, such that their spectral profile is essentially flat and we drop their dependence on the energies $E_{g,e}$. In the main part of the thesis, we will focus on the scenario where the chemical potentials of the leads are set to the energy of the empty DQD state. We will also assume that the temperature of the environment is much smaller than the splitting level splitting of the DQD, i.e. $k_b T \ll \hbar\Omega$. With these assumptions, we can set $f_{\mathrm{L,R}}(E_g) \to 1$, $f_{\mathrm{L,R}}(E_e) \to 0$ and $n_B(\omega_{\mathrm{r}}) \to 0$. For ease of

notation, we also introduce the Lindblad dissipator

$$\mathcal{D}[\hat{A}]\hat{\rho} = \hat{A}\hat{\rho}\hat{A}^\dagger - \frac{1}{2}\{\hat{A}^\dagger\hat{A}, \hat{\rho}\}. \tag{5.46}$$

With these assumptions, we get the following Lindblad master equation for the DQD-MR system in the Schrödinger picture and omitting the Lamb-shift Hamiltonian $\hat{H}_{\mathrm{LS}}$

$$\partial_t\hat{\rho}_{\mathrm{S}}(t) = -i[\hat{\mathcal{H}}_{\mathrm{S}}, \hat{\rho}_{\mathrm{S}}(t)] + \Gamma_{g0}\mathcal{D}[\hat{s}_g^\dagger]\hat{\rho}_{\mathrm{S}}(t) + \Gamma_{0e}\mathcal{D}[\hat{s}_e]\hat{\rho}_{\mathrm{S}}(t) + \kappa\mathcal{D}[\hat{a}]\hat{\rho}_{\mathrm{S}}(t), \tag{5.47}$$

where we have defined

$$\Gamma_{g0} = \Gamma_{g\mathrm{L}} + \Gamma_{g\mathrm{R}}, \quad \Gamma_{0e} = \Gamma_{\mathrm{L}e} + \Gamma_{\mathrm{R}e}. \tag{5.48}$$

We see that, under our assumptions, electrons from the leads can only enter the DQD ground state and leave from the excited state.

Decoherence

An important factor influencing the transport in the DQD-MR system is decoherence. We will focus here on two decoherence mechanisms that affect the state of the DQD. The first one is dephasing, which arises due to fluctuations in the electromagnetic environment [82]. The second one is relaxation and thermal excitation of an electron, which arises due to coupling of the DQD to phonons in the solid-state environment [83].
Pure dephasing describes the decay of the phase-coherence between the overlap of the DQD eigenstates. As mentioned above, this dephasing arises due to fluctuations in the environment, which we will model by a stochastic, time-dependent process $\delta(t)$ [84]. It is added to the DQD Hamiltonian in the following way

$$\hat{H}_{\mathrm{DQD}} = \frac{1}{2}(\Omega + \delta(t))\hat{\sigma}_z, \tag{5.49}$$

The time evolution of the density matrix can then be described by the following operator

$$\hat{U}(t) = \exp\left(-\frac{i}{2}(\Omega t + \phi(t))\hat{\sigma}_z\right), \tag{5.50}$$

where $\phi(t) = \int_0^t \delta(s)ds$. Acting with this unitary on the density matrix will lead to

$$\hat{\rho}_{\mathrm{S}}(t) = \hat{U}(t)\hat{\rho}_{\mathrm{S}}(0)\hat{U}^\dagger(t) = \begin{pmatrix} \rho_{gg} & e^{-i\Omega t}e^{-i\phi(t)}\rho_{ge} \\ e^{i\Omega t}e^{i\phi(t)}\rho_{eg} & \rho_{ee} \end{pmatrix}, \tag{5.51}$$

where $\rho_{ij} = \langle i|\hat{\rho}_{\mathrm{S}}|j\rangle$. We can see that indeed only the off-diagonal elements are effected by the fluctuations in the environment. In order to get a reasonable estimate of the dephasing

time scales, it is useful to average over all the possible realizations of the stochastic process. We will denote this classical expectation value by $\langle ... \rangle_\phi$

$$\langle \hat{\rho}_{\mathrm{S}}(t) \rangle_\phi = \begin{pmatrix} \rho_{00} & \zeta(t)\rho_{01} \\ \zeta^*(t)\rho_{10} & \rho_{11} \end{pmatrix}, \tag{5.52}$$

where $\zeta(t) = \left\langle e^{-i\phi(t)} \right\rangle_\phi$ is the so-called decoherence function. For a Markovian process, it is usually modeled as $\zeta(t) = e^{-t/T_2}$, where T_2 is the dephasing time.
Evaluating the ensemble-averaged density matrix explicitly gives us

$$\langle \hat{\rho}_{\mathrm{S}}(t) \rangle_\phi = \int d\phi \, q(\phi) \hat{U}(t) \hat{\rho}_{\mathrm{S}}(0) \hat{U}^\dagger(t) = (1-p)\hat{\rho}_{\mathrm{S}}(0) + p\hat{\sigma}_z \hat{\rho}_{\mathrm{S}}(0) \hat{\sigma}_z, \tag{5.53}$$

where $p = \int d\phi \, q(\phi) \sin^2(\phi/2)$ with $q(\phi)$ being the distribution of all the possible realizations of $\phi(t)$. By comparison with the previous result we find that $p = \frac{1-\zeta}{2}$. We can now describe the effect of dephasing in the form of a Lindblad dissipator which we can then add to our master equation.
For small times, we can write $\zeta(\delta t) = e^{-\delta t/T_2} \approx 1 - \delta t/T_2$. Thus, we find

$$\langle \hat{\rho}_{\mathrm{S}}(\delta t) \rangle_\phi = \hat{\rho}_{\mathrm{S}} - \frac{\gamma_\phi \delta t}{2} \hat{\rho}_{\mathrm{S}} + \frac{\gamma_\phi \delta t}{2} \hat{\sigma}_z \hat{\rho}_{\mathrm{S}} \hat{\sigma}_z, \tag{5.54}$$

where $\gamma_\phi = 1/T_2$ is the dephasing rate. The differential equation for the density matrix can then be written as (using $\langle \hat{\rho}_{\mathrm{S}}(t) \rangle_\phi = \hat{\rho}_{\mathrm{S}}(t)$)

$$\partial_t \hat{\rho}_{\mathrm{S}}(t) = \lim_{\delta t \to 0} \frac{\hat{\rho}_{\mathrm{S}}(\delta t) - \hat{\rho}_{\mathrm{S}}(0)}{\delta t} = \frac{\gamma_\phi}{2} \mathcal{D}[\hat{\sigma}_z] \hat{\rho}_{\mathrm{S}}(t). \tag{5.55}$$

As mentioned above, the coupling to a phononic environment will cause the DQD states to dissipate or gain energy through relaxation or thermal excitation by the emission or absorption of a phonon, respectively. The Hamiltonians for the phononic bath and the interaction between the DQD and the phonons can be written as

$$\begin{aligned} \hat{H}_{\mathrm{PH}} &= \sum_j \omega_j \hat{d}_j^\dagger \hat{d}_j, \\ \hat{H}_{\mathrm{DP}} &= \sum_j \xi_j (\hat{\sigma}_+ \hat{d}_j + \hat{\sigma}_- \hat{d}_j^\dagger), \end{aligned} \tag{5.56}$$

respectively, where $\hat{d}_j$ ($\hat{d}_j^\dagger$) denoted the phononic annihilation (creation) operator and ξ_j is the coupling constant between the DQD and the phonons.
Following the same steps as in Sec. 5.2.3, we can derive the Lindblad dissipator for the process describing relaxation of an electron from the excited to the ground state of the

DQD. We will neglect thermal excitations due to the small temperature of the environment. The dissipator is given by

$$\gamma_- \mathcal{D}[\hat{\sigma}_-]\hat{\rho}_{\mathrm{S}}(t), \quad \gamma_-(\omega) = 2\pi \sum_j |\beta_j|^2 \delta(\omega - \omega_j), \tag{5.57}$$

where γ_- denotes the relaxation rate.
We add the decoherence dissipators to our master equation (5.47) and get

$$\begin{aligned} \partial_t \hat{\rho}_{\mathrm{S}}(t) = &- i[\hat{\mathcal{H}}, \hat{\rho}_{\mathrm{S}}(t)] + \Gamma_{g0}\mathcal{D}[\hat{s}_g^\dagger]\hat{\rho}_{\mathrm{S}}(t) + \Gamma_{0e}\mathcal{D}[\hat{s}_e]\hat{\rho}_{\mathrm{S}}(t) \\ &+ \frac{\gamma_\phi}{2}\mathcal{D}[\hat{\sigma}_z]\hat{\rho}_{\mathrm{S}}(t) + \gamma_-\mathcal{D}[\hat{\sigma}_-]\hat{\rho}_{\mathrm{S}}(t) + \kappa\mathcal{D}[\hat{a}]\hat{\rho}_{\mathrm{S}}(t). \end{aligned} \tag{5.58}$$

5.2.4 The single-photon detector

In our system and under our specific assumptions, we have seen that an electron may tunnel from the leads only into the ground state of the DQD. If the level splitting Ω matches the energy of the photons ω_{r} in the MR, the electron in the ground state may absorb a photon and move to the excited state. It can then tunnel out of the excited state into the leads. This process leads to a photo-assisted current, or photocurrent. The DQD-MR system can thus be used as a detector of microwave photons. This detection mechanism is an analogue of the optical photodiodes, where an electron is excited across the semiconductor bandgap. In Fig. 5.3, we sketch and describe the microwave photodetection scheme. We see that the

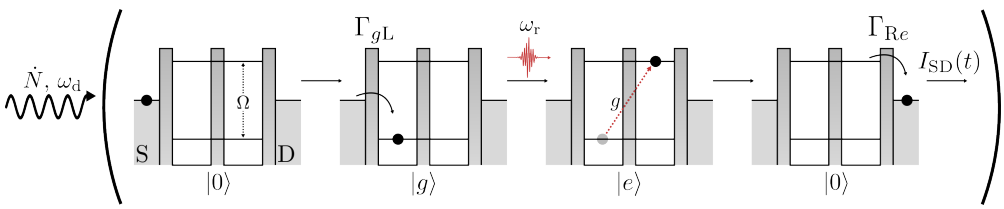

Figure 5.3: Scheme for the detection of microwave photons using a DQD-MR system. A coherent, monochromatic drive feeds in photons to the MR with rate $\dot{N}$ and frequency ω_{d}. The DQD starts in its empty state $|0\rangle$. An electron from the source (S) then tunnels into the ground state $|g\rangle$ with rate $\Gamma_{g\mathrm{L}}$. If the level splitting of the DQD Ω matches the frequency of the photons in the MR ω_{r}, the electron may absorb a photon and move to the excited state $|e\rangle$. The coupling between the DQD and the MR is given by g. The electron in $|e\rangle$ can then tunnel out into the drain (D) with rate $\Gamma_{\mathrm{R}e}$, bringing the DQD back to $|0\rangle$. This process produces a source-drain photocurrent $I_{\mathrm{SD}}(t)$ through the DQD.

photocurrent $I_{\mathrm{SD}}(t)$ is a key quantity in the detection of microwave photons, as it informs whenever a photon has been absorbed by the DQD. Note that we can also have the reverse process, where an electron is brought from drain to source through the absorption of a photon. We will, at least for now, only focus on the source-drain current.
We define the photocurrent as

$$I_{\mathrm{SD}}(t)/e = \Gamma_{\mathrm{R}e}p_e(t) - \Gamma_{e\mathrm{R}}p_0(t), \tag{5.59}$$

where $p_e(t) = \langle e|\hat{\rho}_{\rm S}(t)|e\rangle$ ($p_0(t) = \langle 0|\hat{\rho}_{\rm S}(t)|0\rangle$) is the occupation probability of the excited (empty) state and e denotes the electron charge.

Ideal photodetection

A photodetector is ideal when every photon impinging on the resonator excites an electron across the DQD, leading to a unit quantum efficiency, which, for a monochromatic drive, is defined as

$$\eta = \frac{I_{\rm SD}/e}{\dot{N}}, \tag{5.60}$$

where $I_{\rm SD}$ is the average, or steady-state, photocurrent through the DQD. In Ref. [20], several conditions were derived in order to reach unit efficiency. We summarize them here for completeness.
First, the resonator bandwidth is dominated by the input-port coupling, i.e., $\kappa = \kappa_{\rm in}$. Second, the drive, resonator, and DQD are in resonance, such that $\Delta_{\rm d} = \Delta_{\rm r} = 0$. Third, the decoherence rates are negligible, i.e. $\Gamma_{\rm L,R} \gg \gamma_-, \gamma_\phi$. Fourth, the tunnel coupling between the QDs is small compared to the level splitting, i.e. $t_c \ll \Omega$. Fifth, the rate at which photons get absorbed by the DQD, which is given by $4g^2/\tilde{\Gamma}$, where $\tilde{\Gamma} = \Gamma_{0e} + \gamma_- + 2\gamma_\phi$ denotes the total decoherence rate, should match the photonic loss rate κ. Lastly, the photocurrent is in the linear response regime, i.e. $I_{\rm SD}/e \propto \dot{N}$.

5.3 Equations of motion

We see from Eq. (5.59) that we need to obtain the probabilities $p_e(t)$ and $p_0(t)$ in order to compute the photocurrent. We do this using the master equation (5.58) and the relation in

Eq. (5.10). This leads to the following set of equations for the probabilities

$$\partial_t p_0(t) = -\Gamma_{g0} p_0(t) + \Gamma_{0e} p_e(t), \tag{5.61}$$

$$\partial_t p_e(t) = -(\Gamma_{0e} + \gamma_-) p_e(t) + 2g\mathrm{Im}\left\langle \hat{a}\hat{\sigma}_+ \right\rangle(t), \tag{5.62}$$

$$\begin{aligned}\partial_t \mathrm{Im}\left\langle \hat{a}\hat{\sigma}_+ \right\rangle(t) = &-\frac{1}{2}(\tilde{\Gamma} + \kappa)\mathrm{Im}\left\langle \hat{a}\hat{\sigma}_+ \right\rangle(t) - g p_e(t) \\ &-\frac{f}{2}(\left\langle \hat{\sigma}_+ \right\rangle(t) + \left\langle \hat{\sigma}_- \right\rangle(t)) - g\langle \hat{a}^\dagger \hat{a}\hat{\sigma}_z \rangle(t),\end{aligned} \tag{5.63}$$

$$\partial_t \left\langle \hat{\sigma}_- \right\rangle(t) = -\left(\frac{\tilde{\Gamma}}{2} + i\Delta_\mathrm{d}\right)\left\langle \hat{\sigma}_- \right\rangle(t) + ig\left\langle \hat{a}\hat{\sigma}_z \right\rangle(t), \tag{5.64}$$

$$\partial_t \left\langle \hat{a} \right\rangle(t) = -\left(\frac{\kappa}{2} + i\Delta_\mathrm{r}\right)\left\langle \hat{a} \right\rangle(t) - if - ig\left\langle \hat{\sigma}_- \right\rangle(t), \tag{5.65}$$

$$\partial_t \langle \hat{a}^\dagger \hat{a} \rangle(t) = -\kappa\langle \hat{a}^\dagger \hat{a} \rangle(t) - 2g\mathrm{Im}\left\langle \hat{a}\hat{\sigma}_+ \right\rangle(t) + if(\left\langle \hat{a} \right\rangle(t) - \langle \hat{a}^\dagger \rangle(t)), \tag{5.66}$$

where we have defined $f = \sqrt{\kappa_\mathrm{in}\dot{N}}$. This set of equations is not closed due to the terms $\langle \hat{a}^\dagger \hat{a}\hat{\sigma}_z \rangle(t)$ and $\left\langle \hat{a}\hat{\sigma}_z \right\rangle(t)$. We thus need to make further approximations in order to obtain an analytical solution for the photocurrent. Throughout the main part of the thesis, we employ three different approximations: the low-drive, the large-drive, and the mean-field approximation.

In the low-drive limit, we expand Eqs. (5.61)-(5.66) to lowest order in the drive and obtain the following, closed set of equations

$$\partial_t p_0(t) = -\Gamma_{g0} p_0(t) + \Gamma_{0e} p_e(t), \tag{5.67}$$

$$\partial_t p_e(t) = -(\Gamma_{0e} + \gamma_-) p_e(t) + 2g\mathrm{Im}\left\langle \hat{a}\hat{\sigma}_+ \right\rangle(t), \tag{5.68}$$

$$\begin{aligned}\partial_t \mathrm{Im}\left\langle \hat{a}\hat{\sigma}_+ \right\rangle(t) = &-\frac{1}{2}(\tilde{\Gamma} + \kappa)\mathrm{Im}\left\langle \hat{a}\hat{\sigma}_+ \right\rangle(t) - g p_e(t) \\ &-\frac{f}{2}(\left\langle \hat{\sigma}_+ \right\rangle(t) + \left\langle \hat{\sigma}_- \right\rangle(t)) + g\langle \hat{a}^\dagger \hat{a} \rangle(t),\end{aligned} \tag{5.69}$$

$$\partial_t \left\langle \hat{\sigma}_- \right\rangle(t) = -\left(\frac{\tilde{\Gamma}}{2} + i\Delta_\mathrm{d}\right)\left\langle \hat{\sigma}_- \right\rangle(t) - ig\left\langle \hat{a} \right\rangle(t), \tag{5.70}$$

$$\partial_t \left\langle \hat{a} \right\rangle(t) = -\left(\frac{\kappa}{2} + i\Delta_\mathrm{r}\right)\left\langle \hat{a} \right\rangle(t) - if - ig\left\langle \hat{\sigma}_- \right\rangle(t), \tag{5.71}$$

$$\partial_t \langle \hat{a}^\dagger \hat{a} \rangle(t) = -\kappa\langle \hat{a}^\dagger \hat{a} \rangle(t) - 2g\mathrm{Im}\left\langle \hat{a}\hat{\sigma}_+ \right\rangle(t) + if(\left\langle \hat{a} \right\rangle(t) - \langle \hat{a}^\dagger \rangle(t)). \tag{5.72}$$

In the large-drive limit, where many photons are present in the resonator, the back-action of the DQD on the resonator state can be neglected and the photonic operators $\hat{a}$ and $\hat{a}^\dagger$ can be taken to be equal to their average values. Applying these conditions to Eq. (5.65) we find, in the steady state

$$0 = -\left(\frac{\kappa}{2} + i\Delta_\mathrm{r}\right)\hat{a} - if \quad \Rightarrow \quad \hat{a} = -\frac{2if}{\kappa + 2i\Delta_\mathrm{r}}. \tag{5.73}$$

Plugging Eq. (5.73) into Eqs. (5.61)-(5.66), we find

$$\partial_t p_0(t) = -\Gamma_{g0} p_0(t) + \Gamma_{0e} p_e(t), \tag{5.74}$$
$$\partial_t p_e(t) = -(\Gamma_{0e} + \gamma_-) p_e(t) - ig\hat{a}\left\langle \hat{\sigma}_+ + \hat{\sigma}_- \right\rangle(t), \tag{5.75}$$
$$\partial_t \left\langle \hat{\sigma}_- \right\rangle(t) = -\left(\frac{\tilde{\Gamma}}{2} + i\Delta_\mathrm{d}\right)\left\langle \hat{\sigma}_- \right\rangle(t) + ig\hat{a}(p_e(t) - p_g(t)), \tag{5.76}$$
$$\partial_t p_g(t) = \Gamma_{g0} p_0(t) + \gamma_- p_e(t) + ig\hat{a}\left\langle \hat{\sigma}_+ + \hat{\sigma}_- \right\rangle(t). \tag{5.77}$$

The set of equations in the low- and large-drive limit can be solved in the steady state. For the analytical solutions, we refer the reader to Papers I and III.
Beyond the low- and large-drive limit, we employ a mean-field approximation [85, 86]. It relies on the assumption that, at all times, correlations between the DQD and the resonator can be neglected, such that we can approximate the system's density matrix as $\hat{\rho}_\mathrm{S}(t) = \hat{\rho}_\mathrm{DQD}(t) \otimes \hat{\rho}_\mathrm{r}(t)$. This means that we can factorize the expectation value of products between DQD and resonator operators, e.g. $\langle \hat{a}\hat{\sigma}_+ \rangle = \langle \hat{a} \rangle \langle \hat{\sigma}_+ \rangle$. Plugging this into Eqs. (5.61)-(5.66) we get the closed, but non-linear, set of equations

$$\partial_t p_0(t) = -\Gamma_{g0} p_0(t) + \Gamma_{0e} p_e(t), \tag{5.78}$$
$$\partial_t p_e(t) = -(\Gamma_{0e} + \gamma_-) p_e(t) - ig(\langle \hat{a} \rangle(t) \left\langle \hat{\sigma}_+ \right\rangle(t) - \langle \hat{a}^\dagger \rangle(t) \left\langle \hat{\sigma}_- \right\rangle(t)), \tag{5.79}$$
$$\partial_t \left\langle \hat{\sigma}_- \right\rangle(t) = -\left(\frac{\tilde{\Gamma}}{2} + i\Delta_\mathrm{d}\right)\left\langle \hat{\sigma}_- \right\rangle(t) + ig \langle \hat{a} \rangle(t)(p_e(t) - p_g(t)), \tag{5.80}$$
$$\partial_t \langle \hat{a} \rangle(t) = -\left(\frac{\kappa}{2} + i\Delta_\mathrm{r}\right)\langle \hat{a} \rangle(t) - if - ig \left\langle \hat{\sigma}_- \right\rangle(t), \tag{5.81}$$
$$\partial_t p_g(t) = \Gamma_{g0} p_0(t) + \gamma_- p_e(t) + ig(\langle \hat{a} \rangle(t) \left\langle \hat{\sigma}_+ \right\rangle(t) - \langle \hat{a}^\dagger \rangle(t) \left\langle \hat{\sigma}_- \right\rangle(t)). \tag{5.82}$$

This set of equations can also be solved in the steady-state regime, see Paper I.
In Fig. 5.4, we plot the steady-state photocurrent I_SD/e as a function of the drive amplitude f within the approximations introduced above.

We can see that the mean-field solution matches the low- and large-drive results for the respective drive strengths.

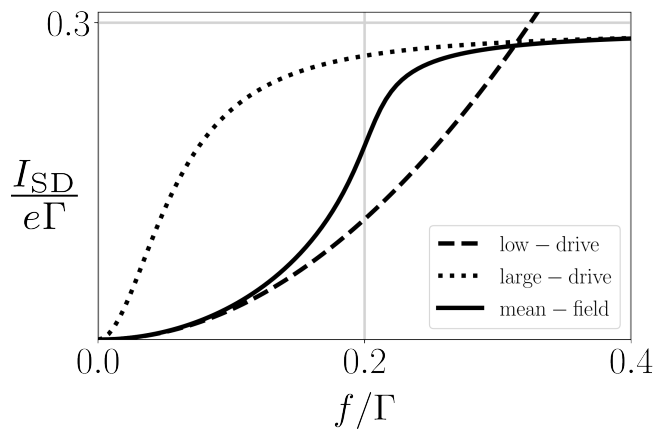

Figure 5.4: Steady-state photocurrent $I_{\mathrm{SD}}/(e\Gamma)$ as a function of the drive f/Γ in the low-drive (dashed line), larg-drive (dotted line), and meand-field (full line) regime, where we have set $\Gamma = \Gamma_{\mathrm{L}} = \Gamma_{\mathrm{R}}$. The parameters chosen are $\theta = 0.5$, $g/\Gamma = 0.8$, $\gamma_-/\Gamma = 0.8$, $\gamma_\phi/\Gamma = 1$, and $\kappa/\Gamma = 0.1$.

Chapter 6

Full Counting Statistics

The quantum-statistical nature of photon-absorption and electron-tunneling events in the DQD-MR system introduces fluctuations to the photocurrent. These fluctuations cannot be obtained through an analysis of the average photocurrent alone. They are, however, key to understanding important properties of the particle transport. For example, the noise of the current can give us insight if the separate electron-tunneling events are correlated with each other or if they follow a completely random distribution [87].
One powerful tool for the computation of the fluctuations is the so-called full counting statistics (FCS) [88–91]. In Fig. 6.1, we sketch a typical scenario to obtain the FCS. If we are able to count every single electron passing to the drain separately, we can plot a histogram of the number of electrons n counted in a time span t. From this histogram we can infer the probability distribution $p(n,t)$. Computing the moments of this distribution constitutes full knowledge about the statistics of the photocurrent.

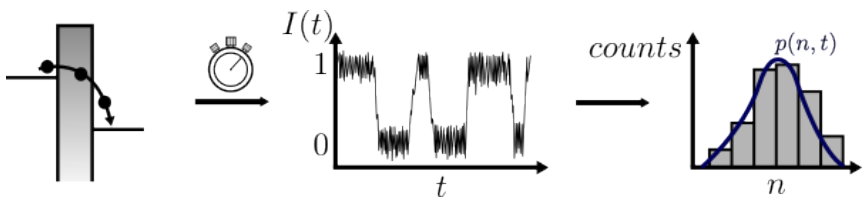

Figure 6.1: Typical FCS scenario. Counting individual particle-tunneling events gives a time trace that indicates whenever there is a particle on the system (denoted by 1 in the sketch) and when there is not (denoted by 0). Obtaining several such time traces, one can plot a histogram with the number of particles n that have been registered over a certain time span t. On this histogram one can fit the probability distribution $p(n,t)$, which gives full knowledge about the statistics of the particle current.

Experimentally, obtaining the FCS is a formidable task, specifically for electronic transport. The electron jumps typically occur on a very fast time scale, such that it is hard to resolve them accurately. A detector that is sensitive to charge fluctuations is needed, which usually

comes in the form of a quantum point contact or a SET [92].

In this chapter, we derive the FCS for the photocurrent through the DQD-MR system. In Sec. 6.1, we show how the FCS is generally obtained from a quantum master equation. We then show how the zero-frequency FCS and the finite-frequency noise is calculated. In Sec. 6.2, we apply the knowledge gained from the previous section to our specific system.

6.1 FCS for quantum master equations

Various methods are employed to obtain the FCS in quantum transport scenarios. The most widely used approaches are based on scattering theory [93], Keldysh Green's functions [94], and master equation techniques [95]. Given that we use a master equation to describe the system's dynamics, we will also apply this framework to calculate the FCS.

6.1.1 Number-resolved master equation

The relevant quantity within the FCS framework is the probability distribution $p(n,t)$ of the transfer of n particles in a time span t. It would therefore be useful to resolve the master equation with respect to n and write the density matrix as

$$\hat{\rho}_{\mathrm{S}}(t) = \sum_n \hat{\rho}_{\mathrm{S}}(n,t). \tag{6.1}$$

To that end, we solve the master equation (5.31) in Laplace space by introducing

$$\hat{\rho}_{\mathrm{S}}(z) = \int_0^\infty dt\, \hat{\rho}_{\mathrm{S}}(t) e^{-zt}. \tag{6.2}$$

Plugging this into the master equation, we find

$$z\hat{\rho}_{\mathrm{S}}(z) - \hat{\rho}_{\mathrm{S}}(0) = \mathcal{L}\hat{\rho}_{\mathrm{S}}(z) \quad \Rightarrow \quad \hat{\rho}_{\mathrm{S}}(z) = (z-\mathcal{L})^{-1}\hat{\rho}_{\mathrm{S}}(0). \tag{6.3}$$

We define the propagator $\Omega(z) = (z-\mathcal{L})^{-1}$ and partition the Liouvillian as $\mathcal{L} = \mathcal{L}_0 + \mathcal{J}$, where $\mathcal{L}_0$ describes the free evolution of the system and $\mathcal{J}$ describes the tunneling events, or jumps, that we would like to monitor. We can then write the propagator as

$$\begin{aligned} \Omega(z) &= \sum_{n=0}^{\infty} (\Omega_0(z)\mathcal{J})^n \Omega_0(z), \\ &= \underbrace{\Omega_0(z)}_{\text{no jumps}} + \underbrace{\Omega_0(z)\mathcal{J}\Omega_0(z)}_{\text{1 jump}} + \underbrace{\Omega_0(z)\mathcal{J}\Omega_0(z)\mathcal{J}\Omega_0(z)}_{\text{2 jumps}} + \ldots \end{aligned} \tag{6.4}$$

where $\Omega_0(z) = (z - \mathcal{L}_0)^{-1}$. The corresponding n-resolved density matrix is then given by

$$\hat{\rho}_{\mathrm{S}}(n, z) = \Omega_0(z)(\mathcal{J}\Omega_0(z))^n \hat{\rho}_{\mathrm{S}}(0). \tag{6.5}$$

Using Eq. (6.5) and Eq. (6.3), we find the equations of motion for the n-resolved density matrix

$$\partial_t \hat{\rho}_{\mathrm{S}}(n, t) = \mathcal{L}_0 \hat{\rho}_{\mathrm{S}}(n, t) + \mathcal{J}\hat{\rho}_{\mathrm{S}}(n-1, t). \tag{6.6}$$

6.1.2 The counting field

We solve the equation of motion (6.6) by introducing the so-called counting field χ, which we define as the variable that is conjugate to n and define the discrete Fourier transform of the n-resolved density matrix as

$$\hat{\rho}_{\mathrm{S}}(\chi, t) = \sum_{n=0}^{\infty} \hat{\rho}_{\mathrm{S}}(n, t) e^{in\chi}. \tag{6.7}$$

We find the equation of motion for the χ-dependent density matrix after plugging Eq. (6.7) into Eq. (6.6)

$$\partial_t \hat{\rho}_{\mathrm{S}}(\chi, t) = (\mathcal{L}_0 + e^{i\chi}\mathcal{J})\hat{\rho}_{\mathrm{S}}(\chi, t) = \mathcal{L}(\chi)\hat{\rho}_{\mathrm{S}}(\chi, t). \tag{6.8}$$

The formal solution of Eq. (6.8) is given by

$$\hat{\rho}_{\mathrm{S}}(\chi, t) = e^{\mathcal{L}(\chi)t}\hat{\rho}_{\mathrm{S}}(0). \tag{6.9}$$

We define the moment-generating function (MGF) of the quantum jump distribution as

$$M(\chi, t) = \mathrm{Tr}\{e^{\mathcal{L}(\chi)t}\hat{\rho}_{\mathrm{S}}(0)\}. \tag{6.10}$$

We also define the cumulant-generating function (CGF) as $C(\chi, t) = \log(M(\chi, t))$. The different cumulants of the distribution are then found by differentiating the CGF with respect to the counting field

$$\langle\langle n^k \rangle\rangle = \frac{\partial_k}{\partial(i\chi)^k} C(\chi, t)|_{\chi=0}, \tag{6.11}$$

where $\langle\langle n^k \rangle\rangle$ gives the k-th cumulant of the distribution. The probability distribution $p(n, t)$ can the be found through the CGF by inverse Fourier transform

$$p(n, t) = \int_{-\pi}^{\pi} \frac{d\chi}{2\pi}\, e^{C(\chi,t) - in\chi}. \tag{6.12}$$

6.1.3 Zero-frequency FCS

We have previously seen that the steady-state regime is of great interest because of its analytical tractability. It is obtained by moving to the long-time, or zero-frequency, limit. To do so, we first introduce the eigendecomposition of the Liouvillian $\mathcal{L}(\chi)$

$$\mathcal{L}(\chi) = \sum_k \lambda_k(\chi) \, |\psi_k(\chi)\rangle\rangle\langle\langle\psi_k(\chi)| \, , \tag{6.13}$$

where $\lambda_k(\chi)$ are the eigenvectors and $|\psi_k(\chi)\rangle\rangle$ are the eigenvectors of the Liouvillian. Note that we have employed a special Dirac notation for the eigenvectors. Since the Liouvillian is a superoperator, its eigenvectors are operators, hence the special notation to differentiate them from state vectors. Note that also, in general, $|\psi_k(\chi)\rangle\rangle^\dagger \neq \langle\langle\psi_k(\chi)|$. The MGF can then be written as

$$M(\chi, t) = \sum_k e^{\lambda_k(\chi)t} \langle\langle\psi_0|\psi_k(\chi)\rangle\rangle\langle\langle\psi_k(\chi)|\psi_0\rangle\rangle, \tag{6.14}$$

where we have set $|\psi_0\rangle\rangle = \hat{\rho}_{\mathrm{S}}(0)$. In the long-time limit, only the eigenvalue with the largest real part will survive, as all other terms yield exponentially damped contributions to the cumulants. We can thus, to exponential accuracy, write the MGF and the CGF as

$$M(\chi, t) \sim e^{\lambda_0(\chi)t} \quad \Rightarrow \quad C(\chi, t) \sim \lambda_0(\chi)t, \tag{6.15}$$

where $\lambda_0(\chi) = \max_k\{\lambda_k(\chi)\}$. We see that all zero-frequency cumulants are linear in time.

6.1.4 Finite-frequency noise

The zero-frequency cumulants provide valuable insight into various statistical properties of particle transport. However, to fully capture the relevant correlations and associated time scales, it is necessary to analyze the system over the entire frequency spectrum [96]. To this end, we will focus on the finite-frequency noise (FFN), which can be determined using MacDonald's formula [97]

$$S(\omega) = \omega \int_0^\infty dt \, \sin(\omega t) \frac{d}{dt} \langle\langle n^2 \rangle\rangle(t). \tag{6.16}$$

It is useful to rewrite the MacDonald's formula in Laplace space as [98]

$$\begin{aligned} S(\omega) &= \frac{\omega}{2i} \int_0^\infty dt \, (e^{i\omega t} - e^{-i\omega t}) \frac{d}{dt} \langle\langle n^2 \rangle\rangle(t) \\ &= \frac{\omega}{2i} [-i\omega \langle\langle n^2 \rangle\rangle(z = -i\omega) - \langle\langle n^2 \rangle\rangle(0) - i\omega \langle\langle n^2 \rangle\rangle(z = i\omega)) + \langle\langle n^2 \rangle\rangle(0)] \\ &= -\omega^2 \, \mathrm{Re}\{\langle\langle n^2 \rangle\rangle(z = -i\omega)\}. \end{aligned} \tag{6.17}$$

To find $\langle\langle n^2\rangle\rangle(z)$, we solve the master equation (6.8) in Laplace space. Using the transformation in Eq. (6.2), we get

$$\hat{\rho}_{\mathrm{S}}(\chi, z) = \Omega(\chi, z)\hat{\rho}_{\mathrm{S}}(\chi, 0), \tag{6.18}$$

where the χ-dependent propagator is defined as $\Omega(\chi, z) = \sum_{n=0}^{\infty}(\Omega_0(z)(e^{i\chi}-1)\mathcal{J})^n\Omega_0(z)$. The second cumulant is found by expanding Eq. (6.18) to second order in χ

$$\begin{aligned}\langle\langle n^2\rangle\rangle(z) &= \partial_{i\chi}^2 \mathrm{Tr}\{\hat{\rho}_{\mathrm{S}}(\chi, z)\}|_{\chi\to 0} \\ &= \mathrm{Tr}\{(\Omega_0(z)\mathcal{J}\Omega_0(z) + 2\Omega_0(z)\mathcal{J}\Omega_0(z)\mathcal{J}\Omega_0(z)\}.\end{aligned} \tag{6.19}$$

6.2 FCS of the photocurrent

In Sec. 5.3 we have derived the equations of motion for the DQD-MR system that describe the dynamics in the low-drive, large-drive, and mean-field regime and showed how they can be used to derive the average, or steady-state, photocurrent, which corresponds to the first cumulant of the distribution. The goal now is to go beyond the average photocurrent and derive the FCS. To that end, we will also use the equations of motion.
In the long-time limit, we can write the χ-dependent density matrix in Eq. (6.8) using the eigendecomposition in Eq. (6.13) as

$$\lim_{t\to\infty} \hat{\rho}_{\mathrm{S}}(\chi, t) = e^{\lambda_0(\chi)t}\,|\psi_0(\chi)\rangle\rangle\langle\langle\psi_0(\chi)|\,\hat{\rho}_{\mathrm{S}}(\chi, 0). \tag{6.20}$$

The expectation value of any operator $\hat{A}$ with respect to the density matrix in Eq. (6.20) can then be written as

$$\langle\hat{A}\rangle = \mathrm{Tr}\{\hat{A}e^{\lambda_0(\chi)t}\mu_0(\chi)\} \Leftrightarrow e^{-\lambda_0(\chi)t}\langle\hat{A}\rangle = \mathrm{Tr}\{\hat{A}\mu_0(\chi)\}, \tag{6.21}$$

where we have abbreviated $\mu_0(\chi) = |\psi_0(\chi)\rangle\rangle\langle\langle\psi_0(\chi)|\,\hat{\rho}_{\mathrm{S}}(\chi, 0)$. We see that the term $e^{-\lambda_0(\chi)t}\langle\hat{A}\rangle$ is time independent. Taking its time derivative therefore yields

$$\partial_t\langle\hat{A}\rangle = \lambda_0(\chi)\langle\hat{A}\rangle. \tag{6.22}$$

We can make use of this equality to compute the eigenvalue $\lambda_0(\chi)$, and thus the CGF, of the photocurrent distribution. We compute the expectation values of our system operators using the $\chi-$dependent master equation, which is given by

$$\begin{aligned}\partial_t\hat{\rho}_{\mathrm{S}} =& -[\hat{\mathcal{H}}, \hat{\rho}_{\mathrm{S}}] + \Gamma_{g\mathrm{L}}\mathcal{D}[\hat{s}_g^\dagger]\hat{\rho}_{\mathrm{S}} + \Gamma_{\mathrm{L}e}\mathcal{D}[\hat{s}_e]\hat{\rho}_{\mathrm{S}} \\ &+ \Gamma_{g\mathrm{R}}(e^{-i\chi}\hat{s}_g^\dagger\hat{\rho}_{\mathrm{S}}\hat{s}_g - \tfrac{1}{2}\{\hat{s}_g\hat{s}_g^\dagger, \hat{\rho}_{\mathrm{S}}\}) + \Gamma_{\mathrm{R}e}(e^{i\chi}\hat{s}_e\hat{\rho}_{\mathrm{S}}\hat{s}_e^\dagger - \tfrac{1}{2}\{\hat{s}_e^\dagger\hat{s}_e, \hat{\rho}_{\mathrm{S}}\}) \\ &+ \frac{\gamma_\phi}{2}\mathcal{D}[\hat{\sigma}_z]\hat{\rho}_{\mathrm{S}} + \gamma_-\mathcal{D}[\hat{\sigma}_-]\hat{\rho}_{\mathrm{S}} + \kappa\mathcal{D}[\hat{a}]\hat{\rho}_{\mathrm{S}} = \mathcal{L}(\chi)\hat{\rho}_{\mathrm{S}}.\end{aligned} \tag{6.23}$$

Note that we have omitted the χ and t dependence of the density matrix for ease of notation. The χ-dependent Liouvillian is given by $\mathcal{L}(\chi) = \mathcal{L}_0 + e^{i\chi}\mathcal{J}_+ + e^{-i\chi}\mathcal{J}_-$. We see that we have two jump operators with different signs in the counting field. This is due to electrons not only being able to flow from the DQD to the drain but also back. The master equation (6.23) can be used together with Eq. (6.22) to derive the χ-dependent equations of motion similar to the ones in Sec. 5.3. The analytical expressions can be found in Paper I.

Within the low-drive limit, we find that the CGF describes a bi-directional Poisson process, one for electrons flowing to the drain and the other for the reverse process. Assuming the ideal-photodetector regime introduced in Sec. 5.2, the electron flow becomes Poissonian and the corresponding probability distribution is given by

$$p(n,t) = e^{-\dot{N}t}\frac{(\dot{N}t)^n}{n!}. \tag{6.24}$$

The statistics of the electrons arriving to the drain in the regime of ideal photodetection is thus equivalent to the statistics of photons from a coherent light source [67]. The ideal photodetector does therefore not only detect each single photon but also preserves their long-time statistics.

In the large-drive limit, only the electron in- and out-tunneling rates $\Gamma_{\mathrm{L,R}}$ impact the photocurrent statistics. The resonator primarily acts as a mediator for transitions between the ground and excited states of the DQD, with these transitions occurring so rapidly that their associated rates no longer appear in the FCS.

The mean-field approach gives an analytical result for the zero-frequency cumulants which again interpolates nicely between the low- and large-drive results. This can be seen in Fig. 6.2(a), where we present a plot for the first two cumulants. In addition, we look at the non-Gaussian properties of the probability distribution by plotting the third cumulant, see Fig. 6.2(b). The third cumulant is nonzero and increases monotonically with the microwave drive, indicating that the distribution exhibits non-Gaussian behavior. In the inset, we plot the logarithm of the probability distribution using the saddle-point approximation for both the low- and high-drive limits, comparing these to the logarithm of a Gaussian distribution. For the selected parameters, we observe that the probability distributions in both the low- and high-drive regimes are skewed, showing a clear deviation from Gaussian behavior.

For the FFN, we see from Eq. (6.19) that we need to obtain the propagator $\Omega_0(z)$ and the jump operator $\mathcal{J}$. Also here, we refer the reader tho Paper I for the analytical expression of the FFN in the different regimes.

In the low-drive regime, we reduce the Hilbert space of the resonator by assuming that we have at most 2 photons at a time present in the resonator. The basis in this case is spanned by the dressed states of the hybridized DQD-MR system. We find that the frequency dependence is determined by the rate Γ_{g0}, which can be explained as follows: in the low-drive limit, the system mostly remains in its ground state, and the likelihood of an electron being

excited is low. When such an excitation does occur, another electron will tunnel back into the ground state with rate Γ_{g0}. Consequently, tunneling events occur in correlated pairs and the events within each pair are separated by a time scale $1/\Gamma_{g0}$. This time scale acts as the effective "dead-time" of the photodetector. Pairs of tunneling events are uncorrelated from each other, as they are separated by a much longer timescale $1/f^2$.
In the ideal-photodetection limit, the FFN simplifies to $S(\omega) = \dot{N}$, corresponding to the noise profile of photons emitted by a coherent light source.
In the large-drive regime, the resonator decouples from the DQD and the Liouvillian is a 5×5 matrix in the basis of the DQD $\hat{\rho}_{\mathrm{DQD}} = (\rho_0, \rho_g, \rho_e, \rho_{ge}, \rho_{eg})^T$, where $\rho_i = \langle i|\hat{\rho}_{\mathrm{S}}|i\rangle$ and $\rho_{ij} = \langle i|\hat{\rho}_{\mathrm{S}}|j\rangle$. The frequency dependence in this regime is by both the in- and out-tunneling rate from the DQD and is given by $1/(\Gamma_{0e} + 2\Gamma_{g0})$. In direct analogy to the low-drive case we interpret this timescale as the dead-time of the photodetector.
In the mean-field regime, similarly to the large-drive regime, the resonator decouples from the DQD and we get a 5×5 matrix for the Liouvillian. It allows for an analytical computation of the FFN across the entire frequency regime. In Fig. 6.2(c), we plot the FFN in the different regimes.

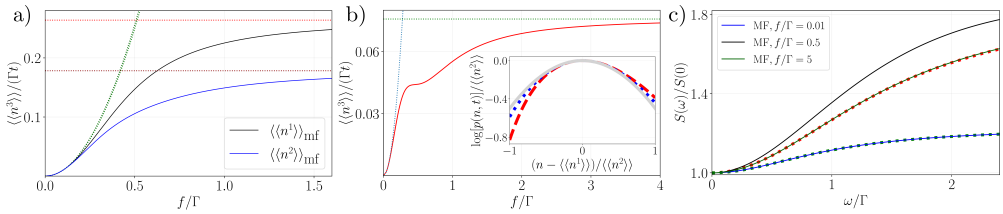

Figure 6.2: Figure taken from Paper I. a) The first two zero-frequency cumulants within the mean-field approximation (full lines) normalized with Γt and plotted as a function of the normalized drive amplitude f/Γ, where $\Gamma = \Gamma_{\mathrm{L}} = \Gamma_{\mathrm{R}}$. The cumulants are compared to the analytical results in the low- and large-drive limits (dotted lines). b) The third cumulant within the mean-field approximation (full line) normalized with Γt and plotted as a function of f/Γ. The third cumulant is also compared to the low- and large-drive limits (dotted lines). Inset: Probability distribution in the saddle-point approximation for the low-drive (red-dashed line) and the large-drive limit (blue dotted line) as a function of $(n - \langle\langle n^1\rangle\rangle)/\langle\langle n^2\rangle\rangle$. A Gaussian is shown for comparison (gray full line). The distributions are normalized by their second cumulant $\langle\langle n^2\rangle\rangle$. c) The FFN within the mean-field approximation (full lines) normalized with its value at zero frequency $S(0)$ and plotted as a function of the normalized frequency ω/Γ for different values of f/Γ. The FFN is compared to the analytical results in low- and large-drive limit (dotted lines). The chosen system parameters are $g/\Gamma = 0.457$, $\kappa_{\mathrm{in}}/\Gamma = 0.094$, $\kappa/\Gamma = 0.337$, $\epsilon/\Gamma = -17.57$, $t_c/\Gamma = 6.78$, $\gamma_-/\Gamma = 0.5$, $\gamma_\phi/\Gamma = 3.92$, and $\Delta_{\mathrm{d}} = \Delta_{\mathrm{r}} = 0$.

Chapter 7

Wigner-Function Formalism

The Wigner function is a quasiprobability distribution which was introduced by Eugene Wigner to describe the state of a quantum system in phase space [99]. The phase space spans all possible states the system can be in as a function of typically two conjugate variables, such as position and momentum or time and frequency [100]. Taking position and momentum as an example, the state of a classical system can usually be represented by a point in phase space, and the probability to find the system at this point is described by a classical probability distribution. The position and momentum for a quantum state cannot be determined simultaneously due to Heisenberg's uncertainty principle, and thus, the phase space representation typically shows a circle or ellipse and the Wigner function is used as the analogue to the probability distribution. One important feature of the Wigner function is that it can take on negative values, hence the name quasiprobability, and it can therefore indicate quantum-mechanical interference [101].

The Wigner function finds applications in different research areas. In quantum optics, it is used to represent different states of light, such as coherent states, Fock states or squeezed states [102, 103]. In quantum information and computing, it is useful for phase-space based approaches to quantum error correction [104]. It is also used in the electronic analogue to quantum optics, called electron quantum optics, where one uses the tools from quantum optics to describe single-electron excitations interacting with each other in electronic interferometer setups [105]. A further area where Wigner functions are employed is signal processing and more specifically the time-frequency analysis of signals [106–108]. It is from this field that we will borrow a few notions and tools for the time and frequency analysis of photodetection in the DQD-MR hybrid.

In experiments, the photons we would like to detect often arrive as a wave packet. This wave packet in our case is a microwave pulse which has a finite spread in both time and frequency. We are therefore interested to analyze the detection of single microwave pulses. Connecting to signal processing, the photodetection in the case of a single pulse drive can

be seen as a filter converting the incoming signal (the pulse) to an outgoing one (the photocurrent). The conversion of microwave pulses to electrons is also interesting since the exact number of photons in a pulse is not well defined, and this conversion could help gaining knowledge about said number.

In this chapter, we derive a Wigner-function formalism for the detection of single microwave pulses. In Sec. 7.1, we introduce the Wigner function and show how it is used in signal processing and electron quantum optics. In Sec. 7.2, we employ several notions from the previous section to describe the detection of single microwave pulses using a DQD-MR system.

7.1 The Wigner function

7.1.1 Wigner function in quantum mechanics

The position and momentum representations of a quantum system are usually encountered first in the study of quantum mechanics [109]. The wave function formalism enables the analysis of the probability density in either representation individually, but not simultaneously. A mathematical object capable of providing joint information in both representations is thus desirable. The Wigner function closes this gap. The Wigner function was first introduced to study the influence of quantum mechanics to problems in classical statistical mechanics, where the Boltzmann factors include energies which themselves are functions of both position and momentum [99].
The Wigner function for a pure state $\psi(x)$ is defined as [104]

$$W(x,p) = \frac{1}{2\pi}\int dy\, e^{-ipy}\psi\left(x+\frac{y}{2}\right)\psi^*\left(x-\frac{y}{2}\right). \tag{7.1}$$

The position and momentum probability distributions are given by the marginals of the Wigner function

$$\begin{aligned}\langle x|\hat{\rho}|x\rangle &= \int dp\, W(x,p),\\ \langle p|\hat{\rho}|p\rangle &= \int dx\, W(x,p),\end{aligned} \tag{7.2}$$

where $\hat{\rho}$ is the density matrix of the quantum system.

7.1.2 Wigner-Ville distribution for time-frequency analysis

Two other important conjugate variables one encounters in quantum mechanics are time and frequency. The time- and frequency-dependent Wigner function is often referred to

as Wigner-Ville distribution and it finds applications in the time-frequency analysis in the processing of signals [110].
Given a time-dependent signal $s(t)$, the Wigner-Ville distribution is defined as

$$W(t,\omega) = \frac{1}{2\pi}\int d\tau\, e^{-i\omega\tau} s\left(t+\frac{\tau}{2}\right) s^*\left(t-\frac{\tau}{2}\right). \tag{7.3}$$

We can look at two examples of a signal that is monochromatic and one that is localized in time, respectively. For a monochromatic signal $s(t) = e^{i\omega_1 t}$ we find

$$W_{\mathrm{mc}}(t,\omega) = \frac{1}{2\pi}\int d\tau\, e^{-i(\omega-\omega_1)\tau} = \delta(\omega-\omega_1). \tag{7.4}$$

For a signal localized at time t_0, i.e. $s(t) = \delta(t-t_0)$, we find

$$W_\delta(t,\omega) = \frac{1}{2\pi}\int d\tau\, e^{-i\omega\tau}\delta\left(t-t_0+\frac{\tau}{2}\right)\delta^*\left(t-t_0-\frac{\tau}{2}\right) = \delta(t-t_0). \tag{7.5}$$

7.1.3 The Volterra series

In signal processing, one is typically interested to study properties of an incoming signal that are not directly observable. To that end, the signal is usually put through a filter and produces an outgoing signal, which can be more easily analyzed as the filtering typically removes noise from the input [111]. One example is a low-pass filter, which removes unwanted high-frequency components of an incoming signal.
This filtering process can in general be described by the following

$$y(t) = Tx(t), \tag{7.6}$$

where $x(t)$ is the input signal, $y(t)$ is the output and T is an operator that maps between the two functions. If T is a linear operator, the response in Eq. (7.6) can be described by a convolution of $x(t)$ with a linear kernel denoted by $h^{(1)}$

$$y(t) = \int d\tau\, h^{(1)}(\tau)x(t-\tau). \tag{7.7}$$

The Volterra series [112, 113] extends this linear system response to nonlinear systems

$$\begin{aligned} y(t) =& h^{(0)} + \int d\tau_1\, h^{(1)}(\tau_1)x(t-\tau_1) + \\ & \int d\tau_1 d\tau_2\, h^{(2)}(\tau_1,\tau_2)x(t-\tau_1)x(t-\tau_2) + \ldots \end{aligned} \tag{7.8}$$

The integral kernels $h^{(n)}$ as referred to as the Volterra kernels and they must fulfill causality

$$h^{(n)}(\tau_1,\ldots,\tau_n) = 0, \quad \text{for } \tau_j < 0, \quad j = 1,2,\ldots,n. \tag{7.9}$$

The Volterra series can be seen as a Taylor series with memory effects. The Taylor series only describes systems where the output is mapped to the input instantaneously, whereas the Volterra series describes systems for which the output also depends on past inputs.

In the next section we will see how we can combine the Volterra series and the Wigner-Ville distribution to study the time and frequency dependence of a detector of microwave pulses.

7.1.4 Wigner function in electron quantum optics

The field of electron quantum optics can be seen as the electronic analogue to quantum optics [114]. It borrows concepts such as Mach-Zehnder interferometry and tries to translate them to electrons. The single photons in quantum optics are replaced by single-electron excitations, such as Levitons [115], and the optical mirrors where the photons interact are replaced by quantum point contacts. One can also employ first- and second-order correlation functions to study the coherence properties of the single electron excitations, similarly to the $g^{(1)}$ and $g^{(2)}$ functions in quantum optics.
The first-order electron coherence function is given by [105]

$$\mathcal{G}(x,t;y,t') = \mathrm{Tr}\{\psi(x,t)\hat{\rho}\psi^{\dagger}(y,t')\}, \tag{7.10}$$

where $\hat{\rho}$ is the density matrix of the electrons and $\psi(x,t)$ is an annihilation operator. The coherence function in Eq. (7.10) gives information about coherence and dephasing times. A frequency representation is obtained through a Fourier transform, and it gives information about the nature of the single-electron excitation. Also here, a joint time and frequency representation is very useful. It is again obtained by employing the Wigner function, which in this case is defined as [105]

$$W(t,\omega) = \frac{1}{2\pi}\int d\tau\, v_{\mathrm{F}} e^{i\omega\tau}\mathcal{G}\left(t+\frac{\tau}{2}, t-\frac{\tau}{2}\right), \tag{7.11}$$

where v_{F} denotes the Fermi velocity of the electron excitations.

We are not going to employ this formalism to our problem. However, it might be useful to develop a Wigner-function formalism for the electrons tunneling out of the DQD, something which would be of interest for future investigations.

7.2 Wigner-function formalism of photodetection

Driving the DQD-MR system with a single microwave pulse changes the drive Hamiltonian in Eq. (5.35) to (see App. A for details)

$$\hat{H}_{\mathrm{DR}} = \sqrt{\kappa_{\mathrm{in}}}(f^{*}(t)\hat{a} + f(t)\hat{a}^{\dagger}), \tag{7.12}$$

where $f(t)$ is the time-dependent amplitude and we are working again in the frame rotating at the center frequency of the pulse ω_1.

7.2.1 Photodetector as non-linear filter

Using the drive Hamiltonian in Eq. (7.12), we derive again a set of equations of motion in the low-drive regime, similar to the one introduced in Sec. 5.3. The reader can find the set of equations in Paper II. The time dependence of the drive Hamiltonian complicates the calculations of the different operator expectation values. By moving to Fourier space, we transform the differential equations to a set of algebraic ones. The frequency-dependent photocurrent is then found to be of the following form

$$\begin{aligned}\tilde{I}(\omega)/e &= \Gamma_{\mathrm{R}e}\tilde{p}_e(\omega) + \Gamma_{g\mathrm{R}}\tilde{p}_0(\omega) \\ &= \frac{1}{\sqrt{2\pi}}\int \frac{d\omega'}{2\pi}\tilde{h}(\omega-\omega',\omega')\tilde{f}(\omega-\omega')\tilde{f}^*(\omega'),\end{aligned} \tag{7.13}$$

where $\tilde{h}(\omega,\omega')$ is a function which depends on the detector properties and $\tilde{f}(\omega)$ is the Fourier transform of $f(t)$. Taking the Fourier transform of Eq. (7.13) and replacing $\omega \to \omega+\omega'$, we get

$$\begin{aligned}I(t)/e &= \frac{1}{(2\pi)^2}\int d\omega d\omega'\, e^{-i(\omega+\omega')t}\tilde{h}(\omega,\omega')\tilde{f}(\omega)\tilde{f}^*(\omega') \\ &= \frac{1}{2\pi}\int_0^\infty d\tau d\tau' h(\tau,\tau')f(t-\tau)f^*(t-\tau'),\end{aligned} \tag{7.14}$$

where $h(\tau,\tau')$ is the Fourier transform of $\tilde{h}(\omega,\omega')$. We note that $h(\tau,\tau') = h(\tau',\tau)$ and that $h(\tau,\tau') = 0$ for $\tau,\tau' < 0$. We see that the detection of a microwave pulse in the low-drive regime can be described by a second-order Volterra series introduced in Eq. (7.8), with $h(\tau,\tau')$ being the Volterra kernel. The detector thus acts as a non-linear filter for the input signal.

7.2.2 Wigner functions for the drive and the detector

We have now all the tools needed to introduce the Wigner functions for the drive and the detector, respectively.
We define the drive Wigner function similarly to the Wigner-Ville distribution in Eq. (7.3)

$$W_{\mathrm{f}}(t,\omega) = \frac{1}{2\pi}\int dy\, e^{-iy\omega} f(t+y/2)f^*(t-y/2). \tag{7.15}$$

The time and frequency marginals are given by

$$\begin{aligned} W_{\mathrm{f}}(t) &= \int d\omega\, W_{\mathrm{f}}(t,\omega) = |f(t)|^2, \\ W_{\mathrm{f}}(\omega) &= \int dt\, W_{\mathrm{f}}(t,\omega) = |\tilde{f}(\omega)|^2. \end{aligned} \tag{7.16}$$

Throughout Paper II, we study two commonly known and analytically tractable types of pulses, Gaussian and Lorentzian. The time-dependent amplitudes for the two pulse types are given by, respectively

$$f_{\mathrm{G}}(t) = \sqrt{\frac{\bar{N}}{\sigma\pi^{1/2}}} e^{-\frac{t^2}{2\sigma^2}}, \qquad f_{\mathrm{L}}(t) = \frac{\sqrt{\bar{N}\sigma}}{\sqrt{\pi}(t - i\sigma)}, \tag{7.17}$$

where σ denotes the width of the pulse and $\bar{N}$ gives the average number of photons in the pulse. Plugging the expressions in Eq. (7.17) into Eq. (7.15) gives the Wigner function for the two pulse types. We omit the analytical expressions here and only show the plots of the Wigner functions in Fig. 7.1 with their respective time and frequency marginals.

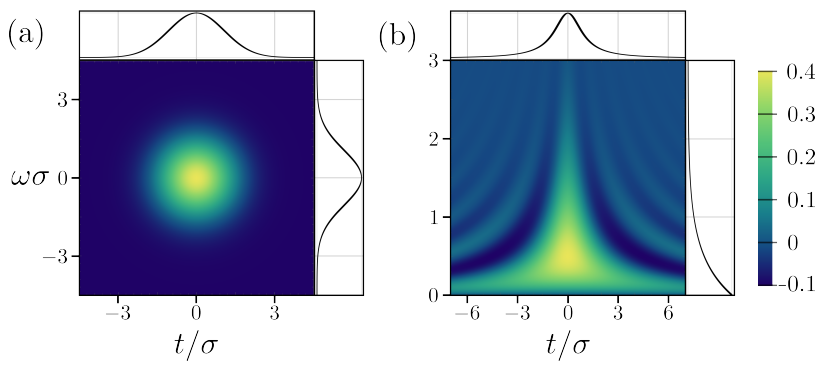

Figure 7.1: Normalized Wigner functions and their respective time and frequency marginals for (a), a Gaussian pulse and (b), a Lorentzian pulse. Note that the normalization is given by $\bar{N}$.

The detector Wigner function is defined in terms of the kernel $h(\tau, \tau')$ as

$$W_{\mathrm{d}}(t,\omega) = \frac{1}{2\pi} \int dy e^{-iy\omega} h(t + y/2, t - y/2). \tag{7.18}$$

It is important to note that, in general, $h(\tau,\tau') \neq h_1(\tau)h_1^*(\tau')$. Therefore, the kernel cannot be expressed in a similar way as the drive Wigner function defined in Eq. (7.15). This distinction makes the detector Wigner function formally analogous to the Wigner function of a mixed quantum state, whereas the drive Wigner function corresponds to that of a pure state. Additionally, the symmetry property ensures that $W_{\mathrm{d}}(t,\omega)$ is real, and

detector causality requires $W_{\mathrm{d}}(t,\omega) = 0$ for $t < 0$. The frequency and time marginals of $W_{\mathrm{d}}(t,\omega)$ are directly associated with the photocurrents obtained under a monochromatic and a delta-function pulse drive, respectively

$$\begin{aligned} W_{\mathrm{d}}(\omega_{\mathrm{l}}) &= \frac{I_{\mathrm{mc}}(\omega_{\mathrm{l}})/e}{\dot{N}} = \eta_{\mathrm{mc}}(\omega_{\mathrm{l}}), \\ W_{\mathrm{d}}(t) &= \frac{I_{\delta}(t+t_0)/e}{N_{\nu}}, \end{aligned} \tag{7.19}$$

where N_{ν} denotes the number of photons per unit bandwidth.
We find analytical expressions for the detector Wigner function in the limit of ideal photodetection introduced in Sec. 5.2 with the small difference that we relax the fifth condition, i.e. $\kappa \neq 4g^2/\tilde{\Gamma}$. We again omit the expressions here and show a plot of the detector Wigner function in Fig. 7.2 together with its respective marginals.

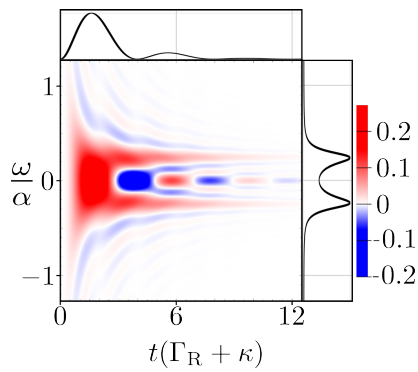

Figure 7.2: Normalized Wigner function of the detector with its respective time and frequency marginals for $\Gamma_{\mathrm{R}}/\kappa = 1$ and $4g^2/(\kappa\Gamma_{\mathrm{R}}) = 10$. The frequency is normalized by $\alpha = \sqrt{-(\Gamma_{\mathrm{R}}-\kappa)^2 + 16g^2}$. Note that the normalization of the Wigner function is given by $\bar{W}_{\mathrm{d}}$ (see main text).

We have noted before that the Wigner function is used in time-frequency analysis. In the context of the photodetector, being able to have accurate knowledge about the frequency of the photon and its arrival time would constitute a perfect detector. This is, however, prohibited by the Heisenberg-Gabor limit [116], which reads

$$\Delta t\, \Delta\omega \geq \frac{1}{2}, \tag{7.20}$$

where $\Delta\omega = \sqrt{\langle\omega^2\rangle - \langle\omega\rangle^2}$, $\Delta t = \sqrt{\langle t^2\rangle - \langle t\rangle^2}$ and $\langle x\rangle = \int dt d\omega\, x W_{\mathrm{d}}(t,\omega)/\bar{W}_{\mathrm{d}}$, where $\bar{W}_{\mathrm{d}} = \int d\omega dt\, W_{\mathrm{d}}(t,\omega)$. A detailed derivation of Eq. (7.20) is given in Paper II.

7.2.3 Photocurrent

The Wigner function formalism introduced above can be used to compute the photocurrent through

$$I(t)/e = \int d\tau d\omega \, W_{\mathrm{d}}(\tau, \omega) W_{\mathrm{f}}(t - \tau, \omega). \tag{7.21}$$

We have seen previously, in the case of monochromatic drives, that the photodetection efficiency is an important figure of merit to characterize the performance of the photodetector. For pulse drives, the time delay between in- and outgoing pulse and the overlap between them are important features as well. We thus analyze those three performance quantifiers by comparing the incoming drive pulse to the outgoing photocurrent pulse. The three quantifiers are defined as

1. The photodetection efficiency, which in the case of a pulse input is given by

$$\eta_{\mathrm{p}} = \frac{Q/e}{\bar{N}}, \tag{7.22}$$

   where $Q = \int dt \, I(t)$ is the average transferred charge in the electrical photocurrent pulse.

2. The average delay in time between the input and output signal, which is defined as

$$\tau_{\mathrm{d}} = \int dt \, t \left[\frac{I(t)/e}{Q} - \frac{|f(t)|^2}{\bar{N}} \right]. \tag{7.23}$$

3. The fidelity of the temporal shape transfer, or overlap, given by

$$O = \int dt \sqrt{\frac{|f(t - \tau_{\mathrm{d}})|^2}{\bar{N}} \cdot \frac{I(t)/e}{Q}}. \tag{7.24}$$

In the ideal-detector limit, we find that the bandwidth of the detector can be approximated by $\Gamma_{\mathrm{R}} + \kappa$. The ratio between the width of the pulse σ and the bandwidth of the detector is the key parameter quantifying the performance of the detector. We see in Fig. 7.3 that for a broadband photodetector, or similarly a very narrow pulse drive, the photodetection is almost ideal according to our figures of merit.

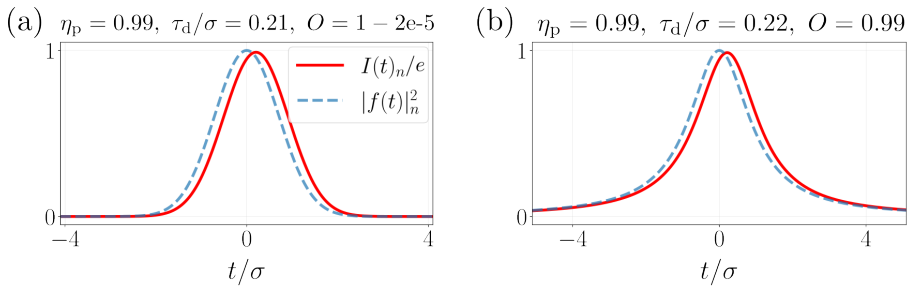

Figure 7.3: Normalized photocurrent in the ideal-detector limit and drive pulses for a Gaussian (a) and Lorentzian (b) drive for $\bar{N} = 0.1$, $\Gamma_\mathrm{R}/\kappa = 1$ and $\sigma(\Gamma_\mathrm{R} + \kappa)/2 = 10$. The efficiency is denoted by η_p, the time delay by τ_d and the overlap by O. Note that the normalization is given by $|f(t = 0)|^2$.

Chapter 8

Harvesting Power

Power – or energy – harvesting is the process of capturing and converting ambient energy from the environment into usable electrical power [117]. This technology leverages various sources, including solar and thermal energy, to power small electronic devices or sensors, particularly in embedded applications where traditional power sources are impractical. One of the most prominent fields within power harvesting is photovoltaics [118], where one uses solar cells consisting of semiconducting material to capture and transform the energy contained in the photons coming from the sun. But also thermoelectric devices, where a temperature gradient can be used to drive an electrical current, are gaining more interest, especially due to the rapidly growing field of quantum thermodynamics [119]. Power harvesting is also of great interest in other areas of quantum technology, such as quantum information processing or cQED [120]. Within these areas, the QD has offered an efficient platform to control the flow of energy and information.
We have also seen that QDs offer a promising platform to investigate the interaction of microwave photons and electrons. More specifically, we have seen that photons can be used to produce an electrical current through a DQD. Within the zero-bias configuration, this process produces no power that can be harvested. Applying a finite bias between source and drain changes that. If we can transport an electron from a lead of lower chemical potential to one of higher chemical potential through the assistance of a photon, we effectively produce a finite amount of power. The DQD-MR system can in this case thus convert the power from the incoming microwave drive to electrical power. This process is an analogue to the optical solar cell, where an electron is excited from the valence band to the conduction band of a reverse-biased photodiode through the absorption of a photon.

In this chapter, we demonstrate a microwave power-to-electrical energy conversion in a DQD-MR system. The general principle is depicted in Fig. 8.1. In Sec. 8.1, we present the experimental setup and device architecture. In Sec. 8.2, we fit zero-bias measurements to

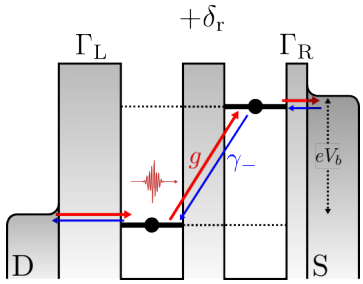

Figure 8.1: Schematic of the power-harvesting mechanism using a DQD-MR system. A finite (here negative) bias eV_b is applied between source (S) and drain (D). Power harvesting occurs when an electron is transported against the applied bias from S to D with the assistance of a photon from the MR. This process is depicted by the red arrows. There are also processes which counteract the harvesting, like electrons flowing with the bias from D to S and electrons relaxing from the excited to the ground state of the DQD. These processes are depicted by the blue arrows. There are two resonance points $\pm\delta_r$ where the DQD is on resonance with the MR. Depicted in the figure is $+\delta_r$, where the energy level of the left QD lies below that of the right QD. Note that, in this work, we use δ instead of ϵ to denote the detuning between left and right QD, and that the S is on the right and the D is on the left side. From the parameter extraction, we find that the rate Γ_R is around two orders of magnitude larger than Γ_L. This is depicted by the different widths of the barriers.

the theory to extract the system parameters. In Sec. 8.3, we present the power-harvesting analysis. In Sec. 8.4, we investigate some discrepancies between the experiment and theory, mainly focusing on a a regime that lies beyond the RWA in the Jaynes-Cummings model.

8.1 Setup and device

The device is shown in Fig 8.2. It consists of a semiconductor DQD dipole-coupled to a one-port waveguide MR. The DQD is created by three wurtzite barrier segments that confine electrons within two zinc-blende islands in an InAs nanowire. The electrochemical potentials of the left and right QD are controlled by plunger gate voltages V_L and V_R, respectively. The drain lead of the DQD is directly connected to the resonator, which has a fundamental resonance frequency of $f = 6.715$ GHz. The photocurrent I_{SD} across the DQD is measured at the resonator's voltage node. Measurements occur in a dilution refrigerator at an electronic temperature of $T_e \approx 60$ mK.

8.2 Zero-bias condition: Parameter extraction

We extract the relevant system parameters by fitting the photocurrent and reflectance at zero bias, see Fig. 8.3. The reflectance is the ratio between the reflected radiation and the incoming drive. Sweeping the frequency of the drive, the reflectance shows a dip at the resonance frequency of the MR. The reflectance is plotted in the Coulomb blockade regime, where the DQD and the MR are detuned, and at the two resonance points, where the

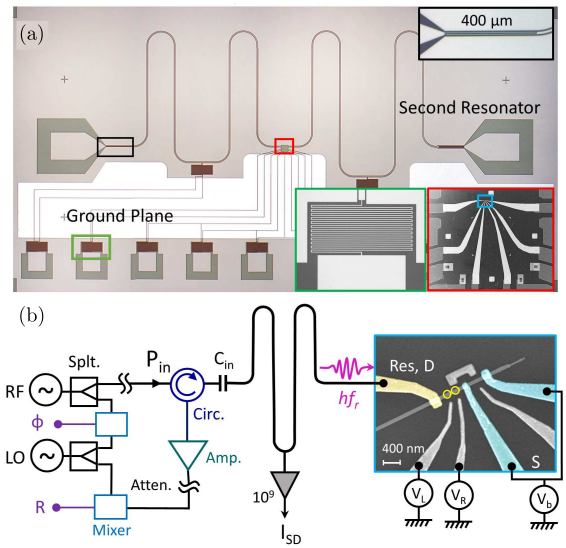

Figure 8.2: Figure taken from Paper III. (a) Optical micrograph of the device. The insets show the coupler of the resonator to the input port, inductive filtering on the dc lines, and the central part of the device showing the connections to the DQD. (c) False-colored scanning electron micrograph showing the nanowire with the schematic layout of the RF and transport measurement scheme. Bias is applied on the blue leads across the DQD (indicated by yellow circles) and the photocurrent I_{SD} is measured via the middle point of the resonator that directly connects the DQD (yellow lead).

level splitting of the DQD matches the frequency of the MR photons. The reflectance is derived using input-output theory, see App. A. The photocurrent is also plotted at the two resonance points and is fitted to the low- and large-drive expressions, respectively.

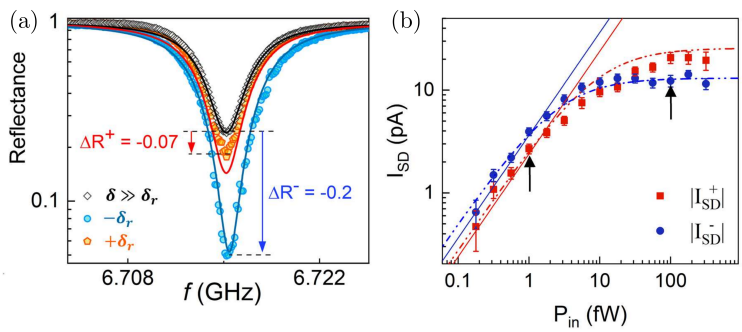

Figure 8.3: (a) Reflectance as a function of drive frequency measured in the Coulomb blockade regime, where the detuning between left and right QD δ is much larger than the resonance detuning δ_{r}, and at the two resonance points $\pm\delta_{\mathrm{r}}$ with $P_{\mathrm{in}} = hf\dot{N} = 1$ fW. (b) Photocurrent I_{SD} as a function of drive power P_{in} at the two resonance points. Solid (dashed-dotted) lines show the theoretically fitted curves at the low- (large-)drive regime.

The theory matches the experimental results well. From the fitting presented above, we ex-

tract the following parameters: $\Gamma_{\mathrm{L}}/(2\pi) = 27$ MHz, $\Gamma_{\mathrm{R}}/(2\pi) = 5400$ MHz, $\gamma_{-}/(2\pi) = 36$ MHz, $\gamma_{\phi}/(2\pi) = 1500$ MHz, $t_c/(2\pi) = 614$ MHz, $g/(2\pi) = 27$ MHz, $\kappa/(2\pi) = 5.1$ MHz and $\kappa_{\mathrm{in}}/(2\pi) = 3.8$ MHz.
An interesting feature to note in Fig 8.3(b) is the crossing of the two photocurrents as the input power is increased. This can be understood in the following way: For low drives, at $+\delta_{\mathrm{r}}$, the tunnel rate out of the excited state is much larger than at $-\delta_{\mathrm{r}}$ due to $\Gamma_{\mathrm{R}} \gg \Gamma_{\mathrm{L}}$. This results in a larger decoherence rate $\tilde{\Gamma}$ at $+\delta_{\mathrm{r}}$, which reduces the effective rate at which photons get absorbed by the DQD in analogy to the Zeno effect. Thus, the current at $+\delta_{\mathrm{r}}$ is smaller compared to the one at $-\delta_{\mathrm{r}}$. For large drives, the ground and excited states become equally populated, and thus the dynamics within the DQD can be neglected. Here, the saturation photocurrent only depends on the in- and out-tunneling rates and is given by $I^{*}_{\mathrm{SD}}/e = p_f/(1/\Gamma_{g0} + 2/\Gamma_{0e})$, with $p_f = (\Gamma_{g\mathrm{L}}\Gamma_{\mathrm{R}e} - \Gamma_{g\mathrm{R}}\Gamma_{\mathrm{L}e})/(\Gamma_{0e}\Gamma_{g0})$, where the factor of 2 arises from the fact that the DQD spends only half of the time in the excited state. In the limit of large asymmetry $\Gamma_{\mathrm{L}} \ll \Gamma_{\mathrm{R}}$, the smallest rate among Γ_{g0} and Γ_{0e} determines the saturation current. Since that rate is smaller at $-\delta_{\mathrm{r}}$ compared to $+\delta_{\mathrm{r}}$, the photocurrent is also smaller.

8.3 Finite-bias condition: Power harvesting

By applying a bias, the chemical potential of the leads move closer to the energy levels of the QDs as in Fig. 8.1. The temperature of the leads thus becomes important and we have to include it into the theoretical model. To that end, we work with the full master equation (5.44), with the small addition that we still take the zero-temperature limit for the bosonic bath. The applied bias enters into the Fermi-Dirac distributions according to Eq. (5.3). We start by varying the bias and computing the maximal photocurrent in the two detuning conditions $\pm\delta$ numerically using QuTip [121], see Fig. 8.4(a)-(b). We do so for two values of the applied microwave drive, 1 fW and 100 fW, which represent the low- and large-drive regimes, respectively, with linear and non-linear response to the photon flux, see the black arrows in Fig. 8.3(b). By multiplying the photocurrent with the applied bias, we get the electrical power out $P_{\mathrm{out}} = I_{\mathrm{SD}}V_b$, which is plotted in Fig. 8.4(c)-(d). The shaded region indicates the harvesting regime, where the photocurrent flows against the applied bias. The relevant figure of merit for this work is the power-harvesting efficiency, plotted in Fig. 8.4(e)-(f), which is defined by the electrical power out divided by the microwave drive power in

$$\eta_E = \frac{P_{\mathrm{out}}}{P_{\mathrm{in}}} = \frac{I_{\mathrm{SD}}V_b}{hf\dot{N}}. \tag{8.1}$$

We see that the efficiency increases first linearly with the applied bias. In the low-drive regime, the efficiency starts decreasing after the bias hits half the resonance detuning δ_{r}, which is around 13 μeV, meaning that only single-photon absorption events contribute

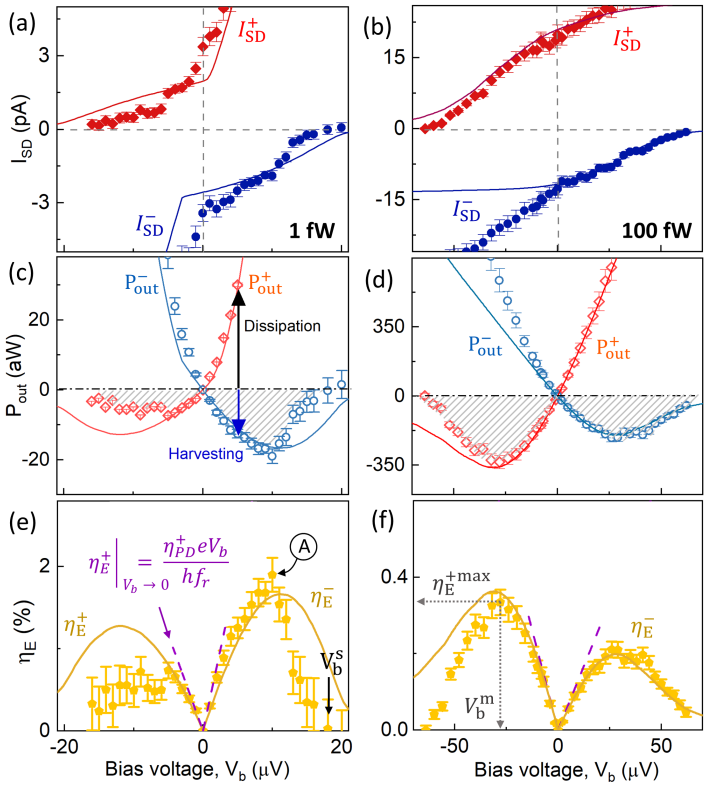

Figure 8.4: Figure taken from Paper III. Photocurrent measured across an applied bias V_b for (a) 1 fW and (b) 100 fW input drive power. The solid lines depict the numerically calculated results for the two detuning configurations. Panels (c)-(d) show the corresponding output power, where the shaded regions indicate the harvesting regimes, and panels (e)-(f) show the corresponding power-harvesting efficiency η_E for the two input powers. The maximum efficiency of 2 % is marked with (A) in figure (e). The stopping bias voltage V_b^s denotes the bias at which the efficiency drops to zero and the maximum bias voltage V_b^m denotes the bias at which the efficiency is maximal. The dashed lines in panels (e)-(f) show the power-harvesting efficiency for zero bias, where η_{PD} denotes the photodetection efficiency.

to the power harvesting. It is also in the low-drive regime that we reach the maximum efficiency of 2 %. In the large-drive regime, we see that power harvesting occurs even at an applied bias that is on the order of twice the photon energy. We attribute this effect to multi-photon absorption events, something that our current model does not capture and will be discussed in the next section.

8.4 Beyond the RWA

In order to capture the multi-photon absorptions, we need to omit the RWA in our model and work with the light-matter interaction Hamiltonian in Eq. (5.33). Moving to the frame

rotating at the drive frequency ω_1, we find

$$\hat{H}_{\mathrm{MD}} = g_z\hat{\sigma}_z(\hat{a}^\dagger e^{i\omega_1 t} + \hat{a}e^{-i\omega_1 t}) + g_x(\hat{a}^\dagger\hat{\sigma}_- + \hat{a}\hat{\sigma}_+ + \hat{a}^\dagger\hat{\sigma}_+ e^{2i\omega_1 t} + \hat{a}\hat{\sigma}_- e^{-2i\omega_1 t}), \quad (8.2)$$

where we have defined $g_x = g_0\sin(\theta)$ and $g_z = g_0\cos(\theta)$. To see that this Hamiltonian indeed accounts for multi-photon processes, we plot the photocurrent numerically as a function of the normalized detuning $\delta/\delta_{\mathrm{r}}$ for zero bias in Fig. 8.5. We observe finite

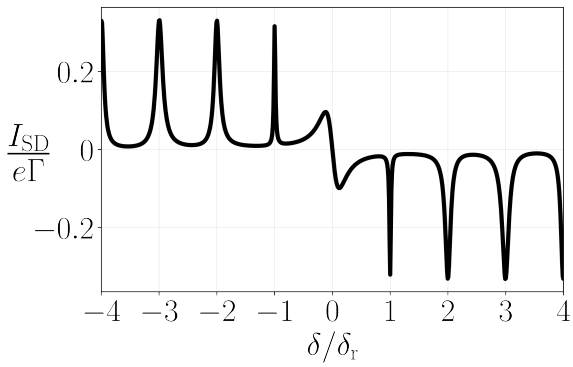

Figure 8.5: Photocurrent as a function of the normalized detuning using the beyond RWA theory. The rates chosen for this plot are: $\Gamma_{\mathrm{L}}/(2\pi) = \Gamma_{\mathrm{R}}/(2\pi) = \Gamma/(2\pi) = 26$ MHz, $P_{\mathrm{in}} = 100$ fW, $\gamma_\phi/(2\pi) = \gamma_-/(2\pi) = 0$ MHz. The rest of the rates are the same as in the experiment.

current peaks at integer multiples of the resonance detuning. To clearly display these peaks, we have used electron-tunneling rates significantly lower than those measured experimentally. The large rate Γ_{R} found from the experimental data leads to a broadening of those resonance peaks. This broadening also accounts for the finite current seen at bias voltages exceeding δ_{r} using the standard Jaynes-Cummings model with the RWA, c.f. Fig. 8.4(b). In Fig. 8.6, we plot the photocurrent as a function of detuning using the Jaynes-Cummings model and the experimental rates. We clearly see the broadening of the peaks, which extends beyond a detuning that is twice as large as δ_{r}.

We also try to fit the full, beyond RWA theory to the experimental data using the parameters found in the previous section. Fig. 8.7 presents the numerically calculated power-harvesting efficiency for negative bias voltages using the Hamiltonian in Eq. (8.2). Although this model includes multi-photon processes, the fit shows increased deviation from experimental data. Specifically, the theoretical prediction extends much further as a function of bias voltage than observed experimentally. This suggests that additional mechanisms in the experiment, not captured by our current model, may reduce the maximum achievable power-harvesting efficiency. One possible such mechanism is the shifting of the chemical potential of the drain due to the high input power, something which has been found experimentally [122]. Another possibility is cotunneling events of electrons through the DQD [123]. Including those additional mechanisms was beyond the scope of this work, but would be of great interest for future investigations.

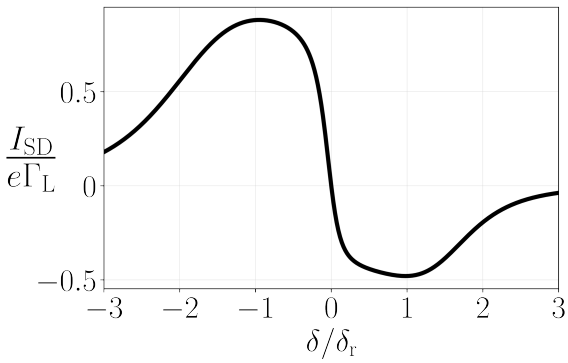

Figure 8.6: Photocurrent as a function of the normalized detuning using the standard Jaynes-Cumming model. The rates chosen are the experimental ones together with $P_{\mathrm{in}} = 100$ fW.

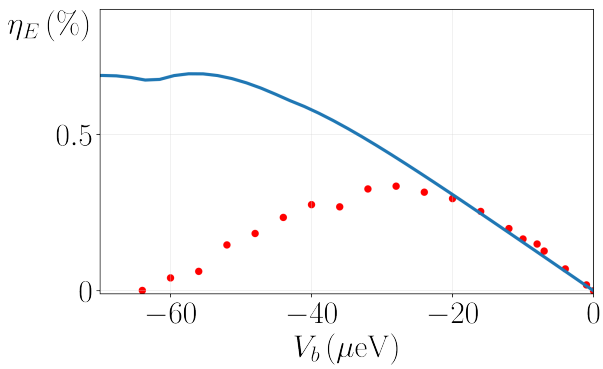

Figure 8.7: Power-harvesting efficiency as a function of bias voltage for an input power of $P_{\mathrm{in}} = 100$ fW using the experimental parameters. The experimental data (points) is compared to the theoretical result (full line), which was computed numerically and used the beyond RWA theory.

Chapter 9

Outlook

The results of this thesis pose several interesting open questions. We will summarize some of those we find most relevant here.

In Papers I and II, we theoretically investigated the photocurrent for two different types of coherent drives, a monochromatic continuous wave and a single pulse. It would be of great interest to investigate different types of drives, specifically non-classical ones such as squeezed or Fock states. The results from Paper I also assume that every single electron tunneling out of the DQD can be measured. This is of course a very idealized assumption. In real experiments, measuring single electron tunneling events is very difficult, as those events typically occur on a fast time scale, which is difficult to resolve. Also, in actual experiments there typically is some kind of feedback induced on the system through the measurement device. Both the investigation of an extended device which also includes the detector for the electrons and describes the measurement and feedback would be of interest. One possible setup that is currently being tested experimentally is to have a SET connected to the DQD and infer the charge state of the DQD through the current in the SET. In Paper II, we assume that the time-dependent photocurrent pulse can be accessed. This, too, is experimentally challenging. Also here it would be interesting to study a system where the time-dependent photodetector is part of the whole setup.

As mentioned previously, in the case of single pulse detection, the study would be more complete with a Wigner-function formalism for the photocurrent. This might include some form of input-output theory, where the tricky part is the input is bosonic and the output fermionic in nature.

We have also in several parts of our work used a mean-field approximation, which to our surprise worked very well. It is not clear why this is the case, and it would be beneficial to also investigate when the approximation works well and when it doesn't and why that would be the case.

In Paper III, we saw that though the non-RWA Hamiltonian accounted for multi-photon

processes, it did not reproduce the experimental data accurately. As mentioned, the shift in the chemical potential due to the high input drive could be a cause. Introducing this shift in the theoretical model might solve the issue we had there. We also found electron-tunneling rates between the leads that where on the order of the DQD energy gap. Typically, this means that standard Markovian Lindblad equation does not hold anymore. Effects of non-Markovianity would therefore also be interesting.
We have also in our collaborations with the experimentalists seen signs of cotunneling events, which could be one more possible extension to the model.

We see that there are many different paths that could be followed which build up on the results presented in this thesis.

References

[1] S. Datta. *Quantum Transport: Atom to Transistor*. Cambridge University Press, 2005.

[2] R. C. Ashoori. Electrons in artificial atoms. *Nature*, 379:413–419, 1996.

[3] M. A. Kastner. The single-electron transistor. *Rev. Mod. Phys.*, 64:849–858, 1992.

[4] K. Ono, D. G. Austing, Y. Tokura, and S. Tarucha. Spin selective tunneling and blockade in two-electron double quantum dot. *Phys. Status Solidi B*, 238(2):335–340, 2003.

[5] K. Ishibashi and Y. Aoyagi. Interaction of electromagnetic wave with quantum dots. *Phys. B: Condensed Matter*, 314(1):437–443, 2002.

[6] T. Fujisawa, T. Hayashi, S. W. Jung, Y.-H. Jeong, and Y. Hirayama. *Single-electron charge qubit in a double quantum dot*, pages 279–287. Springer New York, New York, NY, 2006.

[7] D. Loss and D. P. DiVincenzo. Quantum computation with quantum dots. *Phys. Rev. A*, 57:120–126, 1998.

[8] E. Waks. Coherent control of light-matter interactions using a quantum dot in a cavity. In *Frontiers in Optics 2014*, page LTh1H.1. Optica Publishing Group, 2014.

[9] W. Greiner and J. Reinhardt. *Quantum Electrodynamics*. Springer Berlin, Heidelberg, 2008.

[10] S. M. Dutra. *Cavity Quantum Electrodynamics*. John Wiley & Sons, Ltd, 2004.

[11] X. Zhang, C. Xu, and Z. Ren. High fidelity heralded single-photon source using cavity quantum electrodynamics. *Sci. Rep.*, 8:3140, 2018.

[12] R. J. Lewis-Swan, D. Barberena, J. A. Muniz, J. R. K. Cline, D. Young, J. K. Thompson, and A. M. Rey. Protocol for precise field sensing in the optical domain with cold atoms in a cavity. *Phys. Rev. Lett.*, 124:193602, 2020.

[13] A. Blais, A. L. Grimsmo, S. M. Girvin, and A. Wallraff. Circuit quantum electrodynamics. *Rev. Mod. Phys.*, 93:025005, 2021.

[14] M. AbuGhanem. IBM Quantum Computers: Evolution, Performance, and Future Directions. *arXiv:2410.00916*, 2024.

[15] A. Stockklauser, P. Scarlino, J. V. Koski, S. Gasparinetti, C. K. Andersen, C. Reichl, W. Wegscheider, T. Ihn, K. Ensslin, and A. Wallraff. Strong coupling cavity qed with gate-defined double quantum dots enabled by a high impedance resonator. *Phys. Rev. X*, 7:011030, 2017.

[16] M. Reagor, W. Pfaff, C. Axline, R. W. Heeres, N. Ofek, K. Sliwa, E. Holland, C. Wang, J. Blumoff, K. Chou, M. J. Hatridge, L. Frunzio, M. H. Devoret, L. Jiang, and R. J. Schoelkopf. Quantum memory with millisecond coherence in circuit qed. *Phys. Rev. B*, 94:014506, 2016.

[17] A. Wallraff, D. I. Schuster, A. Blais, L. Frunzio, R.-S. Huang, J. Majer, S. Kumar, S. M. Girvin, and R. J. Schoelkopf. Strong coupling of a single photon to a superconducting qubit using circuit quantum electrodynamics. *Nature*, 431:162–167, 2004.

[18] L. E Bruhat, T. Cubaynes, J. J. Viennot, M. C. Dartiailh, M. M. Desjardins, A. Cottet, and T. Kontos. Circuit qed with a quantum-dot charge qubit dressed by cooper pairs. *Phys. Rev. B*, 98:155313, 2018.

[19] G. Burkard, M. J. Gullans, X. Mi, and J. R. Petta. Superconductor–semiconductor hybrid-circuit quantum electrodynamics. *Nat. Rev. Phys.*, 2:129–140, 2020.

[20] C. H. Wong and M. G. Vavilov. Quantum efficiency of a single microwave photon detector based on a semiconductor double quantum dot. *Phys. Rev. A*, 95:012325, 2017.

[21] P. Kurpiers, M. Pechal, B. Royer, P. Magnard, T. Walter, J. Heinsoo, Y. Salathé, A. Akin, S. Storz, J.-C. Besse, S. Gasparinetti, A. Blais, and A. Wallraff. Quantum communication with time-bin encoded microwave photons. *Phys. Rev. Appl.*, 12:044067, 2019.

[22] M. Casariego, E. Zambrini Cruzeiro, S. Gherardini, T. Gonzalez-Raya, R. André, G. Frazão, G. Catto, M. Möttönen, D. Datta, K. Viisanen, J. Govenius, M. Prunnila, K. Tuominen, M. Reichert, M. Renger, K. G. Fedorov, F. Deppe, H. van der Vliet, A. J. Matthews, Y. Fernández, R. Assouly, R. Dassonneville, B. Huard, M. Sanz, and Y. Omar. Propagating quantum microwaves: towards applications in communication and sensing. *Quantum Sci. Technol.*, 8(2):023001, 2023.

[23] R. Cervantes, G. Carosi, C. Hanretty, S. Kimes, B. H. LaRoque, G. Leum, P. Mohapatra, N. S. Oblath, R. Ottens, Y. Park, G. Rybka, J. Sinnis, and J. Yang. Search for 70 μeV dark photon dark matter with a dielectrically loaded multiwavelength microwave cavity. *Phys. Rev. Lett.*, 129:201301, 2022.

[24] T. P. Pearsall. *Photonics Essentials*. McGraw-Hill, New York, 2003.

[25] S. Haldar, H. Havir, W. Khan, D. Zenelaj, P. P. Potts, S. Lehmann, K. A. Dick, P. Samuelsson, and V. F. Maisi. High-efficiency microwave photodetection by cavity coupled double dots with single cavity-photon sensitivity. *arXiv:2406.03047*, 2024.

[26] S. Haldar, D. Barker, H. Havir, A. Ranni, S. Lehmann, K. A. Dick, and V. F. Maisi. Continuous microwave photon counting by semiconductor-superconductor hybrids. *Phys. Rev. Lett.*, 133:217001, 2024.

[27] M. Liu, N. Yazdani, M. Yarema, M. Jansen, V. Wood, and E. H. Sargent. Colloidal quantum dot electronics. *Nat. Electron.*, 4:548–558, 2021.

[28] B. J. Riel. An introduction to self-assembled quantum dots. *Am. J. Phys.*, 76(8):750–757, 08 2008.

[29] G.-W. Deng, N. Xu, and W.-J. Li. *Gate-Defined Quantum Dots: Fundamentals and Applications*, pages 107–133. Springer International Publishing, Cham, 2020.

[30] G. Burkard, T. D. Ladd, A. Pan, J. M. Nichol, and J. R. Petta. Semiconductor spin qubits. *Rev. Mod. Phys.*, 95:025003, 2023.

[31] E. Jang and H. Jang. Review: Quantum dot light-emitting diodes. *Chem. Rev.*, 123(8):4663–4692, 2023.

[32] H. M. Gil, T. W. Price, K. Chelani, J.-S. G. Bouillard, S. D.J. Calaminus, and G. J. Stasiuk. NIR-quantum dots in biomedical imaging and their future. *iScience*, 24(3):102189, 2021.

[33] A. A. H. Abdellatif, M. A. Younis, M. Alsharidah, O. Al Rugaie, and H. M. Tawfeek. Biomedical applications of quantum dots: Overview, challenges, and clinical potential. *Int. J. Nanomedicine*, 2022.

[34] W. G. van der Wiel, S. De Franceschi, J. M. Elzerman, T. Fujisawa, S. Tarucha, and L. P. Kouwenhoven. Electron transport through double quantum dots. *Rev. Mod. Phys.*, 75:1–22, 2002.

[35] F. D. Ribetto, R. A. Bustos-Marún, and H. L. Calvo. Role of coherence in quantum-dot-based nanomachines within the coulomb blockade regime. *Phys. Rev. B*, 103:155435, 2021.

[36] S. Abdel-Khalek, K. Berrada, and A. Alkaoud. Nonlocality and coherence in double quantum dot systems. *Phys. E*, 130:114679, 2021.

[37] Z. Zhang, C. You, O. S. Maga na Loaiza, R. Fickler, R. de J. León-Montiel, J. P. Torres, T. S. Humble, S. Liu, Y. Xia, and Q. Zhuang. Entanglement-based quantum information technology: a tutorial. *Adv. Opt. Photon.*, 16(1):60–162, 2024.

[38] A. Lasek, H. V. Lepage, K. Zhang, T. Ferrus, and C. H. W. Barnes. Pulse-controlled qubit in semiconductor double quantum dots. *Sci. Rep.*, 13:21369, 2023.

[39] K. Takeda, A. Noiri, T. Nakajima, L. C. Camenzind, T. Kobayashi, A. Sammak, G. Scappucci, and S. Tarucha. Rapid single-shot parity spin readout in a silicon double quantum dot with fidelity exceeding 99%. *npj Quantum Inf.*, 10:22, 2024.

[40] P. Senellart, G. Solomon, and A. White. High-performance semiconductor quantum-dot single-photon sources. *Nature Nanotech.*, 12:1026–1039, 2017.

[41] K. Xiong, X. Li, Y. Wei, W. Wu, C. Zhang, J. Liu, Y. Chen, and P. Chen. Efficient generation of single photons by quantum dots embedded in bullseye cavities with backside dielectric mirrors. *Opt. Express*, 31(12):19536–19543, 2023.

[42] H. Bruus and K. Flensberg. *Many-Body Quantum Theory in Condensed Matter Physics: An Introduction*. Oxford University Press, 2004.

[43] A. Webb. Cavity- and waveguide-resonators in electron paramagnetic resonance, nuclear magnetic resonance, and magnetic resonance imaging. *Prog. Nucl. Magn. Reson. Spectrosc.*, 83:1–20, 2014.

[44] R. J. Cameron, C. M. Kudsia, and R. R. Mansour. *Microwave Resonators*, pages 373–394. Wiley Telecom, 2018.

[45] J. Gao. *The Physics of Superconducting Microwave Resonators*. PhD thesis, California Institute of Technology, 2008.

[46] Y.-L. Chen, Y.-F. Xiao, X. Zhou, X.-B. Zou, Z.-W. Zhou, and G.-C. Guo. Single-photon transport in a transmission line resonator interacting with two capacitively coupled cooper-pair boxes. *J. Phys. B: At. Mol. Opt. Phys.*, 41(17):175503, 2008.

[47] U. Alushi, T. Ramos, J. J. García-Ripoll, R. Di Candia, and S. Felicetti. Waveguide qed with quadratic light-matter interactions. *PRX Quantum*, 4:030326, 2023.

[48] A. Krasnok, P. Dhakal, A. Fedorov, P. Frigola, M. Kelly, and S. Kutsaev. Advancements in superconducting microwave cavities and qubits for quantum information systems. *arXiv:2304.09345*, 2023.

[49] S. Mahashabde, E. Otto, D. Montemurro, S. de Graaf, S. Kubatkin, and A. Danilov. Fast tunable high-Q-factor superconducting microwave resonators. *Phys. Rev. Appl.*, 14:044040, 2020.

[50] U. Vool and M. Devoret. Introduction to quantum electromagnetic circuits. *Int. J. Circ. Theor. Appl.*, 45(7):897–934, 2017.

[51] M. H. Devoret. Quantum fluctuations in electrical circuits. In *Les Houches, Session LXIII 7.8*, pages 133–135, 1995.

[52] H. J. Kimble. Strong interactions of single atoms and photons in cavity QED. *Phys. Scr.*, 1998(T76):127, 1998.

[53] G. S. Agarwal. Vacuum-field Rabi oscillations of atoms in a cavity. *J. Opt. Soc. Am. B*, 2(3):480–485, 1985.

[54] P. R. Rice, J. Gea-Banacloche, M. L. Terraciano, D. L. Freimund, and L. A. Orozco. Steady state entanglement in cavity QED. *Opt. Express*, 14(10):4514–4524, 2006.

[55] P. Grangier, G. Reymond, and N. Schlosser. Implementations of quantum computing using cavity quantum electrodynamics schemes. *Fortschr. Phys.*, 48(9-11):859–874, 2000.

[56] J. L. Bromberg. The birth of the laser. *Physics Today*, 41:26–33, 1988.

[57] O.-P. Saira, M. Zgirski, K. L. Viisanen, D. S. Golubev, and J. P. Pekola. Dispersive thermometry with a josephson junction coupled to a resonator. *Phys. Rev. Appl.*, 6:024005, 2016.

[58] A. Peugeot, G. Ménard, S. Dambach, M. Westig, B. Kubala, Y. Mukharsky, C. Altimiras, P. Joyez, D. Vion, P. Roche, D. Esteve, P. Milman, J. Leppäkangas, G. Johansson, M. Hofheinz, J. Ankerhold, and F. Portier. Generating two continuous entangled microwave beams using a DC-biased Josephson junction. *Phys. Rev. X*, 11:031008, 2021.

[59] T. Niemczyk, F. Deppe, H. Huebl, E. P. Menzel, F. Hocke, M. J. Schwarz, J. J. Garcia-Ripoll, D. Zueco, T. Hümmer, E. Solano, A. Marx, and R. Gross. Circuit quantum electrodynamics in the ultrastrong-coupling regime. *Nature Phys.*, 6:772–776, 2010.

[60] R. Kuzmin, N. Mehta, N. Grabon, R. Mencia, and V. E. Manucharyan. Superstrong coupling in circuit quantum electrodynamics. *npj Quantum Inf.*, 5:20, 2019.

[61] Z.-B. Feng. Quantum state transfer between hybrid qubits in a circuit QED. *Phys. Rev. A*, 85:014302, 2012.

[62] F. Armata, G. Calajo, T. Jaako, M. S. Kim, and P. Rabl. Harvesting multiqubit entanglement from ultrastrong interactions in circuit quantum electrodynamics. *Phys. Rev. Lett.*, 119:183602, 2017.

[63] M. Pechal, L. Huthmacher, C. Eichler, S. Zeytinoğlu, A. A. Abdumalikov, S. Berger, A. Wallraff, and S. Filipp. Microwave-controlled generation of shaped single photons in circuit quantum electrodynamics. *Phys. Rev. X*, 4:041010, 2014.

[64] R.-Y. Yan and Z.-B. Feng. Fast generation of microwave photon fock states in a superconducting nanocircuit. *Phys. E*, 127:114522, 2021.

[65] M. Bina. The coherent interaction between matter and radiation. *Eur. Phys. J. Spec. Top.*, 203:163–183, 2012.

[66] D.A. Steck. *Quantum and Atom Optics*. 2007.

[67] D. F. Walls and G. J. Milburn. *Quantum Optics*. Springer Berlin, Heidelberg, 2007.

[68] E. T. Jaynes and F. W. Cummings. Comparison of quantum and semiclassical radiation theories with application to the beam maser. *Proc. IEEE*, 51(1):89, 1963.

[69] H.-P. Breuer and F. Petruccione. *The Theory of Open Quantum Systems*. Oxford University Press, 2002.

[70] G. Schaller. *Open Quantum Systems Far from Equilibrium*. Springer Cham, 2014.

[71] L. Chirolli and G. Burkard. Decoherence in solid-state qubits. *Advances in Physics*, 57(3):225–285, 2008.

[72] Y.-X. Gong, Y.-S. Zhang, Y.-L. Dong, X.-L. Niu, Y.-F. Huang, and G.-C. Guo. Dependence of the decoherence of polarization states in phase-damping channels on the frequency spectrum envelope of photons. *Phys. Rev. A*, 78:042103, Oct 2008.

[73] C. W. Gardiner. *Handbook of Stochastic Methods*. Springer, 1985.

[74] M. A. Nielsen and I. L. Chuang. *Quantum Computation and Quantum Information: 10th Anniversary Edition*. Cambridge University Press, 2010.

[75] G. Lindblad. On the generators of quantum dynamical semigroups. *Commun. Math. Phys.*, 48:119, 1976.

[76] A.G. Redfield. The theory of relaxation processes. In J. S. Waugh, editor, *Advances in Magnetic Resonance*, volume 1, pages 1–32. Academic Press, 1965.

[77] D. Chruściński and S. Pascazio. A brief history of the GKLS equation. *Open Systems & Information Dynamics*, 24(03):1740001, 2017.

[78] L. Childress, A. S. Sørensen, and M. D. Lukin. Mesoscopic cavity quantum electrodynamics with quantum dots. *Phys. Rev. A*, 69:042302, 2004.

[79] W. Khan, P. P. Potts, S. Lehmann, C. Thelander, P. Samuelsson, and V. F. Maisi. Efficient and continuous microwave photoconversion in hybrid cavity-semiconductor nanowire double quantum dot diodes. *Nat. Commun.*, 12:5130, 2021.

[80] E. Artacho and L. M. Falicov. Open fermionic quantum systems. *Phys. Rev. B*, 47:1190–1198, 1993.

[81] N. Anto-Sztrikacs and D. Segal. Strong coupling effects in quantum thermal transport with the reaction coordinate method. *New J. Phys.*, 23(6):063036, 2021.

[82] M. Büttiker. *Capacitance, Charge Fluctuations and Dephasing in Coulomb Coupled Conductors*. Springer, Berlin, 2001.

[83] A. Grodecka-Grad and J. Förstner. Theory of phonon-mediated relaxation in doped quantum dot molecules. *Phys. Rev. B*, 81:115305, 2010.

[84] F. Marquardt and A. Püttmann. Introduction to dissipation and decoherence in quantum systems. *arXiv:0809.4403*, 2008.

[85] G. A. Prataviera and S. S. Mizrahi. Many-particle Sudarshan-Lindblad equation: mean-field approximation, nonlinearity and dissipation in a spin system. *Rev. Bras. Ensino Fís.*, 36:4, 2014.

[86] D. Plankensteiner, C. Hotter, and H. Ritsch. QuantumCumulants.jl: A Julia framework for generalized mean-field equations in open quantum systems. *Quantum*, 6:617, 2022.

[87] C. Beenakker and C. Schönenberger. Quantum shot noise. *Physics Today*, 56(5):37–42, 2003.

[88] W. Belzig. Full counting statistics of super-poissonian shot noise in multilevel quantum dots. *Phys. Rev. B*, 71:161301, 2005.

[89] G. Kießlich, P. Samuelsson, A. Wacker, and E. Schöll. Counting statistics and decoherence in coupled quantum dots. *Phys. Rev. B*, 73:033312, 2006.

[90] Y. V. Nazarov and Y. M. Blanter. *Quantum Transport*. Cambridge University Press, Cambridge, 2009.

[91] C. Xu and M. G. Vavilov. Full counting statistics of photons emitted by a double quantum dot. *Phys. Rev. B*, 88:195307, 2013.

[92] C. Fricke, F. Hohls, W. Wegscheider, and R. J. Haug. Bimodal counting statistics in single-electron tunneling through a quantum dot. *Phys. Rev. B*, 76:155307, 2007.

[93] L. S. Levitov, H. Lee, and G. B. Lesovik. Electron counting statistics and coherent states of electric current. *J. Math. Phys.s*, 37(10):4845–4866, 1996.

[94] W. Belzig and Yu. V. Nazarov. Full counting statistics of electron transfer between superconductors. *Phys. Rev. Lett.*, 87:197006, 2001.

[95] D. A. Bagrets and Yu. V. Nazarov. Full counting statistics of charge transfer in coulomb blockade systems. *Phys. Rev. B*, 67:085316, 2003.

[96] N. Ubbelohde, C. Fricker, C. Flindt, F. Hohls, and R. J. Haug. Measurement of finite-frequency current statistics in a single-electron transistor. *Nat. Commun.*, 3:612, 2012.

[97] D. K. C. Macdonald. Spontaneous fluctuations. *Rep. Prog. Phys.*, 12(1):56–81, jan 1949.

[98] C. Flindt, T. Novotný, and A.-P. Jauho. Current noise spectrum of a quantum shuttle. *Phys. E*, 29(1):411–418, 2005.

[99] E. Wigner. On the quantum correction for thermodynamic equilibrium. *Phys. Rev.*, 40:749–759, 1932.

[100] T. L. Curtright and C. K. Zachos. Quantum mechanics in phase space. *Asia Pacific Physics Newsletter*, 01(01):37–46, 2012.

[101] D. K. Ferry and M. Nedjalkov. *The Wigner Function in Science and Technology*. 2053-2563. IOP Publishing, 2018.

[102] M. A. Alonso. Wigner functions in optics: describing beams as ray bundles and pulses as particle ensembles. *Adv. Opt. Photon.*, 3(4):272–365, 2011.

[103] F. S. Roux and N. Fabre. Wigner functional theory for quantum optics. *arXiv:1901.07782*, 2020.

[104] J. P. Paz, A. J. Roncaglia, and M. Saraceno. Qubits in phase space: Wigner-function approach to quantum-error correction and the mean-king problem. *Phys. Rev. A*, 72:012309, 2005.

[105] D. Ferraro, A. Feller, A. Ghibaudo, E. Thibierge, E. Bocquillon, G. Fève, Ch. Grenier, and P. Degiovanni. Wigner function approach to single electron coherence in quantum Hall edge channels. *Phys. Rev. B*, 88:205303, 2013.

[106] B. Boashash. Note on the use of the Wigner distribution for time-frequency signal analysis. *IEEE Trans. Acoust., Speech, Signal. Process.*, 36(9):1518, 1988.

[107] L. Debnath. *The Wigner-Ville Distribution and Time-Frequency Signal Analysis*, pages 307–360. Birkhäuser Boston, Boston, MA, 2002.

[108] D. Dragoman. Applications of the Wigner distribution function in signal processing. *EURASIP J. Adv. Signal Process.*, 2005:264967, 2005.

[109] D. J. Griffiths and D. F. Schroeter. *Introduction to Quantum Mechanics*. Cambridge University Press, 3 edition, 2018.

[110] L. Cohen. Time-frequency distributions-a review. *Proc. IEEE*, 77(7):941, 1989.

[111] T. Kelemenová, O. Benedik, and I. Koláriková. Signal noise reduction and filtering. *Ac. Mech.*, 5:29–34, 06 2020.

[112] S. O. Rice. Volterra systems with more than one input port—distortion in a frequency converter. *Bell Syst. Tech. J.*, 52(8):1255, 1973.

[113] C. Crespo-Cadenas, M. J. Madero-Ayora, J. Reina-Tosina, and J.A. Becerra-González. Formal deduction of a volterra series model for complex-valued systems. *Sig. Proc.*, 131:245, 2017.

[114] B. Roussel, C. Cabart, and P. Degiovanni. Quantum signal processing for electron quantum optics. In *Quantum Information and Measurement (QIM) 2017*, page QW5A.1. Optica Publishing Group, 2017.

[115] D. S. Glattli and P. S. Roulleau. Levitons for electron quantum optics. *Phys. Status Solidi B*, 254(3):1600650, 2017.

[116] D. Gabor. Theory of communication. Part 1: The analysis of information. *Proc. Inst. Electr. Eng.*, 93:429, 1946.

[117] A. Georgiadis, A. Collado, and M. M. Tentzeris. *Energy Harvesting: Technologies, Systems, and Challenges*. EuMA High Frequency Technologies Series. Cambridge University Press, 2021.

[118] T. Markvart A. McEvoy and L. Castañer. *Practical Handbook of Photovoltaics*. Elsevier Ltd., 2012.

[119] J. P. Pekola. Towards quantum thermodynamics in electronic circuits. *Nat. Phys.*, 11(2):118–123, 2015.

[120] R. Kokkoniemi, J.-P. Girard, D. Hazra, A. Laitinen, J. Govenius, R. E. Lake, I. Sallinen, V. Vesterinen, M. Partanen, and J. Y. Tan. Bolometer operating at the threshold for circuit quantum electrodynamics. *Nature*, 586(7827):47–51, 2020.

[121] J.R. Johansson, P.D. Nation, and Franco Nori. Qutip: An open-source python framework for the dynamics of open quantum systems. *Comput. Phys. Commun.*, 183(8):1760–1772, 2012.

[122] S. Haldar, H. Havir, W. Khan, S. Lehmann, C. Thelander, K. A. Dick, and V. F. Maisi. Energetics of microwaves probed by double quantum dot absorption. *Phys. Rev. Lett.*, 130:087003, 2023.

[123] J. N. Pedersen and A. Wacker. Modeling of cotunneling in quantum dot systems. *Phys. E*, 42(3):595–599, 2010.

[124] C. W. Gardiner and M. J. Collett. Input and output in damped quantum systems: Quantum stochastic differential equations and the master equation. *Phys. Rev. A*, 31:3761–3774, 1985.

[125] A. H. Kiilerich and K. Mølmer. Input-output theory with quantum pulses. *Phys. Rev. Lett.*, 123:123604, 2019.

[126] K. Jacobs. *Input–output theory*, page 458–474. Cambridge University Press, 2014.

[127] C. K. Law. Effective hamiltonian for the radiation in a cavity with a moving mirror and a time-varying dielectric medium. *Phys. Rev. A*, 49:433–437, 1994.

Scientific publications

Author contributions

Co-authors are abbreviated as follows: Peter Samuelsson (PS), Patrick P. Potts (PPP), Subhomoy Haldar (SH), Ville F. Maisi (VFM), Antti Ranni (AR), Harald Havir (HH), Sebastian Lehmann (SL), Kimberly A. Dick (KAD).

Paper I: Full counting statistics of the photocurrent through a double quantum dot embedded in a driven microwave resonator

PS and PPP came up with the idea for the project. I did most of the analytical and all of the numerical calculations under the supervision of PS and PPP. I wrote the bulk of the manuscript. PS wrote the abstract and introduction. All authors contributed to the analysis of the results and the revision of the manuscript.

Paper II: Wigner-function formalism for the detection of single microwave pulses in a resonator-coupled double quantum dot

PS and PPP came up with the idea to investigate single microwave pulse drives. PPP came up with the idea to use the Wigner function for our analysis. I did most of the analytical and all of the numerical calculations in the low-drive regime. PPP derived the Heisenberg-Gabor limit. PS did most of the analytical calculations in the large-drive regime. All authors contributed to the writing of the manuscript and the analysis of the results.

Paper III: Microwave power harvesting using resonator-coupled double quantum dot photodiode

VFM and SH conceived the experiment. SH and HH designed and fabricated the nanowire-resonator device. SH performed the measurements. I, PS and PPP performed the theoretical calculations and the numerical simulations. I, SH, VFM, PPP and PS performed the data analysis. All authors contributed to the discussion of the results and the manuscript preparation. SL and KAD designed and fabricated the nanowires.

Paper IV: Symmetries and decoherence in a double quantum dot coupled to a high-impedance microwave resonator

VFM and AR conceived the experiment. AR designed and fabricated the nanowire-resonator device. AR performed the measurements. I performed the theoretical calculations and the fitting of the theory to the experimental data. I, VFM, PPP and PS performed the data analysis and contributed to the discussion of the results and the manuscript preparation. SL and KAD designed and fabricated the nanowires.